BUILDING EXTRACTION IN HAZARDOUS AREAS USING EXTENDED MORPHOLOGICAL OPERATORS WITH HIGH RESOLUTION OPTICAL IMAGERY(Dissertation_全文)

Chandana Dinesh Kumara Parapayalage

Chandana Dinesh Kumara Parapayalage. BUILDING EXTRACTION IN HAZARDOUS AREAS USING EXTENDED MORPHOLOGICAL OPERATORS WITH HIGH RESOLUTION OPTICAL IMAGERY. 京都大学, 2014, 博士(工学)

BUILDING EXTRACTION IN HAZARDOUS AREAS USING EXTENDED MORPHOLOGICAL OPERATORS WITH HIGH RESOLUTION OPTICAL IMAGERY

CHANDANA DINESH KUMARA PARAPAYALAGE

2014

KYOTO UNIVERSITY

京都大学

DISSERTATION THESIS

BUILDING EXTRACTION IN HAZARDOUS AREAS USING EXTENDED MORPHOLOGICAL OPERATORS WITH HIGH RESOLUTION OPTICAL IMAGERY

Author
Chandana Dinesh Parape

Supervisor
Prof. Masayuki Tamura

Laboratory of Geoinformatics
Department of Urban and Environmental Engineering
Graduate School of Engineering
Kyoto University
2014

BUILDING EXTRACTION IN HAZARDOUS AREAS USING EXTENDED MORPHOLOGICAL OPERATORS WITH HIGH RESOLUTION OPTICAL IMAGERY

By
Chandana Dinesh Parape

Doctoral Course of Human Security Engineering (HSE),
Environmental Management Leader (EML) &
Global Leader Program (GL)
Laboratory of Geoinformatics
Department of Urban and Environmental Engineering
Graduate School of Engineering
Kyoto University

A dissertation submitted in partial fulfillment of the requirements for the degree of Doctor of Philosophy

Examining Committee:	Prof. Masayuki Tamura (Chairperson) Assoc Prof. Muneta Yokomatsu Assoc Prof. Junichi Susaki
Nationality:	Sri Lankan
Previous Degrees:	**Master of Science** (Department of Urban and Environmental Engineering, Graduate School of Engineering, Kyoto University, Kyoto, Japan) **Bachelor of Science** (Department of Civil Engineering, Faculty of Engineering, Kobe University, Kobe, Japan) **Diploma in Civil Engineering and Architecture** (Department of Civil Engineering & Architecture, Tokuyama Collage of Technology, Yamaguchi, Japan)

Dedicated to my Parents

Dayasena Parape,

Soma Chandrasiri

&

memory of my Grandfather

Ayurvedic doctor Karanis Parape

"Education is not the learning of facts,
but the training of the mind to think."
– Albert Einstein

"Strength does not come from winning. Your struggles develop your strengths. When you go through hardships and decide not to surrender, that is strength."
–Arnold Schwarzenegger

ABSTRACT

In the past couple of decades, remote sensing techniques have been extensively exploited in hazard mapping, rescue, evacuation, emergency response, and disaster mitigation and rebuilding process. Rescue and evacuation of occupants from the hazardous regions are the main tasks of emergency response after a disaster and predicting building damages is also useful for emergency management. In other words, damaged building detection is a key element in the post disaster crisis assessment and response procedures. Generally, both airborne and space borne optical sensors can cover much larger areas than other platforms, and hence, they can be used for damage detection in large-scale natural disasters. However, the building extraction using optical imagery, especially in hazard areas, is still the subject of ongoing research. The challenges are due to: inaccurate feature extraction using optical images, variety and complexity of building roof, the effects of the ruble in hazardous areas, etc.

In this thesis, we proposed and develop novel Mathematical Morphology (MM) based methods and algorithms for accurate building extraction in hazardous areas. First, MM based novel method has been extended to pattern recognition combing morphological filters and Hit-Or-Miss Transform (HMT). In this method which is developed optimizing the shape and the size of HMT morphological filtering parameters with morphological operators are presented for building roof target detection.

In a second step, another novel approach for building roof reconstruction and classification method is introduced. Here the main two classification methods of SVM and Random Forest (RF) are tested for building roof extraction. Usually RF classification is based on week learners; however, our well performed RF classification algorithm gave higher accurate results on building extraction.

In a third step, Discrete Fast Fourier Transform (DFFT) method is tested for pre and post event image registration and developed a damaged building identification method using the power spectrum changes. Finally, combining both these methods produced significantly high accurate damaged maps were generated and optimized results were validated with ground truth survey and existing GIS data for accuracy assessment.

The study solely based only on freely available and downloadable data but with different scales, rotation and shifted imagery. These images were obtained at pre and post disaster situations and hence the cost efficiency of the method is very high. Single source optical images with spectral information represented by pixel values can adapt to different image analysis tasks to certain degrees of accuracy, hence multisource images can be useful in this context. Considering the ground condition of the candidate heavily damaged areas that used for the study, these accuracy values are reasonable. On the basis of the study, the analysis and the experiments carried out in the framework of this thesis, we identified some interesting directions of research as future development of this work.

Key words: *optical image processing, natural hazard, building extraction, pattern recognition, Mathematical Morphology, Differential Morphological Profile, Hit-Or-Miss Transform, Random Forest, Discrete Fast Fourier Transform, GIS.*

ACKNOWLEDGEMENTS

The task of undertaking a PhD education requires a lot of sacrifice and support from many people. I have been fortunate to have the support of professors, colleague, friends and family. I’m really pleasure to express my gratitude to all these people.

First and foremost, I would like to express my profound gratitude and appreciation to my supervisor, Professor Masayuki Tamura, for his invaluable advices, encouragement and his continuous generous support throughout my PhD study. Without his guidance and support that based on his deep insight experience in the field of Remote Sensing and Environmental Engineering, this work could not have been completed. I owe him not only for this study, But also for extending his help on various aspects of my life in Kyoto University.

I am also deeply indebted to Associate professor Junichi Susaki for his valuable suggestions and advices during my study. I gratefully thank Mr. Akamatsu, secretary of Geo-informatics Laboratory, who has been so kind in assisting during my study in both Master and Doctoral research. I would like to extend my gratitude to Prof. Ranjith Dissanayeke and Mr. Abdul Bari in University of Peradeniya, Sri Lanka for contribute their valuable time for joint research and field survey. I would like to express my profound appreciation to Jón Atli Benediktsson and Prashanth Reddy Marpu, University of University of Iceland, for their valuable suggestions, advices and knowledge sharing in this study.

My appreciation is also extended to the member of the dissertation committee, Associate Professor Muneta Yokomatsu for advices and suggestions of him as well as for the valuable time and efforts in reviewing this thesis.

I appreciate the students of Geo-informatics laboratory for their kind support and assistance. I am grateful to my colleagues for providing me a pleasant and creative environment during my research. In particular, I would like to thank all of Doctoral students Mr. Duminda Welikanna and Mr. Jin and all other laboratory members, their support and encouragement are greatly appreciated.

I sincerely express acknowledge to all of my host families Akira, Ikoku, Nakaji, Nagaoka and Ueda, who made Japan my second home. I would also like to express my thanks to the financial and research work advices provided by Fuji Zerox and Yamaoka Scholarship grant, which made this doctoral study possible. My most deeply-felt

gratitude goes to my parents, brothers and sister in Sri Lanka for all their love, support and faith in my entire life and particular during my study in Japan.

I dedicate this dissertation to them. Finally, I would like to thank all interesting people from all over the world who has contributed directly or indirectly to the realization of this study, and who have made my time in Japan enjoyable and fruitful.

Kyoto, 2014
Chandana Dinesh

BIBLIOGRAPHY

Author’s Publications

International Journals

1. Chandana Dinesh Parape, Masayuki Tamura, U. Abdul Bari, P.G. Ranjith Dissanayake, “Detecting and assessment of tsunami building damage using high-resolution satellite images with GIS data, International Journal of Disaster Resilience in the Built Environment”, Emerald, ISSN 1759-5908, Vol.4(2), pp. 132-144, 2013. (Published)

2. Chandana Dinesh Parape, Chinthaka Premachandra, Masayuki Tamura, Masami Sugiura, “Morphological Hit-Or-Miss Transform Based Approach for Building Damage Estimation from VHR Airborne Imagery in 2011 Pacific Coast of Tohoku Earthquake and Tsunami”, International Archives of Photogrammetry, Remote Sensing and Spatial Information Sciences, Vol. 30-B3, pp. 509-512, 2012. (Published)

3. Chandana Dinesh Parape, Chinthaka Halpage, Masayuki Tamura, Ubdul Bari, Ranjith Disanayake, Duminda Welikanna, Shengye Jin, Masami Sugiura, “Building Damage and Business Continuity Management in an Event of Natural Hazard – Case study in year 2004 Tsunami, SRI LANKA”, International Journal of Sustainability, ISSN 2071-1050, Issue 5(2), pp. 456-477, 2013. doi:10.3390/su5020456.(Published)

4. Chinthaka Halpage, Chandana Dinesh Parape, “Road Crack Detection Using Color Variance Distribution and Discriminant Analysis for Approaching Smooth Vehicle Movement on Non-smooth Roads International Journal of Machine Learning and Cybernetics”, International Journal of Machine Learning and Cybernetics (Springer), doi: 10.1007/s13042-014-0240-6. (Published).

5. Chandana Dinesh Parape, Masayuki Tamura, “Optimization of structure elements for morphological Hit-Or-Miss transform for building extraction from VHR airborne imagery in natural hazard areas”, International Journal of Machine Learning and Cybernetics (Springer), (Accepted).

6. Chinthaka Halpage, Chandana Dinesh Parape,”Parallel Layer Scanning Based Fast Dot/Dash Line Detection Algorithm for Large Scale Binary Document Images”, ICIAR 2014, Part I, LNCS 8814, pp. 395–402, 2014.DOI: 10.1007/978-3-319-11758-4_43. (Published)

Conferences Proceedings (International)

1. Chandana Dinesh Parape, Masayuki Tamura, Chinthaka Premachandra, Duminda Welikanna, and Shengye Jin, "Urban building damage detection using Fast Fourier Transform from pre and post event high resolution airborne stereo imagery in case of natural hazards", 2013 CaGIS/ASPRS Specialty Conference, San Antonio, Texas, USA, October 2013 (Paper Peer reviewed /Poster)

2. Chandana Dinesh Parape, Masayuki Tamura, Chinthaka Premachandra, Duminda Welikanna, and Shengye Jin, "Morphological operators based approach for building extraction in hazardous areas using close range airborne imagery", 2013 CaGIS/ASPRS Specialty Conference, San Antonio, Texas, USA, October 2013.(Paper Peer reviewed /Poster)

3. Chandana Dinesh Parape, Chinthaka Premachandra, Masayuki Tamura, Masami Sugiura, Automated Identification of Tsunami Induct Damaged Buildings From Airborne Imagery Using Extended Morphological Transformations, International Conference on Disaster Management 2012 (IIIRR), Kagoshima, Japan, August 2012.(Paper Peer reviewed/Oral)

4. H. Waruna H. Premachandra, Chinthaka Premachandra, Chandana Dinesh Parape and Hiroharu Kawanaka, "Parallel Scanning Based Fast Elliptical Object Detection Approach for High-resolution Binary Document Images", International Workshop on Advanced Image Technology, January 2014.(Oral)

5. H. Waruna H. Premachandra, Chinthaka Premachandra, Chandana Dinesh Parape, "Parallel Scanning Based Speed-up Method for Detection of Elliptical Obstacles in High-resolution Image", International Journal of Computer Science and Communication Networks, November 2013.(Poster)

6. Chinthaka Premachandra, H. Waruna H. Premachandra, and Chandana Dinesh Parape, "Image Based Automatic Road Surface Crack Detection for Achieving Smooth Driving on Deformed Roads", Proc. IEEE International Conference on Systems, Man, and Cybernetics, October 2013.(Oral)

7. H. Chinthaka N. Premachandra, Chandana Dinesh Parape, and H. Waruna H. Premachandra, “A Study on Image Processing Based Road Crack Detection”, Proc. of 2013 RISP International Workshop on Nonlinear Circuits, Communications and Signal Processing, Hawaii, USA, March 2013.(Peer reviewed/ Oral)

8. Chandana Dinesh Parape, Masayuki Tamura, “Automatic Damaged Building Detection Using Fast Fourier Transform from Close Range Optical Imagery in Case of Natural Hazards”, ISPRS Congress 2012, Melbourne, Australia, August 2012.(Peer reviewed/ Oral)

9. Chandana Dinesh Parape, Chinthaka Premachandra, Masayuki Tamura, Masami Sugiura, “Morphological Hit-Or-Miss Transform Based Approach for Building Damage Estimation from VHR Airborne Imagery in 2011 Pacific Coast of Tohoku Earthquake and Tsunami”, Chandana Dinesh Parape, Chinthaka Premachandra, Masayuki Tamura, Masami Sugiura, ISPRS Congress 2012, Melbourne, August 2012.(Peer reviewed/Oral)

10. Chandana Dinesh Parape, Chinthaka Premachandra, Masayuki Tamura, Masami Sugiura, “Damaged Building Identifying from VHR Satellite Imagery using Morphological Operates in 2011 Pacific Coast of Tohoku Earthquake and Tsunami”, IGARSS-2012, Munich, Germany, July 2012.(Oral)

11. Chandana Dinesh Parape, Masayuki Tamura, “Mathematical Morphology Based Approach for Building Damage Estimation from VHR airborne Imagery of Ishinomaki Area in 2011 Pacific Coast of Tohoku Earthquake and Tsunami”, FIG working week 2012, International Federation of Surveyors, Rome, Italy, May 2012.(Peer reviewed/Oral)

12. Chandana Dinesh Parape, Masayuki Tamura, “Identifying Damaged Building from High-Resolution Satellite Imagery in Hazardous Area using Morphological Operators”, IGARSS-2011, Vancouver, Canada, July 2011.(Poster)

13. U.Abdul Bari, Chandana Dinesh Parape, Mazayuki Tamura, P.G. Ranjith Dissanayake, “Tsunami Damaged Buildings Assessment Using Satellite Imagery, GIS & GPS Data, International Conference on Building Resilience”, Interdisciplinary approaches to disaster risk reduction and the development of sustainable communities", Kandalama, Sri Lanka, July 2011.(Peer reviewed/Oral)

14. Chandana Dinesh Kumara, Masayuki Tamura, “Identification of Damaged Building from

High-Resolution Satellite Imagery in Hazardous Areas using Extended Morphological Operators- Case Study in China", ISPRS Hannover Workshop: High Resolution Earth Imaging for Geospatial Information, Hannover, Germany, June 2011.(Peer reviewed/Poster)

15. Chandana Dinesh Kumara, Masayuki Tamura, "Identify Damaged Building from High-Resolution Satellite Imagery in Hazardous Areas using Morphological Operators", 34th International Symposium on Remote Sensing of Environment, Sydney Convention and Exhibition Centre, Sydney, Australia, April 2011.(Peer reviewed/Oral)

16. Chandana Dinesh Kumara, Masayuki Tamura, "Identify Damaged Buildings from High-Resolution Satellite Imagery in Hazard Area Using Differential Morphology", ICIAfS 10 - 5th International Conference on Information and Automation for Sustainability, Colombo, Sri Lanka, December 2010.(Peer reviewed/Oral)

17. Chandana Dinesh Parape, Masayuki Tamura, "Identify Damaged Buildings from High-Resolution Satellite Imagery in Hazard Area Using Differential Morphology", ICSBE –International Conference on Sustainable Built Environment, Kandy, Sri Lanka, December 2010.(Peer reviewed/Oral)

18. Chandana Dinesh, Environment issues in Sri Lanka; Colombo waste management Project, Environmental & Sanitary Engineering Research, 23(4), pp.21-22, 2009.

19. Chandana Dinesh Parape, Masayuki Tamura, "Extract mangrove forests in Sri Lanka using Landsat data and SRTM elevation data, 29th Asian Conference of Remote Sensing", Colombo Sri Lanka, September 2008.(Poster)

Conferences Proceeding (Domestic)

1. Chandana Dinesh Kumara, Masayuki Tamura, "Extraction and Assessment of Buildings Damages from High-Resolution Satellite Imagery", 第20回生研フォーラム「広域の環境・災害リスク情報の収集と利用フォーラム」 International Center for Urban Safety Engineering (ICUS), March 2011.(Oral)
2. Chinthaka Premachandra, H. Waruna H. Premachandra, Chandana Dinesh Parape, "Road Crack Detection for Making Complex Road Surface Drivable Functions", 第12回情報科学技術フォーラム, November 2013.(Poster)

3. Chandana Dinesh Parape, Masayuki Tamura, "Mapping mangrove forests in Sri Lanka using Landsat images and SRTM elevation data", Japan Association of Surveyors Geo Information Forum, Pacifico Yokohama, Japan, June 2009.(Poster)

4. Chandana Dinesh Parape, Masayuki Tamura, "Extract mangrove forests and change detection within a decade in Sri Lanka using Landsat data and SRTM elevation data", Chandana Dinesh Parape, Masayuki Tamura, 45th Conference of Japan Society of Remote Sensing, Nopporo, Sapporo, Japan, December 2008.(Poster)

5. Y. Kuwata, Chandana Dinesh Parape and S. Takada, "Business Continuity Management after Tsunami for local Industries in Sri Lanka", 61th Civil Engineering Conference of Japan, Ritsumeikan University, Kyoto, Japan September 2006.(Oral)

Grant and Award

1. Certificate of International Environmental Leadership (EML)
2. Certificate of Global Leaders in Advanced Engineering & Pharmaceutical Sciences (GL)
3. Certificate of Human Security Engineering (HSE)
4. Yamaoka scholarship Grant (2009/2010)
5. Setsutaro Kobayashi Memorial Grant for young researcher (2010)
6. Setsutaro Kobayashi Memorial Grant for young researcher (2011)

Activities

1. Member of American Society of Photogrammetry and Remote Sensing (ASPRS)
2. Member of International Society of Photogrammetry and Remote Sensing (ISPRS)
3. Member of Institute of Electrical and Electronics Engineers (IEEE)
4. Member of Japan Society of Photogrammetry and Remote Sensing (JSPRS)

Thesis / Dissertations

Chandana Dinesh Parape. Mangrove Extraction and Change Detection in Sri Lanka Using Landsat TM/ ETM+ and SRTM Satellite Data (2009), Kyoto University, Kyoto, Japan.(Msc)

Chandana Dinesh Parape. Business continuity management after the Tsunami Hazards in Sri Lanka (2007), Kobe University, Kobe, Japan (Bsc)

Chandana Dinesh Parape. Land Cover Classification and Change Detection of Yamaguchi Prefecture using Landsat Multispectral Data (2004), Tokuyama Collage of Technology, Yamaguchi, Japan. (Diploma)

CONTENTS

List of Figures

List of Tables

List of Abbreviations

AA	Average Accuracy
Abs	Absolute value
ASME	American Society of Mechanical Engineers
API	Application Programming Interface
AVIRIS	Airborne Visible/Infrared Imaging Spectrometer
BRR	Building Roof Reconstruction
CA	Class-specific Accuracy
CART	Classification and Regression Tree
CC	Connected Components
Conj	Complex conjugate
CPU	Central Processing Unit
CR	Closing by Reconstruction
CRAN	Comprehensive R Archive Network
CUDA	Compute Unified Device Architecture
DAFE	Discriminant Analysis Feature Extraction
DBFE	Decision Boundary Feature Extraction
DFT	Discrete Fast Fourier Transform
DMP	Differential Morphological Profile
EMP	Extended Morphological Profile
FFT	Fast Fourier Transform
FORTRAN	FORmula TRANslation computer language
GIS	Geographic Information Systems
GLCM	Gray Level Co-occurrence Matrix
GPU	Graphics Processing Unit
GPS	Geometric Product Specification
HTM	Hit-Or-Miss Transform
HSEG	Hierarchical SEGmentation
HSWO	Hierarchical StepWise Optimization
ICA	Independent Component Analysis
IFFT	Inverse Fast Fourier Transform
ISODATA	Iterative Self-Organizing DATa Analysis
LDA	Linear Discriminant Analysis

MC	Multiple Classifier
ML	Maximum Likelihood
MP	Morphological Profile
MRF	Markov Random Field
MSSC	Multiple Spectral-Spatial Classifier
NN	Nearest Neighbor
NN	Neural Network
NWFE	Non-parametric Weighted Feature Extraction
OA	Overall Accuracy
OC	Opening by Closing
OOB	Out-Of-Bag
OR	Opening by Reconstruction
PC	Principal Component
PCA	Principal Component Analysis
PDF	Probability Density Function
QGIS	Quantum GIS
RF	Random Forest
ROI	Region OF Interest
SAR	Synthetic Aperture Radar
SAM	Spectral Angle Mapper
SDK	Software Development Kit
SE	Structuring Element
SID	Spectral Information Divergence
SVM	Support Vector Machines
VHR	Very High Resolution
ZMPS	Zero Maximum scaled Power Spectrum
2D	Two dimensions

Numerical Notations

Chapter 3

Section 3.1

f	Image
p	pixel
ψ	function
$N(p)$	neighborhood
$(\wedge)$	*infimum*
$(\vee)$	*supremum*
λ	Structuring Element
$\overline{\lambda}$	Reflected structuring element
n	Aarray
ε_λ	Erosion
δ_λ	Dilation
γ_λ	Opening
φ_λ	Closing
γ_λ^*	Opening with reconstruction
φ_λ^*	Closing with reconstruction
r	Radius size of disc (circular) shape Structuring Elements
$\prod_{\gamma_\lambda}(f)$	*opening profile*
$\prod_{\varphi_\lambda}$	*closing profile*
Δ_{γ_λ}	*derivative of the opening profile*
Δ_{φ_λ}	*derivative of the closing profile*

Section 3.2

η_{FG}	Foreground of SET

η_{BG}	Background of SET
$C_{\eta_{FG}}$	Center of the complement of foreground
$C_{\eta_{BG}}$	Center of the complement of the background
t_i	Threshold value

Section 3.3.2

t	Tree
T	Forest size
D	Tree depth
ρ	Injected randomness
i	Attribute
x_i	Attributes of data point (instance lable)
F	Feature space
d	dimensionality of the feature space
d'	Dimensionality of the subspace
v	Vector (data point)
θ	split function (weak learner model)
ϕ	Filter function (subset selected from the set of all possible features)
ψ	Geometric primitive (axis-aligned hyperplane)
$\Im$	Parameters of the test function
τ	Treshold
$[\cdot]$	Indicator function (Tree Training)
$[\times]$	Indicator function (Tree Testing)
j	jth node
$h(\mathrm{v},\theta_j)$	test function
S_j	training set
I_j	information gain in j th node (objective function)

θ_j^* Maximization of an objective function

$H(S)_{Shannon}$ Shannon entropy

$H(S)_{Gini}$ Gini index

S training points
c class label
C set of all classes
$p(c)$ empirical distribution
I information gain
$P(c\,|\,\mathrm{v})$ posterior distributions

$\Im_j$ Small random subset thresholds

ϕ Filter function

l_j True label of x_i

$[\cdot]$ Indicator function (training)
$[\times]$Indicator function (testing)
$\wp$ Indicator function (feature importance)
$\aleph$ feature importance
$\mathcal{B}^{(t)}$ In-Bag samples for a tree
$\mathcal{B}^{c(t)}$ Out-Of-Bag samples (OOB; Complementary samples)

Section 3.4
f(x) two-dimensional function

x_1: Number of pixels horizontally

x_2 : Number of pixels vertically

k_1, k_2 : Spatial frequency variables

j : Imaginary component of complex number
$F(\xi, \eta)$ absolute value
(x, y) the point

R	ratio of two images
P_t	Total profile depth
R_a	arithmetic average of the absolute values
R_q	root mean squared (among the profile roughness)
R_z	mean roughness depth
R_{ti}	maximum height of the profile R_t for the i^{th} sampling length
W_t	Waviness height(total height of W-profile)
y_i	vertical distance from the mean line

Chapter 1

INTRODUCTION

1 Introduction

1.1 Research Background

1.2 Problem Statement
  1.2.1 Drawbacks of the optical remote sensing
  1.2.2 Drawbacks of the existing DMP

1.3 Objectives and Novel Contribution of the Thesis

1.4 Proposed Dissertation Framework

1.5 Thesis layout (Scope and Organization)

1 Introduction

1.1 Research Background

Any form of a natural hazard is a threat of a naturally occurring event that will have a navigate effect on the livelihood of the people. As reported in several reliable recent sources, various kinds of natural hazards occurring all over the world, they kill and affect thousands of people and damage billions of properties. By region, Asia is the highest in all indices for disaster occurrences. Asia accounts for 35.8 percent of disaster occurrence; number of people killed, 52.1 percent; total number of affected people, 78.3 percent; and the amount of economic damage, 44.9 percent [1]. Figure.1.1 and 1.2 show the increasing natural disaster trend and estimated damage (in US$ billion) caused by reported natural disasters between year 1900 and 2010.

In the past couple of decades, remote sensing techniques have been extensively exploited in hazard mapping, rescue, evacuation, emergency response, and disaster mitigation and rebuilding process. Remote sensing is the leading technique to quickly map the damage at different scales, coordinating the relief effort and to assess the vulnerability of the areas. Rescue and evacuation of occupants from the hazardous regions are the main tasks of emergency response after a disaster and predicting building damage is also useful for emergency management. In other words, damaged building detection is a key element in the post disaster crisis assessment and response procedures. Generally, both airborne and space borne optical sensors can cover much larger areas than other platforms, and hence, they can be used for macro-scale urban modeling and damage detection in large-scale natural disasters.

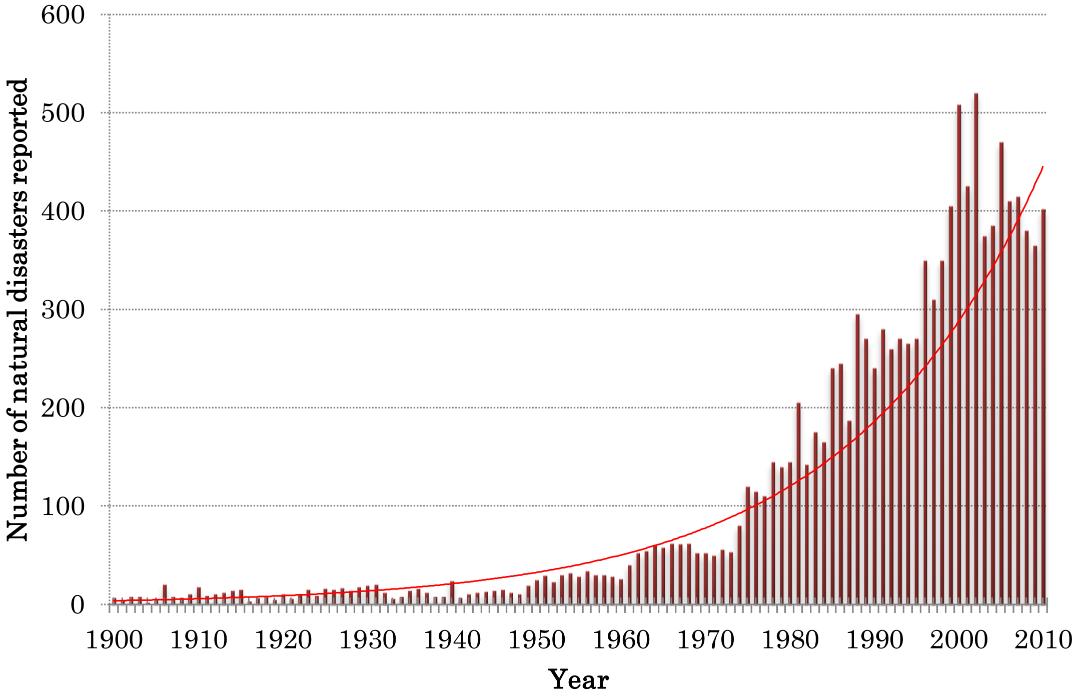

Fig.1.1. Natural disasters trend reported in year1900-2010.

(Source: Report-2010, ADRC, Kobe, Japan)

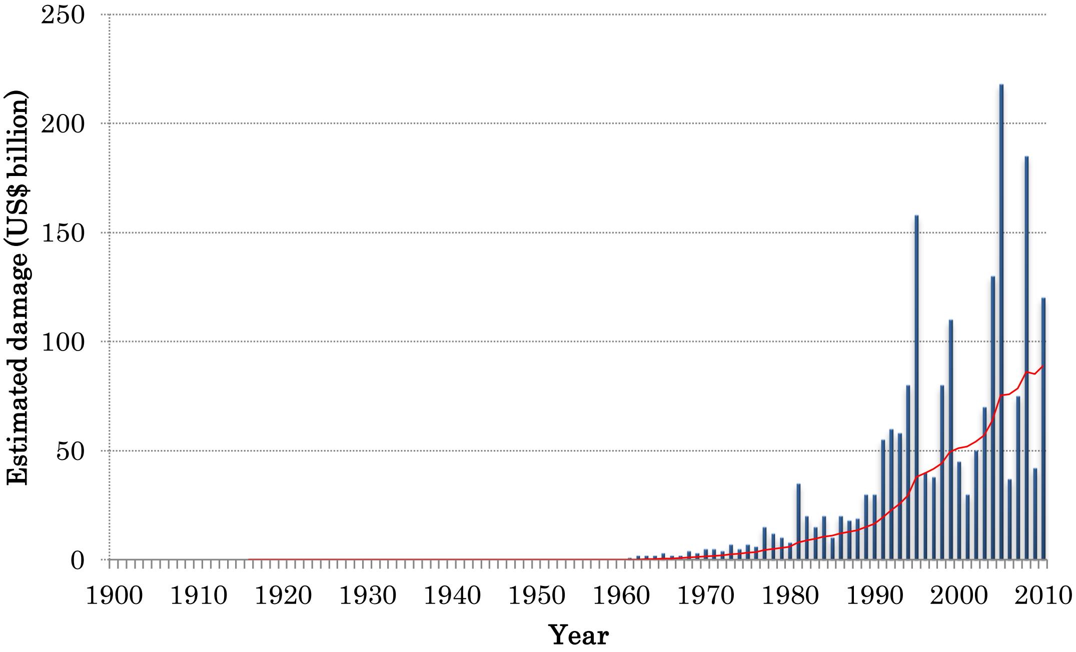

Fig.1.2. Estimated damage caused by reported natural disasters.

(Source: Report-2010, ADRC, Kobe, Japan).

1.2 Problem Statement

Remote sensing techniques provide a strong base for large area disaster mapping, damage monitoring and coordinating relief efforts [2]. The prompt and accurate detection and assessment of urban building damage caused by natural hazard is one of the important aspects of above damage monitoring. There have been a lot of published work and real implementations of using remote sensing technique for hazard mapping. The development of advanced remote sensing technologies has improved the mapping capabilities and expanded the areas of applications.

The methods that have been designed for building damage detection can be basically divided into two groups: (1) methods that interpret only post event data and (2) methods that detect damaged building between pre and post event data. Compared to methods using only post-event data, more accurate results can be obtained by those using pre and post event data [3]. The obvious shortcoming of the methods using only post disaster data is less satisfactory. Because detection outcome face the difficulty of precisely identifying the damage without knowing what existed before the hazard. Also, it has a major limitation in many urban areas, especially in developing countries where pre event reference ground truth data is hard to find (e.g. GIS).

Change detection using pre and post event SAR, LiDAR and optical data are popular methods to acquire building damage information. Using SAR images, building damage can be detected based on changes in the backscatter coefficient and intensity correlation (amplitude), phase information or the combination of phase and amplitude information. However, restricted by the source and quality of the SAR data, the quantitative relationship between the coherence coefficients and the damage grades must still be worked out. Most of the research also revealed that the results from damaged building detection using SAR images were less conclusive without the aid of additional image data or ground truth information [4, 5, 6, 7].

Airborne LiDAR systems allow fast and extensive acquisition of precise height data which can be used for detecting some specific damage types (e.g., pancake collapse) that cannot be identified by 2D images. Since LiDAR is a relatively new technology and many places do not have LiDAR coverage, a little research has been done using real pre and post event LiDAR data for building damage detection. Usually it is not a common practice to obtain laser scanning data right after a natural hazard only for the purpose of building damage detection, due to the cost and difficulty in flight planning [8, 9, 10].

Optical imagery with spatial resolution finer than 1m can be acquired by both airborne and space borne imagery. The emergence of VHR remote sensing imagery with detailed texture and context information makes it possible to detect damaged building. Various properties in spectra, texture, edge, spatial relationship, structure, shape and shadow in the imagery has been used for damage extraction. The increased availability of this type of data and the frequently updating images archive make VHR optical data well-suited as a pre event reference data source for building damage detection [11, 12, 13, 14, 15, 16].

The most significant improvement was the commercialization of high spatial resolution optical satellite images such as IKONOS, Geo-Eye and Quick Bird [17, 18]. These high resolution optical images from space borne and airborne sensors provide data with a ground samplings distance in the panchromatic band of up to 0.5m or 0.2m, respectively, a sufficient spatial resolution for the desired task of building extraction.

1.2.1 Drawbacks of the optical remote sensing

Automated extraction of building from airborne or space borne imagery has been an active research field for decades. However, extracting building from high resolution remote sensing imagery is a quite challenging task, until now building detection using optical remote sensing images still remains as an open problem. In addition, most current approaches do not work in densely built-up areas and hazardous areas. There are a number of challenges and the difficulties are outlined below.

1. Manual extraction of buildings from the imagery is very time-consuming. A major drawback of manual interpretation is low efficiency, difficulties in meeting urgent demands in the emergency response and outputs are subjected to heavy operator supervision.

2. Building can be rather complex structures with different shapes and scales, and they might be surrounded by a dense urban region. (Building geometry and neighborhood complexity)

3. The variety of roof (e.g. shape, color, etc.), shadows and smoke (e.g. in the hazard region) frequently occur, which makes the appearance of buildings in image incomplete and irregular.

4. Different environmental noises such as roads, individual trees and vehicles which are not easy to distinguish from buildings.

5. Obtaining significant distinctions between man-made objects and natural background to achieve effective image segmentation, resulting in high false detection.

6. Rubble, debris and small scale watershed after the natural disaster caused noises heavily.

To deal with the above difficulties, researchers have proposed many approaches [19][20][21], which usually use pixel based or object based methods. However, these methods are not suitable for building detection in intensely build-up high resolution satellite images. Extracting building from high resolution remote sensing imagery is a challenging task, as the building can be rather complex, such as structures with different shapes and scales, they might be surrounded by a densely urban region. In a high resolution satellite image with hundreds of complex buildings, the number of lines or junctions is large, and also the noise levels which are very hard to distinguish from the real information are needed. They may appear very differently in intensity level, shapes and other patterns. There are nearly no general features to describe as buildings.

Among the various analyses and approaches, *Mathematical Morphology* (MM) based methods draws promising and strong attention recently. Topological and geometrical continuous-space concepts such as size, shape, convexity, connectivity, and geodesic distance, were introduced by MM on both continuous and discrete spaces. MM is also the foundation of morphological image processing, which consists of a set of operators that transform images according to the above characterizations. They either completely remove or entirely preserve a structure in the image and do not distort the shape of structures nor introduce new edges [22]. Image segmentation considering not only the pixel based but also the object based is another advantage of the MM. *Differential Morphological Profile* (DMP), further extension of MM is a multi-scale image processing algorithm that employs a combination of Morphological Operators (MO) and derivatives of the resulting Morphological Profile (MP) [23, 24]. This technique attempts to classify regions of an image as homogeneous with respect to a series of Structuring Elements (SE) with increasing radius.

Here the basic MO is the erosion, dilation, opening and closing. Morphological residuals between the original gray-level function and the composition of a granulometry and an anti-granulometry by reconstruction are used to build a so called MP function. The DMP is defined as a vector where the measure of the slope of the opening-closing profile is stored for every step of an increasing SE series. (The MM will be further discussed in section.3.1).

1.2.2 Drawbacks of the existing DMP

Although DMP contain strong information on land cover and their spectral properties, several shortcomings of the existing MP based approach are listed below,

1. The existing MP based methods do not explore all aspects of the feature space, including the buildings in urban areas and more advanced approaches should be investigated [25]. The building extraction performance has among the best results reported in the literature thus far as percentage of 58%. [17].

2. Existing DMP based methods are not sufficient enough for accurate classification and none of them are focused on damage or hazard areas.

3. This method concerns the necessity of looking at a large range of increasing opening closing by reconstruction. Therefore, the resulting differential profile can be high-dimensional and contain unnecessary data profile for building extraction. Which means it is required to identify the necessary bands of DMP, the Structuring Elements (SE) size and shape performs well for the building in the image. Usually the determination of the size and shape of the SE is largely an empirical process [26].

4. The multiscale approach based on a range of different SE sizes are allowed to explore a range of different hypothetical spatial domains. However, a proper classification process is needed to use for the best response of the structures in the image.

5. Computational complexity, processing limited to the analysis of the scale, limitation in the characterization of features to be modeled due to the usage of structuring elements.

These problems should be solved for successful use of DMP for building identification and damage assessment.

1.3 Objectives and Novel Contribution of the Thesis

For the general case of object extraction, it is impossible to assume that all buildings will always be of a uniform size in the candidate area. Thus, SEs of multiple scales are a necessity. Additionally, the multi - scale techniques also allow for the identification of object substructures. Among the various analyses, approaches and use of our 5 years experience, MP based methods draw promising and attention more so than the other methods. The MP based methodology is sufficient enough for land cover classifications, but none of the literature is focused on hazardous areas for high accurate building extraction.

The objective of this study is to develop a further extension of the MP based method for building extraction using space borne or airborne imagery in natural hazardus areas with improved accuracy. To overcome the difficulties of the MP based algorithm we investigate further extensions of morphological operation, filtering irrelevant features, and performing of the processing with a reduced computation load and classification methods. Considering the building in the image rather than general land cover classification, the *Structuring Element* (SE) is prompt to optimized and identify the effective DMP channels (hypothetical spatial domains) for building. In particular, this study is devoted to the definition and in depth evaluation of the functionality of the SE and find the well performed classification method of *Random Forest* (RF) for building extraction in hazardous areas.

The study also tested an automated image registration method based on *Fast Furrier Transform* (FFT) for hazardous areas and proposed a novel rapid automated building damage extraction method based on Decrete Fast Fourier Transform (DFFT) using the max-scaled log power spectrum to increase the accuracy of the process beside the main MP based technique. Finally, these MP and FFT based methods are combined for higher accurate building and damage extraction.

Depending on the objectives the thesis outlines several novelties as follows.

1. To apply and investigate the performance of the MP and its extended connection operators in building extraction using VHR remotely sensed data.

    i. Extending the MP technique for building pattern recognition and determining the proper structural element size and shape for optimal performance. (Described in section 3.2)

ii. Investigating compatible classification approach to be integrated with the MM operation results. (Described in section 3.3)

2. Define the behavior of the FFT power spectrum of the VHR images in hazarded regions.

i. Automated registration of pre and post event image in hazardous areas using FFT based method

ii. Identifying damaged building using spectral analysis of the frequency domain. (Described in section 3.4)

The study region is selected from the hazardous area of Ishinomaki, Miyagi prefecture due to the 2011 Tohoku earthquake and tsunami. Mainly the freely available airborne or space borne high resolution optical images will be used as the remote sensing data. (In the present study, we were able to achieved more than 92% of building extraction accuracy, even in hazardous areas).

1.4 Proposed Dissertation Framework

The Proposed thesis framework is shown in Figure.1.3 and it consists of several steps as explained below.

Step.1.1- Pre and post event image registration manually or automated method that based on FFT.

Step.1.2- The pre and post event remote sensing images applied to extended morphological operators

Step.1.3- Damaged and undamaged building are extracted using pattern recognition and specified classification methods. The following approaches show the extended morphological based building extraction and optimization methods for optical images.

(a) Approach 1

Pattern Recognition-

Extended MP based approach combined with Hit-Or-Miss transform as a novel pattern recognition technique for building extraction from VHR space borne imagery in 2011 Pacific Coast of Tohoku Earthquake and Tsunami.

Purpose of above approach-

MP based approach extended to pattern recognition method using Hit-Or-Miss transform. The effect of template sizes and shapes of the candidate building in the images is analyzed, for their performances.

(b) Approach 2

Classification based Method-

Extend the MP for building roof rebuild and for building extraction in hazardous area using airborne imagery.

Purpose of above approach-

Although MP shows high complexity for feature extraction, further investigations are needed for better response of the

building structures in the image (including hazardous areas), avoiding noise for high accuracy building identification.

Step.2- Automated building damage identification using FFT from the spectral information of optical images.

Step.3- Data fusion of the MP based and FFT based techniques.

Step.4- Results validation with ground truth and existing GIS data.

1.5 Thesis Layout (Scope and Organization)

The outline of the work presented in this doctoral thesis is briefly described as follows.

Chapter 2: This chapter reviews some of existing literatures of building identification in hazardous areas.

Chapter 3: Introduce the basic concept of MO, MP and DMP. Then the important novelty of proposed optimizations of the pattern recognition templates and building roof reconstruction methods is described. The most effective classification method of *Random Forest* (RF) that performed for building extraction combing with extended MP are recalled. (The behaviors of the *Preformed Random Fores*t (PRF) for building extraction are described in chapter. 4) As a dual approach for damage extraction, Fast Fourier Transform based novel method has introduced.

Chapter 4: Present the results and the discussion.

Chapter 5: Finally the summary and an overall discussion of the dissertation as a whole are presented.

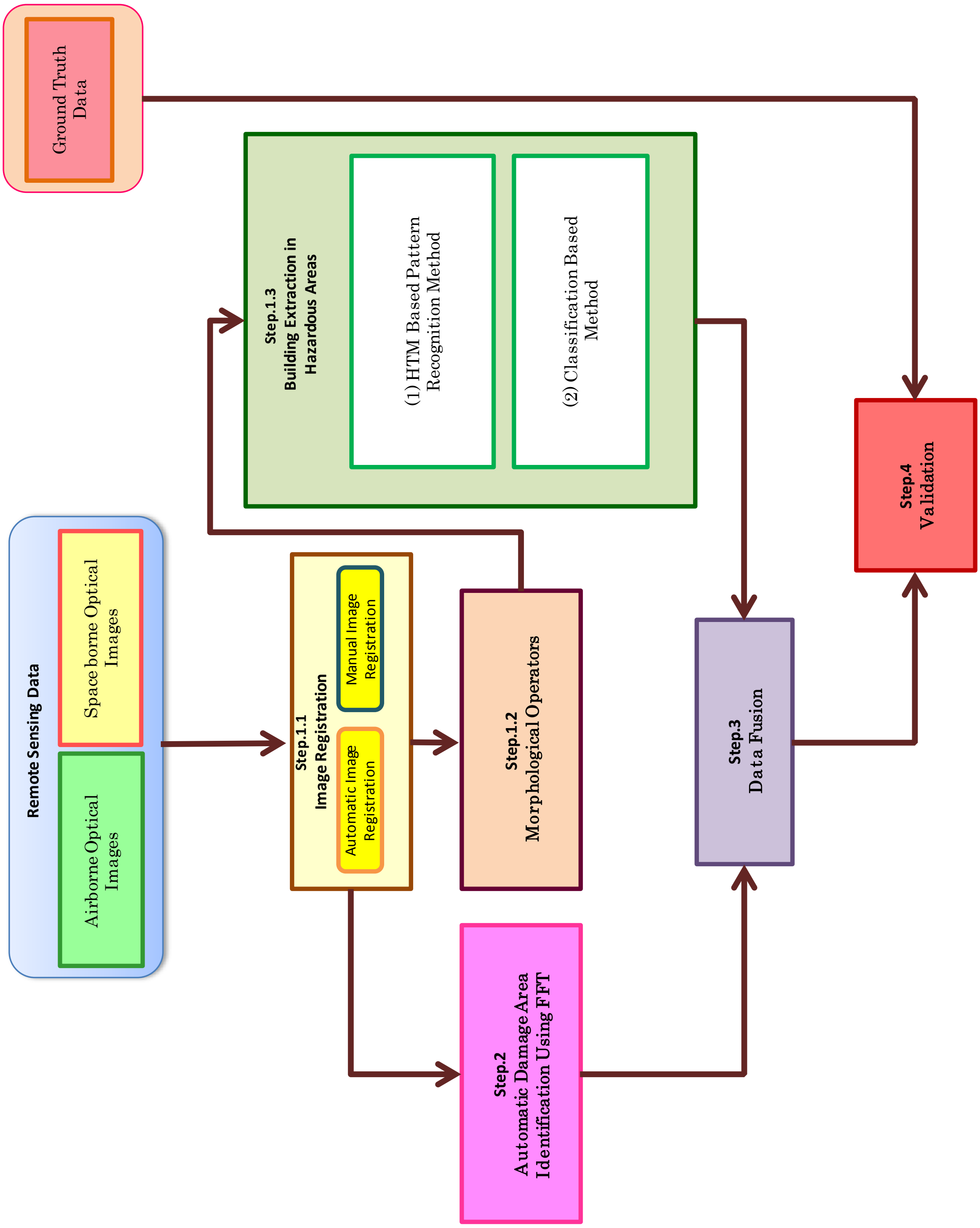

Fig.1.3. Proposed dissertation framework

References

[1] Natural Disaster Data Book, 2011, Asia Disaster Reduction Center, Kobe, Japan.

[2] Kerle, N., 2010, “Satellite-based damage mapping following the 2006 Indonesia earthquake”, International Journal of Applied Earth Observation and Geoinformation, Vol.12, pp. 466-476.

[3]Dong, L., Shan, J., 2013, A comprehensive review of Earthquake-induced building damage detection with remote sensing techniques, ISPRS Journal of Photogrammetry and Remote Sensing, Vol.84. pp. 85-99.

[4]Matsuoka, M., Yamazaki, F., 2004,”Use of satellite SAR intensity imagery for detecting building areas damaged due to earthquakes”, Earthquake Spectra, Vol.20(3), pp.975–994.

[5] Matsuoka, M., Yamazaki, F., 2005, “Building damage mapping of the 2003 Bam, Iran Earthquake using Envisat/ASAR intensity imagery”, Earthquake Spectra, Vol.21 (S1),pp.285–294.

[6] Ito, Y., Hosokawa, M., Lee, H., Liu, J.G., 2000,”Extraction of damaged regions using SAR data and neural networks”, Proceeding of 19th International Society for Photogrammetry and Remote Sensing (ISPRS) Conference, pp. 156–163.

[7] Yonezawa, C., Tomiyama, N., Takeuchi, S., 2002,”Urban damage detection using decorrelation of SAR interferometric data”, IEEE International Geoscience and Remote Sensing Symposium and 24th Canadian Symposium on Remote Sensing, Vol.I–Vi, pp. 2051–2053.

[8] Rehor, M., Voegtle, T., 2008,”Improvement of building damage detection and classification based on laser scanning data by integrating spectral information”, The International Archives of the Photogrammetry, Remote Sensing and Spatial Information Sciences, Beijing.

[9] Schweier, C., Markus, M., Steinle, E., 2004,” Simulation of earthquake-caused building damages for the development of fast reconnaissance techniques”, Natural Hazards and Earth System Sciences, Vol.4(2), pp. 285–293.

[10] Schweier, C., Markus, M., 2006, “ Classification of collapsed buildings for fast damage and loss assessment”, Bulletin of Earthquake Engineering, Vol.4, pp.177–192.

[11] Haralick, R.M., Shanmugan, K., Dinstein, I., 1973,”Texture features for image classification”, IEEE Transactions on Systems, Man, and Cybernetics, Vol.3, pp.610–621.

[12] Rathje, E.M., Woo, K.S., Crawford, M., Neuenschwander, A., 2005,”Earthquake damage identification using multi-temporal high-resolution optical satellite imagery”, IEEE International Geoscience and Remote Sensing Symposium, Vol.7, pp. 5045–5048.

[13] Saito, K., Spence, R.J., Going, C., Markus, M., 2004,"Using high-resolution satellite images for post-earthquake building damage assessment: a study following the 26 January 2001 Gujarat earthquake", Earthquake Spectra, Vol.20(1), pp.145–170.

[14] Sakamoto, M., Takasago, Y., Uto, K., Kakumoto, S., Kosugi, Y., Doihara, T., 2004, "Automatic detection of damaged area of Iran earthquake by high-resolution satellite imagery", IEEE International Geoscience and Remote Sensing Symposium, Vol. 2, pp. 1418–1421.

[15] Gamba, P., Dell Acqua, F., Odasso, L., 2007, "Object-oriented building damage analysis in VHR optical satellite images of the 2004 tsunami over Kalutara, Sri Lanka", 2007 Joint Urban Remote Sensing Event, pp.1–5.

[16] Yusuf, Y., Matsuoka, M., Yamazaki, F., 2001," Damage assessment after 2001 Gujarat earthquake using Landsat-7 satellite images", Journal of the Indian Society of Remote Sensing",Vol.29(1),pp.233–239.

[17] Jin, X., Davis,C. H., 2005, "Automated building extraction from high-resolution satellite imagery in urban area using structural contextual, and spectral information", EURASIP Journal on Applied Signal Processing, Vol. 14, p.p. 2196–2206.

[18] Guindon, B., 1997, "Computer-based aerial image understanding: are view and assessment of its application to plan metric information extraction from very high resolution satellite images", Canadian Journal of Remote Sensing, Vol. 23, No. 1, pp. 38–47.

[19] Koc, D., Turker, M., 2005, "Automatic Building Detection from High Resolution Satellite Images", Recent Advances in Space Technologies, pp. 617-622.

[20] Estrada, M., Yamazaki, F., Matsuoka, M., 2000, "Use of Landsat images for the identification of damage due to the 1999 Kocaeli, Turkey earthquake", In proceeding of the 21st Asian Conference on Remote Sensing, Singapore, pp. 1185–1190.

[21] Dong, Y., Yu, D., Zang, J., 2009, "Preliminary Hazard Degree Assessment of Urban Earthquake Disaster Based on High Resolution Satellite Image", Urban Remote Sensing Joint Event, pp. 1-5.

[22] Falco, N., Mura, M.D., Bovolo, F., Benediktsson, J.A. and Bruzzone, L., 2010, "Study on the capabilities of morphological attribute profiles in change detection on VHR images", Proceedings of SPIE, pp. 7830-7841.

[23] Elbaz, A., Mohamed, R.M., Farag, A.A., 2005, "Shape-constraint for accurate segmentation in remote sensing imagery", Proceeding of International Conference on Information Fusion, Vol.2, pp. 1154-1161.

[24] Comaniciu, D., Meer, P., 2002, "A robust approach toward feature space analysis," IEEE Transaction on Pattern Analysis and Machine Intelligence, Vol. 24, pp. 603-619.

[25] Benedictsson, J.A., Pesaresi, M., Arnason, K., 2003, “Classification and Future Extraction for Remote Sensing Images From Urban Areas Based on Morphological Transformations”, IEEE Transaction on Geoscience and Remote Sensing, Vol.41, No. 9, pp. 1940-1949.

[26]www.dartmouth.edu/doc/idl/html_6.2/Overview_of_Extracting_and_Analyzing_Image_Shapes.html (Accessed on 2010/10/22)

Chapter 2

STATE OF THE ART

2.1 Introduction

This chapter makes a brief survey of existing methods for building extraction using airborne or space borne optical imagery without any kind of auxiliary data (e.g. SAR, LiDAR, hyperspectral data, DEM, etc.). Particularly approaches employing the texture analysis, feature extraction and pattern recognition procedures are reviewed. Throughout this investigation advantages and disadvantages of those methods are also examined. Most of the examined optical data sets consist of panchromatic imagery coming from both airborne as well as high resolution satellite sensors. These surveyed methodologies of image segmentation for building extraction from monocular images can be classified into two categories: edge-driven and region-driven. The mathematical morphological transformation based approaches for urban classification also become popular in the past decade.

2.2 Existing Methods for Building Extraction from Optical Imagery

2.2.1 Edge driven methods

The edge driven methods are mainly focused on the delineation of building boundary and segmentation of building roof polygons or faces. Building detection using entropy threshold basis selection method was investigated by Banjanin et al [1]. They proposed a method that allows for the restriction of the decomposition complexity by increasing the threshold factor with the use of edge enhancement as a simple and effective feature extraction method. Nevatia et al. also introduce a linear feature extraction and description [2]. Elaborating on the Gaussian scale-space, applied a technique for detecting whether the difference between two consecutive scales are too large, based on the changes the sign of the Laplacian of the image undergoes with the increasing standard deviation of the Gaussian filter. Sobel and Roberts are also well-known feature extraction methods that show reliable extraction performance through the implementations [3],[4].

However, these edge detection based methods still need a improvements. Figuring out that how to combine the benefits of the fine scales (spatial accuracy) with those of the coarse ones (reliable classification). Choosing a threshold very low will lead to many false edge counts and contribute to noise in the processed image. Conversely, if the threshold is set too high, there will be a discontinuity in the detected edges. Many of these works showed short comes in their application in hazardous areas as shown, because of the influence of the errors occurred by debris, none of them provides an automatic method for determining the numerical values for the scales.

The classical Hough transformation is used to detect lines, circles, ellipses, etc., whereas the generalized form can be used to detect features that cannot easily be described in an analytical approach. By applying the advanced Hough transformation the geometric properties of the buildings such as building edge and corners are extracted [5]. The research shows that by using Hough transformation for building extraction has many advantages, such as the better handling of noisy data, easy adjustment of level detail of the output data, the ability to force certain geometric properties into the extracted buildings and possibility to bridge gaps, meaning that building corners that might not to be visible in the imagery can be determined accurately [6]. Easy implementation, simple conceptuality, adaptive use of many types of spatial configuration (not only lines), handles missing and occluded reliable data are the advantages of the Hough transform.

However, this methodology has certain weaknesses when dealing with radiometrically heterogeneous building roof, large roof shadow, complex building geometry, the combination and arrangement of many compound buildings. Other disadvantages of this method are its computational complexity for a number of building roof parameters, its focus for a single type of object at one time, inability to determine the length and position of a line segment and the difficulties in separating co-linear line segments. Most of the approaches are based on stepwise, interactive Hough transform in combination with an adaptive feature extraction algorithm.

2.2.2. Region driven methods

Comparing with edge driven methods, region driven methods have significant advantages, because it can incorporate with prior high level knowledge such as texture, intensity and shape models. A wide range of region driven based techniques and algorithms have been proposed for building extraction from high resolution imagery in early research. Considering both radiometry and geometry, large populations of these building extraction methodologies are categorized as region growing, clustering and segmentation, shadow based identification and so forth.

For the initial segmentation of optical images, seeded region growing algorithms are also used to find homogeneous roof regions in the image. The seed points are regularly distributed over the image with a seed point raster size set with respect to the expected roof size. The seeded region growing algorithm starts at a pixel position of each seed point and compares this pixel value with the neighboring pixel values. If the neighboring pixel values lie inside a given tolerance, the neighboring pixels belong to the same region as the seed point. The region growing goes on recursively with the newly added pixels and ends, when no new neighboring pixels which fulfill the condition can be found [7]. The main drawback of this technique is that it is difficult to distinguish proper building in the image.

There are many traditional schemes for image clustering and segmentation. Without prior information, building extraction methods for airborne or space borne images based on algorithms are modified by step follows, namely a multi-scaled geometric image analysis, watershed segmentation and region classification. Most of the time these texture clustering algorithms are assumed to be an arduous and complex combination of image processing approaches (e.g. histogram filtering, enhancing, contrast measuring, smoothing, merging etc.) [8, 9].

Most of the recent work on building extraction from high resolution satellite images are based on supervised techniques. These techniques either require a classification based on initial training data to provide hypotheses for the positions and sizes of the candidate building features. The past studies have shown that the supervised classification methods of Support Vector Machine (SVM) [10,11,12] and Maximum Likelihood Classifier (MLC) [13,14] and Neural Network Classifier [9,13,15] provide significantly higher accuracy of the remote sensing images than other approaches (These classifiers are briefly described in the appendix). Concerning the effect of the training sample size on classification accuracy, it can state that increasing the training sample size increase the accuracy. However, due to the fact that in each of these classification methods, the location of the training samples in the feature space is more important than the training sample size and the largest increase was not observed to be more than 3% [10].

When illuminated by the sun, buildings cast shadows around them. Several studies have been conducted on the relationship between a building and its cast shadow [16, 17]. Generally, there are two types of methods for extracting shadows of structures: property-based and model-based methods [20]. Property-based methods obtain shadows by making use of specific properties of shadow images, such as color, texture and shape [20,21,22,23].

However, in visual interpretation of the scene, less than 60% of shadows were really caused by buildings; others were by trees, debris or even clouds. The studies of building extraction or damage assessments using only shadow analysis show low accuracy detections and needed an integrated shadow analysis with optional data.

2.2.3 Mathematical morphology

Segmentation and classification of images at pixel level have been widely used in the field of advance remote sensing. The generally accepted technique reported in the literature is to assign the pixels to a semantically meaningful class based on spectral similarity and local textural features. Feature extraction by various methods has been extensively employed to incorporate the spatial information about the local neighborhood of a pixel. Another approach for the integration of spatial information is the use of mathematical morphology by Soille [24]. Pesaresi and Benediktsson introduced multi-scale analysis based on Morphological Profiles (MPs; will be detailed in Chaptor. 3) that are formed by the successive application of opening and closing by reconstruction with the increasing size (scales) of the structuring elements (SE) [25]. The successive difference of the MP, the differential morphological profile (DMP), was defined as a feature vector for each pixel. Then, the scale, where the maximum response was observed in the DMP was coded as the probable size of the object underlying the pixel of interest. In addition, each pixel was labeled as convex, concave or flat in accordance with the type of that scale.

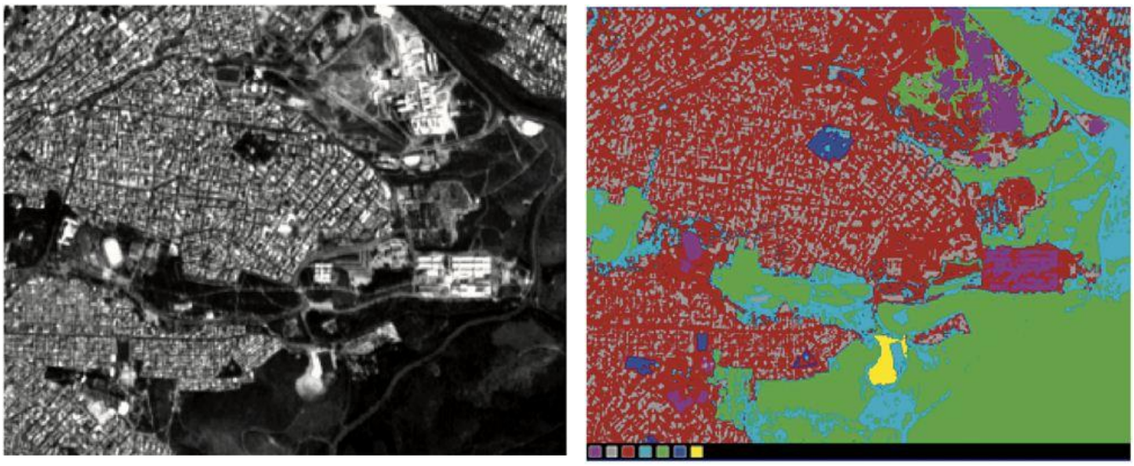

(a) (b)

Fig. 2.1 (a) Original panchromatic image and (b) classification based on the full DMP for each pixel of 16 DMP layers for land cover classification. (Refer [26]).

Many researchers have employed the DMP as a feature vector for each pixel and have performed segmentation and classification based on the similarities of these features. In [26] Benediktsson et al., significant scales were selected from the DMP and used as features for a neural network type classifier. Figure 2.1 (a) shows the conducted agricultural experiment area in a subset of panchromatic image. The classification results of large buildings, small buildings, roads, wetlands, open area inside and outside area are shown in different colors [large building (magenta), small building (gray), streets (cyan), open spaces in the urban areas (dark blue), open space outside urban areas (green), wetland (yellow)] in Figure. 2.1. (b).

A multi-scale hierarchical segmentation was performed based on MP in [27] Akcayet al., where spatial connectedness and spectral homogeneity were utilized at each hierarchical level. The DMP was used in estimating the kernel bandwidths of the mean shift at each pixel and the segmentation results that confirmed the effectiveness compared to fixed bandwidth mean shift segmentation were reported in Aytekin et al., [28]. The common framework of the methods Pesaresi et al., and Benediktsson et al., is the assumption that the maxima of the DMP emulate the sizes and typologies of the underlying structures, i.e., convex, concave or flat. This assumption is generally true for the geometrical and more or less homogenous primitives.

Usually the MM methodology feature extraction method has a problem when applied to the scenes accounting for different urban settlement images of very high spatial resolution. The significant misclassification in the extraction is the models are not included the type or sizes of building [29]. Consequently, the standard method does not explore all aspects of the feature space and more advanced feature selection approaches that give higher accuracies should be investigated. Appropriate feature selection mythology for building extraction also could be used for reducing the misclassification error and computational time.

2.3 Conclusions

From the literature review, it can be concluded that building extraction using optical imagery, especially in hazard areas, is still the subject of ongoing research. The challenges are due to: inaccurate feature extraction using optical images, variety and complexity of building roof, the effects of the ruble in hazardous areas, etc.

Most of the edge driven methods lose corners and miss the edges. There is always some mismatching and only sparse features can be extracted without dense matching. The segmentation task is quite difficult, i.e. deriving the inner and outer boundary of building such as houses with inner courtyards. Although these methods show low accuracy results that might not be directly applicable for feature extraction, due to urban complexity and debris of the hazardous areas. Therefore, preprocessing methods are needed to correctly connect the features and avoid error affection.

The challenge for building extraction of region driven methods is that the buildings are dense and vary greatly in urban environments. Even from VHR airborne images, recovering a complete and accurate numbers of buildings is still a difficult task, especially when extracting building in a hazardous area. Most of the methods were applied to optical images, using the steps of segmentations, and appropriate classification methods such as neural network, support vector machine, etc. The optical images, in particular the robustness of feature matching and feature tracking are reduced by occlusions, illumination changes, limited locations of image acquisition and non textured surfaces. However the existing building extraction algorithms lack a robust and comprehensive feature extraction. The manual building extraction shows quit highly accurate results, but these kinds of techniques are very time consuming [30,31].

The MP based methodology is sufficient enough for classifications, but it has a problem when applied to the scenes accounting for different urban settlements images of very high spatial resolution. The significant misclassification in the extraction is due to the model performative, which did not include the type or sizes of building. Overview of the literature review of damage extraction results shows the difficulties of building extraction in hazardous areas using existing methods, very few studies have conducted so far and it is an urgent need to be developed more accurate and rapid method.

References

[1] Banjanin, B., Gergic, B., Planinsic, P., Cucej, C., 2001,“Entropy-threshold method for best basis selection”, Image and Vision Computing, Vol.19, pp. 477–484.

[2] Nevatia, R., Babu, K.R., 1980,“Linear feature extraction and description Computer Graphics”, Image Process., Vol.13, pp. 257–269.

[3] Canny, J.,1986,“A Computational Approach to Edge Detection”, IEEE Trans.Pattern Analysis and Machine Intelligence, Vol. 8, pp. 679-698.

[4] Bao, P., Zhang,L., Wu,X., 2005,“Canny edge detection enhancement by scale multiplication IEEE Transactions on Pattern Analysis and Machine Intelligence”, Vol.27(9), pp. 1485–1490.

[5] Vozikis, G., Jansa, J., 2008, “Advantages and disadvantages of the Hough transform in the frame of automated building extraction”, International Society for Photogrammetry and Remote Sensing XXIst Congress, Beijing China, pp.719- 724.

[6] Li, G.,Jinlian, A., Wan, Y., 2012, “Automated building extraction based on improved watershed segmentation, mutual information match and snake model”, International Journal of Computer Applications in Technology, Vol.43(2), pp.147 – 154.

[7] Zahra, L., Hamid, E., 2007, “Automated building extraction from high resolution satellite imagery using spectral and structural information based on artificial neural networks”, High-resolution earth imaging for geospatial information, ISPRS Archives, Vol.36(1).

[8] Fei, C., 2011, “Man-made object detection based on texture clustering and geometric structure feature extracting”, International Journal of Information Technology and Computer Science, Vol.2, pp. 9-16.

[9] Sun, X., Fu, K., 2008,“Contextual models for automatic building extraction in high resolution remote sensing image using object based boosting method”, Geoscience and Remote Sensing Symposium, Boston, MA,Vol.2, pp. 437-440.

[10] Turker, M., Son, D.K., 2010,“Building detection from pan-sharpened Ikonos imagery through support vector machines classification”, The International Archives of the Photogrammetry, Remote Sensing and Spatial Information Sciences, Vol.28(8),pp. 841-846.

[11] Huang, X., Zhang, L., and Li, P., 2007,“An adaptive multi-scale information fusion for feature extraction and classification of IKONOS multispectral imagery over urban areas”, IEEE Geoscience and Remote Sensing Letters, Vol.4(4), pp.654-658.

[12] Bellman, C. J., Shortis, M. R., 2000, “Building recognition using wavelet analysis and support vector machines”, Proceedings of SSC2003.

[13] Chen, K., 2002, “Extraction building features from high resolution areal imagery for natural hazards risk assessment”, Geoscience and Remote Sensing Symposium, Vol.4, pp.2039-2041.

[14] Sarp, G., Erener, A.,2008,“Land use detection comparison from satellite images with different classification procedures”, ISPRS Proceeding, Vol.37 (4), pp. 555-558.

[15] Lari, Z., Ebadi, H., 2007,“Automatic Extraction of Building Features from High Resolution Satellite Images Using Artificial Neural Networks, In Proceedings of ISPRS Conference on Information Extraction from SAR and Optical Data, with Emphasis on Developing Countries, Istanbul, Turkey.

[16] Irvin, R.B., McKeown, D.M.J.R., 1989, “Methods for exploiting the relationship between buildings and their shadows in aerial imagery”, IEEE Transactions on Systems, Man and Cybernetics, Vol.19 (6), pp. 1564–1575.

[17] Cheng, F., Thiel, F.H., 1995, “Delimiting the building heights in a city from the shadow in a panchromatic SPOT-image; Part 1.Test of forty-two buildings”, International Journal of Remote Sensing, Vol.16 (3), pp. 409–415.

[18] Turker, M., San,B.T., 2004,“Detection of collapsed buildings caused by the 1999 Izmit, Turkey earthquake through digital analysis of post-event aerial photographs”, International Journal of Remote Sensing, Vol.25 (21), pp. 4701–4714.

[19] Turker, M., Sumer, E., 2008, “Building-based damage detection due to earthquake using the watershed segmentation of the post-aerial images”, International Journal of Remote Sensing, Vol.29 (11), pp. 3073–3089.

[20] Salvador, E., Cavallaro, A., Ebrahimi, T., 2004,“Cast shadow segmentation using invariant color features Computer Vision and Image Understanding”, Vol.95(2), pp. 238–259.

[21] Dare, P.M., 2005, “Shadow analysis in high-resolution satellite imagery of urban areas Photogrammetric Engineering & Remote Sensing”, Vol.71 (2), pp. 169–177.

[22] Sarabandi, P., Yamazaki, F., Matsuoka, M., 2004, “Shadow detection and radiometric restoration in satellite high resolution images”, In: Proceedings of 2004 IEEE International Geoscience and Remote Sensing Symposium, Anchorage, Alaska, USA, pp. 3744–3747.

[23] Sirmacek, B., Unsalan, C., 2008, “Building detection from aerial images using invariant color features and shadow information”, In: Proceedings of the 23rd International Symposium on Computer and Information Sciences (ISCIS 2008), Istanbul, Turkey, pp. 1–5.

[24] Soille, P., 2003,”Morphological Image Analysis: Principles and Applications”, Springer-Verlag, Berlin, pp. 390.

[25] Pesaresi, M., and Benediktsson, J.A., 2001, "A new approach for the morphological segmentation of high resolution satellite imagery", IEEE Transactions on Geoscience and Remote Sensing, Vol.39(2), pp.309–320.

[26] Benediktsson, J. A., Pesaresi, M., Arnason, K., 2003, "Classification and feature extraction for remote sensing images from urban areas based on morphological transformations", IEEE Trans. Geoscience and Remote Sensing,Vol.41(9), pp. 1940-1949.

[27] Akcay, H.G., Aksoy, S.,2008,"Automatic Detection of Geospatial Objects Using Multiple Hierarchical Segmentations," IEEE Transactions on Geoscience and Remote Sensing, Vol.46(7), pp.2097-2111.

[28] Aytekin, O., Ulusoy, I., Halici, U., 2009,"Segmentation of High resolution satellite imagery based on mean shift algorithm and morphological operations", Image and Signal Processing for Remote Sensing XV, Berlin, Germany, doi:10.1117/12.830456.

[29] Jin, X., Davis,C. H., 2005,"Automated building extraction from high-resolution satellite imagery in urban area using structural contextual, and spectral information", EURASIP Journal on Applied Signal Processing, Vol. 14, pp. 2196-2206.

[30] Deichmann, U., Ehrlich, D., Christoper, S., Zeung, G., 2011,"Using high resolution satellite data for the identification of urban natural disaster risk", Global Facility for Disaster Reduction and Recovery, European union and world bank report. pp.1-79.

[31] Saito, K, Spence, R.J.S., Christopher, G., Markus, M., 2004,"Using High-Resolution Satellite Images for Post-Earthquake Building Damage Assessment: A Study Following the 26 January 2001 Gujarat Earthquake", Earthquake Spectra, Vol. 20(1), pp. 145-169.

CHAPTER 3

METHODOLOGY

In this chapter the fundamental concept of connected operators and proposed methods are presented. In particular, the definition of opening and closing by reconstruction is recalled and reviewed. The proposed thesis framework shown in Figure.3.(a) consists of several methods that are explained in this chapter.

The proposed method of morphological operators are presented in section 3.1. In section 3.2, the novel building roof pattern recognition method based on hit-or-miss transform is described. Another novel approach of building roof reconstruction using extended morphological operators and classification method are explained in section 3.3. Here the main classification method of Random Forest that we used for building roof extraction is introduced under section 3.4.2. The pre and post event image registration and a novel damaged building block identification based on Discrete Fast Fourier Transform method are described in section 3.4.3. Finally these two methods are combined for higher accurate damage building extraction. All the results are evaluated with existing GIS data as ground truth.

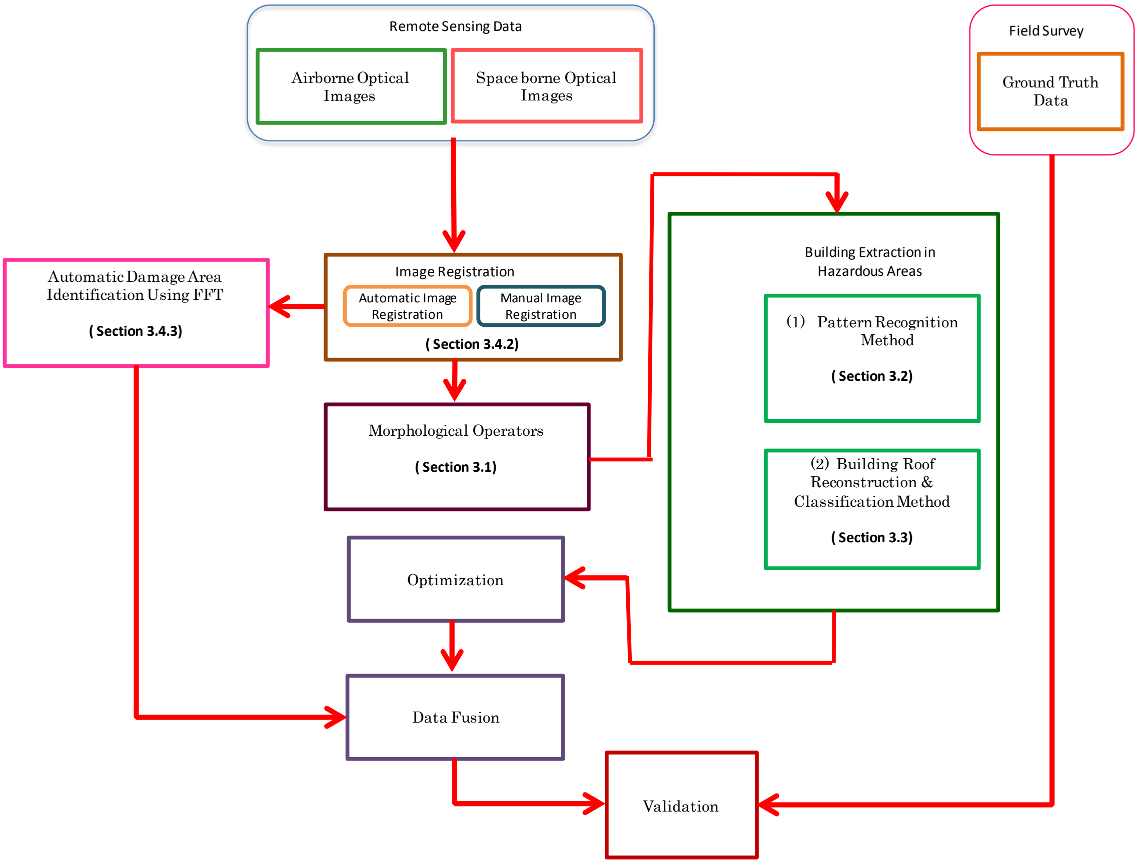

Fig.3 (a) proposed dissertation framework

3.1 Morphological Operators

3.1.1. Fundamental Properties of Morphological Profile

This concept is used to create a feature vector from a single image, f and it is based on the repeated use of the opening and closing operators, which are commonly used in mathematical morphology. Opening and closing by reconstruction is obtained by following erosion and dilation of the original image [1, 2]. Let us consider a grayscale $2D$ image f with discrete single tone pixel values. A morphological neighborhood transformation transforms a pixel p of the image f according to a function ψ and a neighborhood $N(p)$ of p (set of pixels connected to p according to a connectivity rule) [3]. This can be formulated as

$$[\psi(f)](p) = \psi[N(p)] \tag{3.1.1}$$

Obviously, the output of the transform depends on the function ψ and on how the neighborhood N is defined. Usually, the set that defines the neighborhood in such transformations is known as a Structuring Element (SE) and it is defined by a certain shape and a center. The shape is usually a discrete representation of continuous shapes (e.g., lines, rectangles, circles, etc.) on the domain lattice. The center identifies the pixel on which the SE is superposed when probing the image.

The definitions of some fundamental properties of morphological image transformations that will be useful in the following discussion are recalled as below [4].

- *Idempotence*. A transformation ψ is idempotent if the output of the transformation is independent of the number of times it is applied to the image: i.e., $\psi(\psi(f)) = \psi(f)$.
- *Increasingness.*A transformation is said to be increasing if and only if it keeps the ordering relation between images, i.e., $f \le g \Leftrightarrow \psi(f) \le \psi(g) \forall f, g$. The notation $f \le g$ means that $f(p) \le g(p)$ for each pixel p in the definition domain of the images.
- *Extensivity and Anti-extensivity*. A transformation ψ is extensive if, for each pixel, the transformation output is greater or equal to the original image, i.e., $f \le \psi(f)$ .The correspondent property is anti-extensivity and is satisfied when $f \ge \psi(f)$ for all the pixels in the image.

Another fundamental concept is that of the so-called *connected component*. In a grayscale image a connected component (also called a "*flat zone*") is defined as a set of connected iso-intensity pixels. Two pixels are connected according to a connectivity rule. Common connectivity rules are the 4- and 8-connected, where a pixel is said to be adjacent to four or eight of its neighboring pixels, respectively. The connectivity can be extended by more general criteria defining a connectivity class [5].

3.1.2. Opening and Closing by Reconstruction

The two fundamental neighborhood transformations in mathematical morphology are *erosion* and *dilation*. Most morphological operations are based on a selected combination of erosion and dilation. Erosion and dilation are denoted by ε_λ and δ_λ, where λ refers to the structuring element that corresponds to the neighborhood. The erosion or dilation operators transform an input image by giving as output for each pixel p the *infimum* ($\wedge$) or *supremum* ($\vee$) of the intensity values of the set of pixels included by the SE when it is centered on p, respectively. It is important to note that infimum and the supremum are the minimum and maximum of an ordered set, respectively. The definition of the erosion ε_λ of the gray level function using the structuring element λ is defined by the infimum of the values of the grey level function in the neighborhood:

$$\varepsilon_\lambda f(p) = \{\wedge f(p^/) \big| p^/ \in N_G(p) \cup p\} \tag{3.1.2}$$

Here in the Euclidean transforms assume that flat structuring element that corresponds to the neighborhood $N_G(p)$. The dilation δ_λ is similarly defined by the supremum of the neighboring values and the value of $f(p)$

$$\delta_\lambda f(p) = \{\vee f(p^/) \big| p^/ \in N_G(p) \cup p\} \tag{3.1.3}$$

The effect of a dilation using 3×3 SE on a binary image is shown in Figure. 3.1.1 And effect of erosion using 3×3 square structuring element shows on Figure.3.1.2.

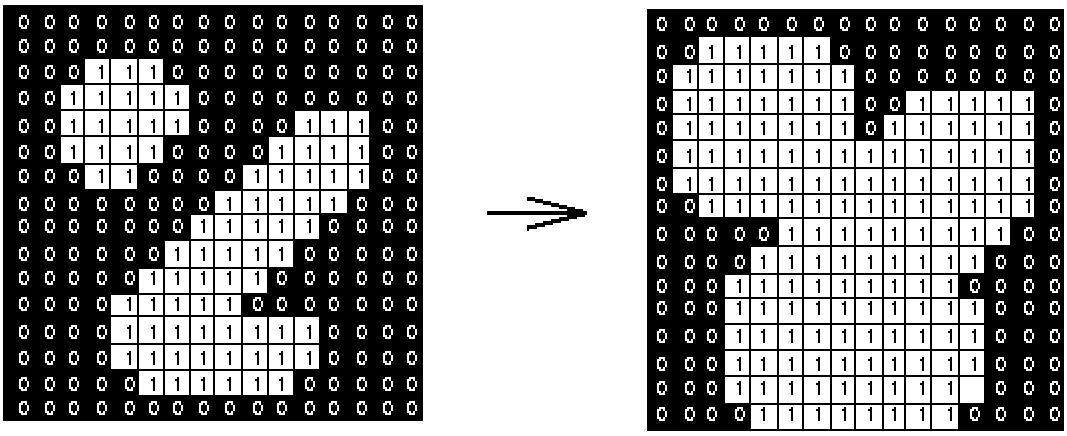

0	0	0	0	0	0	0	0	0	0	0	0	0	0	0	0
0	0	0	0	0	0	0	0	0	0	0	0	0	0	0	0
0	0	0	1	1	1	0	0	0	0	0	0	0	0	0	0
0	0	1	1	1	1	1	0	0	0	0	0	0	0	0	0
0	0	1	1	1	1	1	0	0	0	0	1	1	1	0	0
0	0	1	1	1	1	0	0	0	0	1	1	1	1	0	0
0	0	0	1	1	0	0	0	0	1	1	1	1	1	0	0
0	0	0	0	0	0	0	0	1	1	1	1	1	0	0	0
0	0	0	0	0	0	0	1	1	1	1	1	0	0	0	0
0	0	0	0	0	0	1	1	1	1	1	0	0	0	0	0
0	0	0	0	0	1	1	1	1	1	0	0	0	0	0	0
0	0	0	0	1	1	1	1	1	0	0	0	0	0	0	0
0	0	0	0	1	1	1	1	1	1	1	1	0	0	0	0
0	0	0	0	1	1	1	1	1	1	1	1	0	0	0	0
0	0	0	0	0	1	1	1	1	1	1	0	0	0	0	0
0	0	0	0	0	0	0	0	0	0	0	0	0	0	0	0

0	0	0	0	0	0	0	0	0	0	0	0	0	0	0	0
0	0	1	1	1	1	1	0	0	0	0	0	0	0	0	0
0	1	1	1	1	1	1	1	0	0	0	0	0	0	0	0
0	1	1	1	1	1	1	1	0	0	1	1	1	1	1	0
0	1	1	1	1	1	1	1	0	1	1	1	1	1	1	0
0	1	1	1	1	1	1	1	1	1	1	1	1	1	1	0
0	1	1	1	1	1	1	1	1	1	1	1	1	1	1	0
0	0	1	1	1	1	1	1	1	1	1	1	1	1	1	0
0	0	0	0	0	1	1	1	1	1	1	1	1	1	0	0
0	0	0	0	1	1	1	1	1	1	1	1	1	0	0	0
0	0	0	1	1	1	1	1	1	1	1	1	0	0	0	0
0	0	0	1	1	1	1	1	1	1	1	1	1	0	0	0
0	0	0	1	1	1	1	1	1	1	1	1	1	0	0	0
0	0	0	1	1	1	1	1	1	1	1	1	1	0	0	0
0	0	0	1	1	1	1	1	1	1	1	1		0	0	0
0	0	0	0	1	1	1	1	1	1	1	1	0	0	0	0

Fig.3.1.1. Effect of dilation using a 3×3 square structuring element

Source:- Hyper media image reference/The University of Edinburgh.

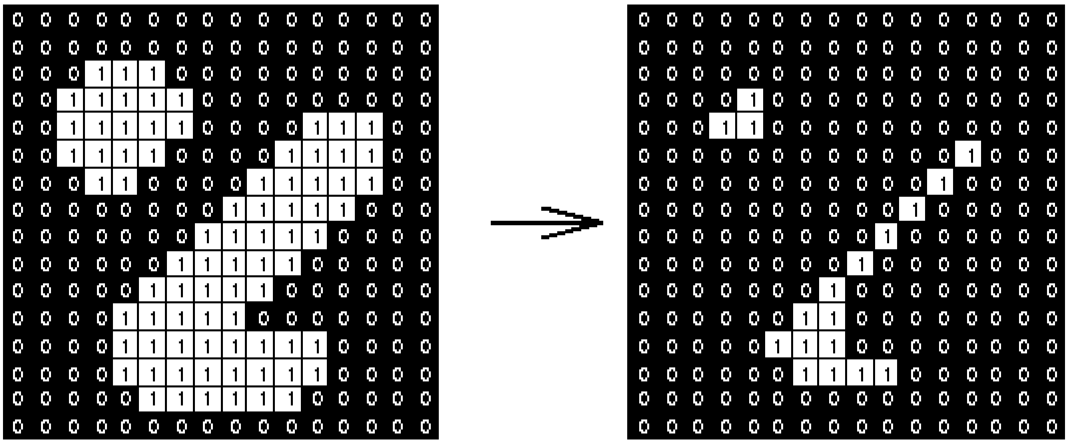

0	0	0	0	0	0	0	0	0	0	0	0	0	0	0	0
0	0	0	0	0	0	0	0	0	0	0	0	0	0	0	0
0	0	0	1	1	1	0	0	0	0	0	0	0	0	0	0
0	0	1	1	1	1	1	0	0	0	0	0	0	0	0	0
0	0	1	1	1	1	1	0	0	0	0	1	1	1	0	0
0	0	1	1	1	1	0	0	0	0	1	1	1	1	0	0
0	0	0	1	1	0	0	0	0	1	1	1	1	1	0	0
0	0	0	0	0	0	0	0	1	1	1	1	1	0	0	0
0	0	0	0	0	0	0	1	1	1	1	1	0	0	0	0
0	0	0	0	0	0	1	1	1	1	1	0	0	0	0	0
0	0	0	0	0	1	1	1	1	1	0	0	0	0	0	0
0	0	0	0	1	1	1	1	1	0	0	0	0	0	0	0
0	0	0	0	1	1	1	1	1	1	1	1	0	0	0	0
0	0	0	0	1	1	1	1	1	1	1	1	0	0	0	0
0	0	0	0	0	1	1	1	1	1	1	0	0	0	0	0
0	0	0	0	0	0	0	0	0	0	0	0	0	0	0	0

0	0	0	0	0	0	0	0	0	0	0	0	0	0	0	0
0	0	0	0	0	0	0	0	0	0	0	0	0	0	0	0
0	0	0	0	0	0	0	0	0	0	0	0	0	0	0	0
0	0	0	0	1	0	0	0	0	0	0	0	0	0	0	0
0	0	0	1	1	0	0	0	0	0	0	0	0	0	0	0
0	0	0	0	0	0	0	0	0	0	0	0	1	0	0	0
0	0	0	0	0	0	0	0	0	0	0	1	0	0	0	0
0	0	0	0	0	0	0	0	0	0	1	0	0	0	0	0
0	0	0	0	0	0	0	0	0	1	0	0	0	0	0	0
0	0	0	0	0	0	0	0	1	0	0	0	0	0	0	0
0	0	0	0	0	0	0	1	0	0	0	0	0	0	0	0
0	0	0	0	0	0	1	1	0	0	0	0	0	0	0	0
0	0	0	0	0	1	1	1	0	0	0	0	0	0	0	0
0	0	0	0	0	0	1	1	1	1	0	0	0	0	0	0
0	0	0	0	0	0	0	0	0	0	0	0	0	0	0	0
0	0	0	0	0	0	0	0	0	0	0	0	0	0	0	0

Fig.3.1.2. Effect of erosion using a 3×3 square structuring element.

Source:- Hyper media image reference/The University of Edinburgh.

Closing can sometimes be used to selectively fill in particular background regions of an image. Whether or not this can be done depends upon whether a suitable structuring element can be found that fits well inside regions that are to be preserved, but doesn't fit inside regions that are to be removed.

The sequential composition of erosion and dilation leads to the definition of the morphological *opening* and *closing* transformations. Morphological Opening γ_{λ} of an image f by a structuring element λ is defined as the erosion of f by λ followed by the dilation of the eroded output by $\bar{\lambda}$, the reflected structuring element with respect to λ:

$$\gamma_\lambda f(p) = \delta_{\bar{\lambda}}[\varepsilon_\lambda f(p)] \tag{3.1.4}$$

In contrast, a Morphological Closing φ_λ of an image f by a structuring element λ is defined as the dilation of f by λ followed by the erosion of the dilated output by the reflected structuring element $\bar{\lambda}$:

$$\varphi_\lambda f(p) = \varepsilon_{\bar{\lambda}}[\delta_\lambda f(p)] \tag{3.1.5}$$

While the output of erosion would have an effect on all the brighter structures independent of the size, an opening flattens bright objects that are smaller than the size of the structuring element and, because of dilation, mostly preserves the bright large areas. A similar conclusion can be drawn for darker structures when a closing is performed. The terms brighter and darker are considered with respect to the surroundings gray tones. The morphological opening and closing operators usually lead to severe effects on the image, especially when the SE is large with respect to the size of the structures in the image. Moreover, with these operators, the geometrical characteristics of the structures can be distorted or completely lost. This is obviously an undesirable effect when information on the objects of interest has to be retrieved after the filtering.

The erosion can be used to eliminate small clumps of undesirable foreground pixels, e.g. salt noise, quite effectively; it has the big disadvantage that it will affect all regions of foreground pixels indiscriminately. The opening gets around this by performing both an erosion and a dilation on the image. The effect of opening can be quite easily visualized. Imagine taking the structuring element and sliding it around inside each foreground region, without changing its orientation. All pixels which can be covered by the SE with the SE being entirely within the foreground region will be preserved. However, all foreground pixels which cannot be reached by the SE without parts of it moving out of the foreground region will be eroded away. After the opening has been carried out, the new boundaries of foreground regions will all be such that the SE fits inside them, and so further openings with the same element have no effect. The property is known as idempotence. The effect of an opening on a binary image using a 3×3 square SE is illustrated in Figure 3.1.3. One of the uses of dilation is to fill in small background color holes in images, e.g. pepper noise. One of the problems with doing this, however, is that the dilation will also distort all regions of pixels indiscriminately. By performing an erosion on the image after the dilation, i.e. a closing, we reduce some of this effect. The effect of closing can be quite easily visualized. Imagine taking the SE t and sliding it around outside each foreground region, without changing its orientation. For any background boundary point, if the SE can be made to touch that point, without any part of the element being inside a foreground region, then that point remains in background. If this is not possible, then the pixel is set to foreground.

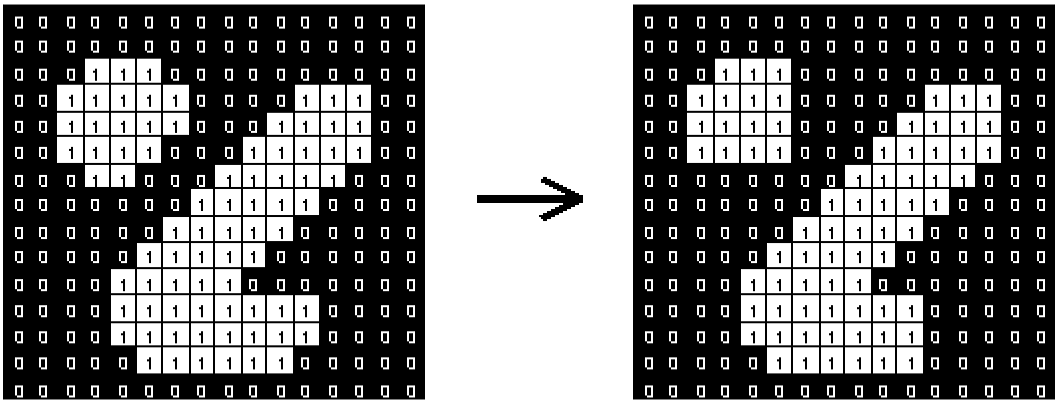

Fig.3.1.3. Effect of opening using a 3×3 square structuring element.

Source:- Hyper media image reference/The University of Edinburgh.

After the closing has been carried out the background region will be such that the structuring element can be made to cover any point in the background without any part of it also covering a foreground point, and so further closings will have no effect. This property is known as idempotence. The effect of a closing on a binary image using a 3×3 square structuring element is illustrated in Figure.3.1.4.

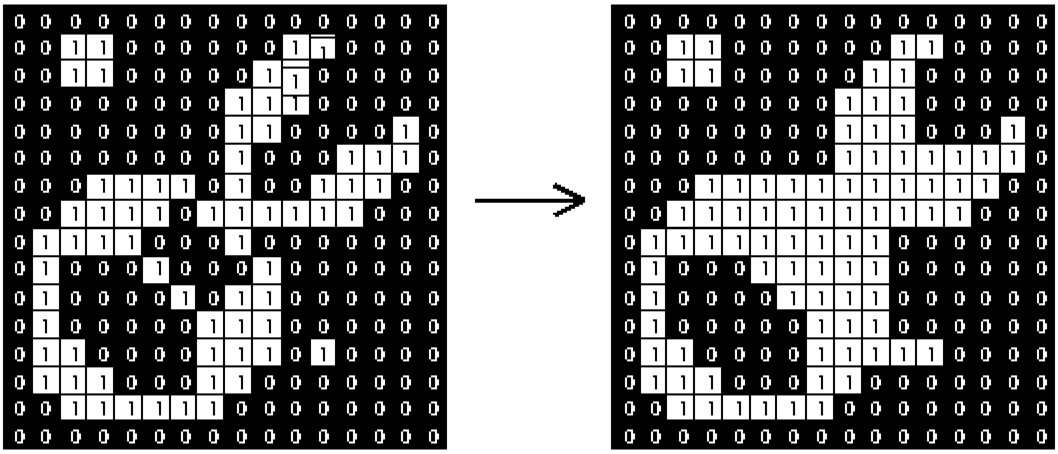

Fig.3.1.4. Effect of closing using a 3×3 square structuring element.

Source:- Hyper media image reference/The University of Edinburgh.

However, the classical morphological opening and closing operators usually lead to severe effects on the image especially when the SE is large with respect to the size of the structures in the image. Moreover, with these operators, the geometrical characteristics of the structures can be destroyed or completely lost. This is obviously an undesirable effect when information on the objects of the interest has to be retrieved after the filtering. Morphological operators based on the geodesic reconstruction can effectively process the image by overcoming this issue. This is achieved by either completely removing or preserving the connected components in the image according to their interaction with the SE of the transformation. In greater detail, if a component in the image is larger than the SE then it will be unaffected, otherwise it will be merged to a brighter or darker adjacent region depending upon whether a closing or opening is respectively applied.

An Opening by Reconstruction (OR) is performed in two separated phases and can be formally defined as:

$$\gamma_{\lambda}^{*} f(p) = \delta_{(n)}^{f(p)}(\varepsilon_{\lambda} f(p)) = Rec(\varepsilon_{\lambda} f, f) \qquad (3.1.6)$$

The first transformation, $\varepsilon_{\lambda} f(p)$ is an erosion of the image f with an SE of size λ, which defines the size of the opening. This aims at creating the so called marker image for the reconstruction operation. The second phase performs a reconstruction by dilation, $\delta_{(n)}^{f(p)}(\varepsilon_{\lambda} f(p)) = Rec(\varepsilon_{\lambda} f, f)$, of the marker image taking as reference mask f. This operation is an iterative procedure that applies geodesic dilation (which is defined as the infimum of the elementary dilation and the mask image) on the marker image until idempotence $(\delta_{(n)}^{f} = \delta_{(n+1)}^{f})$:

$$Rec(\varepsilon_{\lambda} f, f) = \delta_{(n)}^{f(p)}(\varepsilon_{\lambda} f(p)) = \underbrace{\delta_{(1)}^{f(p)} \cdot \delta_{(1)}^{f(p)} \cdot \delta_{(1)}^{f(p)} \cdots\cdots\cdots\cdots \delta_{(1)}^{f(p)}(\varepsilon_{\lambda} f(p))}_{n.times} \qquad (3.1.7)$$

Here the $\delta_{(1)}^{f}$ means dilation one time of the image f. The reconstruction phase permits to fully retrieve all those structures that are not completely suppressed by the erosion and it potentially needs several iterations before reaching stability. By duality, a Closing by Reconstruction (CR) is defined as the reconstruction by erosion of f from the dilation of f using a structuring element of size λ:

$$\varphi_{\lambda}^{*} f(p) = \varepsilon_{(n)}^{f(p)}(\delta_{\lambda} f(p)) = Rec(\delta_{\lambda} f, f) \qquad (3.1.8)$$

It is important to note that the result obtained with operators by reconstruction is less dependent on the shape of the selected structuring element than in the case of morphological opening or closing. Operators by reconstruction are also less severe than the corresponding morphological ones, which can be explained by analyzing the ordering relations between the operators:

$$\gamma_\lambda \le \gamma_\lambda^* \le f \le \varphi_\lambda^* \le \varphi_\lambda \qquad (3.1.9)$$

Here $\gamma_\lambda, \varphi_\lambda, \gamma_\lambda^*, \varphi_\lambda^*$ are the opening, closing, OR with structuring element λ and CR with structuring element λ in the image f. Here in Figure 3.1.5 shows the classical image opening and opening with the reconstruction process. The goal is the reconstruction is aimed to efficiently precisely reconstruct the contours of the objects which have not been totally removed by the filtering process. The mask is the original image and marker is an erosion of the mask.

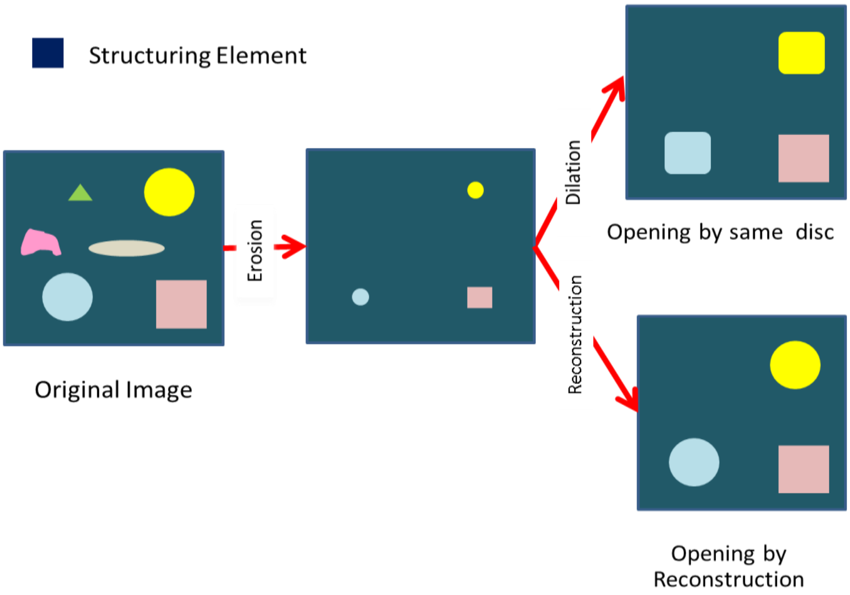

Fig.3.1.5. Classical image opening and opening with reconstruction process.

Figure.3.1.6. shows the radius increment step size of disc (circular) shape SEs.

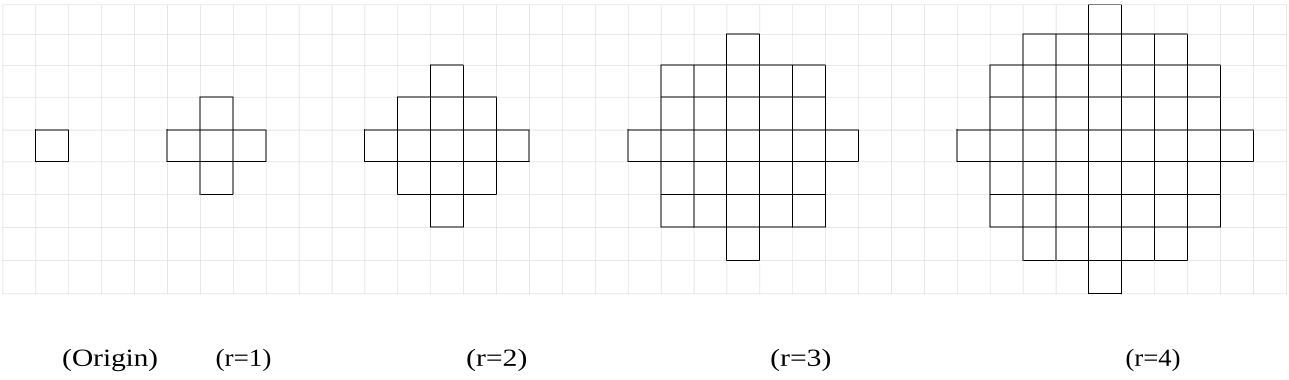

Fig.3.1.6. The circular SE with size in radius (r) =0(origin), 1,2, 3 and 4.

Figure.3.1.7 shows the MP of OR based on the circular shape iteration SE. Similarly

Figure.3.1.8 shows the MP of CR based on circular shape iteration structuring elements. The original gray color image consists of the post tsunami event of Ishinomaki area, Miyagi prefecture, Japan. The profile series has been generated by three iterations of the disk shape structuring element radius size (r) of 3,7,11 and15.


(a) r=3 (b) r=7 (c) r=11 (d) r=15

Fig.3.1.7. MP based on disk (circular shape) structuring element of opening. Each profile has been generated by three iterations of the SE size (a) r=3, (b) r=7, (c) r=11 and (d) r=15 respectively.


(a) r=3 (b) r=7 (c) r=11 (d) r=15

Fig.3.1.8. MP based on a disk (circular shape) structuring element of closing. Each profile has been generated by three iterations of the SE size (a) r=3, (b) r=7, (c) r=11 and (d) r=15 respectively.

3.1.3. Differential Morphological Profile for panchromatic images

In this section the *Differential Morphological Profile* (DMP) is reviewed. In general, for real applications, it is unlikely that filtering of an image with a single opening and closing by reconstruction completely models the spatial information in a complex scene. This behavior might limit the capability of the image analysis. A common procedure is to filter an image with a sequence of many different SEs in order to extract more information on the scene. Granulometries and anti-granulometries are examples of this approach. A granulometry is obtained by the application of a series of opening with SEs of increasing size and fixed shape. An anti-granulometry is generated analogously by closing operators. By analyzing the result of a granulometry one is able to gather information on the size distribution of those objects brighter than the surrounding background. Thus, we can refer to this procedure as a multi-scale analysis. When performing such an analysis with operators based on the geodesic reconstruction, the progressive simplification of the image does not come at the detriment of the geometry of those objects that are not canceled from the image. The morphological profiles are based on these ideas. MP were introduced by Pesaresi et al., and Benediktsson et al., in and defined as a concatenation of an anti-granulometry followed by agranulometry performed by closing and opening by reconstruction transformations, respectively [6]. The anti-granulometry is referred as closing profile $\prod_{\varphi_\lambda}$ and the granulometry as opening profile $\prod_{\gamma_\lambda}$. The opening and closing by reconstruction can be considered as lower-level opening and upper-level closing operations [7]. The idea of the multi-scale segmentation based on the derivative of the morphological profile, denoted as Differential Morphological Profile (DMP) was developed as

The morphological opening profile of an image f is an array of n opening performed on the original image using SE size λ, and let vector $\prod_{\gamma_\lambda}(f)$ be the *opening profile* defined by

$$\prod_{\gamma_\lambda}(f) = \{\prod_{\gamma_\lambda}(f) : \prod_{\gamma_\lambda}(f) = \gamma_\lambda^*(f), \forall\lambda \in [1,......,n]\} \qquad (3.1.10)$$

Thus, by duality, the morphological *closing profile* $\prod_{\varphi_\lambda}$ composed by the operator by n level, can be denoted by as a vector

$$\prod_{\varphi_\lambda}(f) = \{\prod_{\varphi_\lambda}(f) : \prod_{\varphi_\lambda}(f) = \varphi_\lambda^*(f), \forall\lambda \in [1,......,n]\} \qquad (3.1.11)$$

Above the $\gamma_0^*(f) = \varphi_0^*(f) = f$ for $\lambda = 0$ [7]. Therefore, both the opening and closing profiles are generated by opening and closing by reconstruction operators with the image f taken the mask and with SEs of fixed shape and size increasing on the n levels. When a closing profile and an opening profile, both of size n, are joined a Morphological Profile (MP) is obtained. The MP is of size $2n$, because when the opening and closing profiles are equal to the original image. The opening profile can also be defined as a granulometry [8] made with opening by reconstruction, while the closing profile can be defined as anti-granulometry made with closing by dual reconstruction.

$$MP_\lambda(f) = \left\{ \begin{array}{lll} \prod_{\varphi_\lambda}(f), & \lambda = (n+1-i), & i \in [1, n]; \\ \prod_{\gamma_\lambda}(f), & \lambda = (i-n), & i \in [n+1, 2n]; \end{array} \right\} \tag{3.1.12}$$

The differential morphological profile is defined as a vector where the measure of the slope of the opening-closing profile is stored for every step of an increasing SE series. The *differential opening profile* Δ_{γ_λ} is defined as the vector

$$\Delta_{\gamma_\lambda}(f) = \left\{ \Delta_{\gamma_\lambda} : \Delta_{\gamma_\lambda} = \prod_{\gamma_{\lambda-1}} - \prod_{\gamma_\lambda} \right\} \quad \lambda \in [1,.....n]; \tag{3.1.13}$$

By duality, the *differential closing profile* Δ_{φ_λ} is the vector

$$\Delta_{\varphi_\lambda}(f) = \left\{ \Delta_{\varphi_\lambda} : \Delta_{\varphi_\lambda} = \prod_{\varphi_\lambda} - \prod_{\varphi_{\lambda-1}} \right\} \quad \lambda \in [1,.....n]; \tag{3.1.14}$$

Generally, the *differential morphological profile* or the DMP can be written as the vector

$$DMP_\lambda(f) = \left\{ \begin{array}{lll} \Delta_{\varphi_\lambda}(f), & \lambda = (n+1-i), & i \in [1, n]; \\ \Delta_{\gamma_\lambda}(f), & \lambda = (i-n), & i \in [n+1, 2n]; \end{array} \right\} \tag{3.1.14}$$

with equal to the total number of iterations, $i = 1,2...,2n$ and n are the total number of iterations, and the size of the morphological transform. Near the central position of the DMP vector, it has responded for the derivative calculated using smaller SEs, while at the beginning (position) and at the end (position), it records the response for the greatest SEs in the closing and opening profiles, respectively. Therefore, if observe a centered DMP, it can argue that small structures are present in the image. On the other hand, an unbalanced DMP (either on the left or right side) indicates the presence of larger structures. These larger structures are either darker [high response in the closing profile] or lighter [higher response in the opening profile] than the surroundings. Generally speaking, the signal response recorded in the DMP gives information about the size and the type of the structures in the image by observing the placement of the area of the DMP histogram. The size is the distance from the center of the DMP, while the type of a structure (darker or lighter than the surrounding ones) can be argued by observing on which side it is placed in the histogram of the DMP vector values. While the above-mentioned approaches do not require a particular metric for the morphological transforms, the DMP approach requires the use of granulometry and anti-granulometry made by opening and closing by reconstruction, using a geodesic metric [8]. Here the Figure.3.1.9 and 3.1.10 show the creation of DMP from opening and closing with increasing SEs. Examples of morphological profile based on disk (circular shape) SE of opening profile series has been generated by four iterations of the SE size λ (a) =original gray color image, (b) $\lambda=3$, (c) $\lambda=7$ and (d) $\lambda=11$ from a panchromatic gray color space borne image are shown on Figure.3.1.11 and 3.1.12. DMP for four information classes are given in Figure.3.1.13 and 3.1.14 for a panchromatic IKONOS image of the Sichuan area in China. In Figure.3.1.15, it can be seen that strikingly different characteristics are achieved for the different classes and shows the DMP vector of attributes for each pixel.

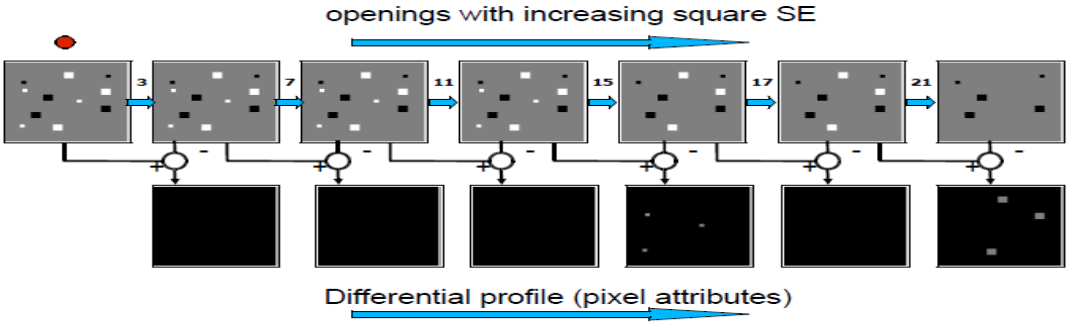

Fig.3.1.9. Creation of DMP from opening with increasing SE.● Mark shows the original image in the left side.(Source-*Introduction to Mathematical Morphology, NTNU*)

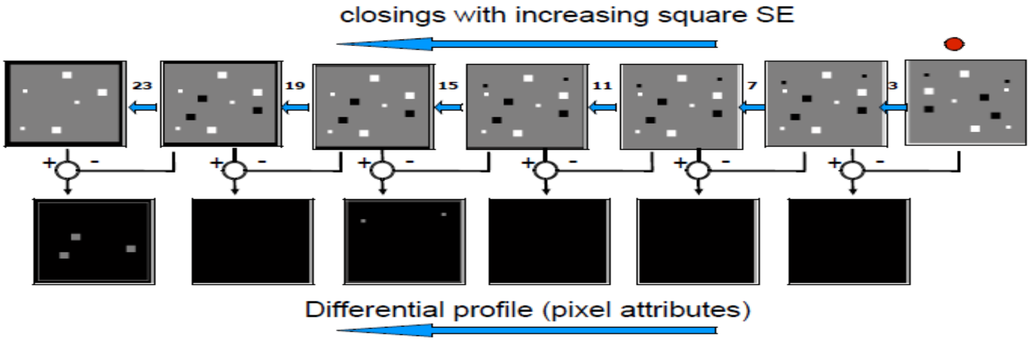

Fig.3.10. Creation of DMP from closing with increasing SE. ●Mark shows the original image in the right side. (Source—*Introduction to Mathematical Morphology, NTNU*)

Therefore, the use of the differential profiles should help in discrimination. However, a lot of redundancy can be seen in the profiles, i.e., the information from all the channels may not be necessary. Thus, feature extraction or feature selection from the differential profiles is of interest.

(a) Original (b) λ =3 (c) λ =7 (d) λ =11

Fig.3.1.11. MP based on a square shape SE of opening. The profile series has been generated by three iterations of the structuring element (SE) size (a), Original image, (b) λ =3, (c) λ =7 and (d) λ =11.

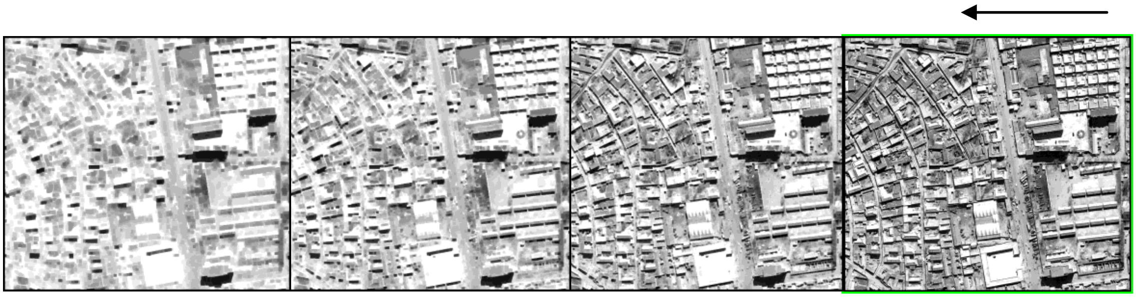

(a) λ =11 (b) λ =7 (c) λ =3 (d) Original

Fig.3.1.12. MP based on a square shape SE of closing. The profile series has been generated by three iterations of the SE size (a) λ =11, (b) λ =7, (c) λ =3 and (d) = original gray color image.

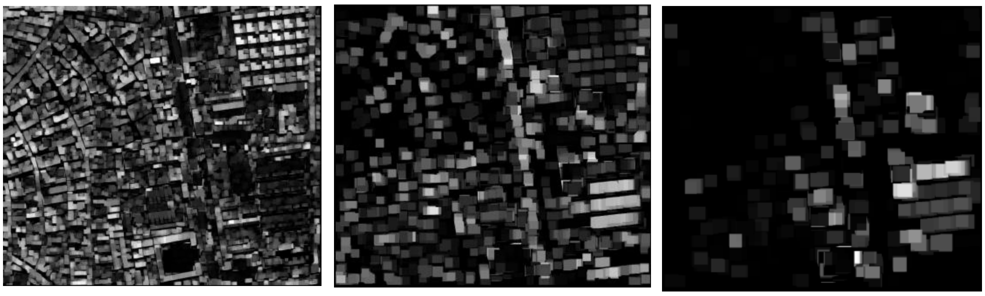

(a) λ =3 (b) λ =7 (c) λ =11

Fig.3.1.13. DMP based on the square shape SE of opening. The profile series has been generated by three iterations set of the SE size (a) λ =3 (b) λ =7 and (c) λ =11.

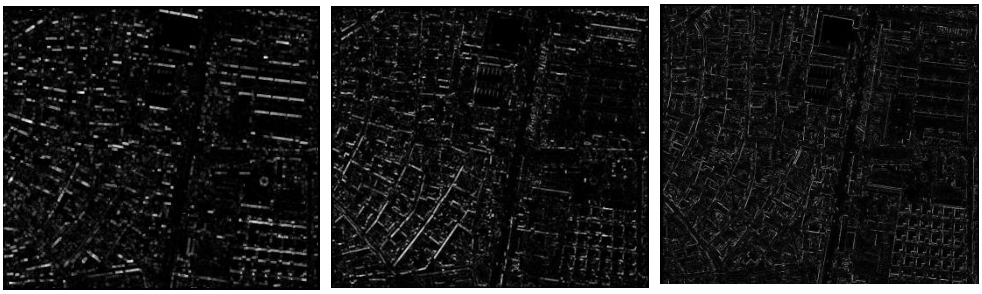

(a) λ =3 (b) λ =7 (c) λ =11

Fig.3.1.14. DMP based on the square shape SE of closing. The profile series has been generated by three iterations set of the SE size (a) λ =3, (b) λ =7 and (c) λ =11.

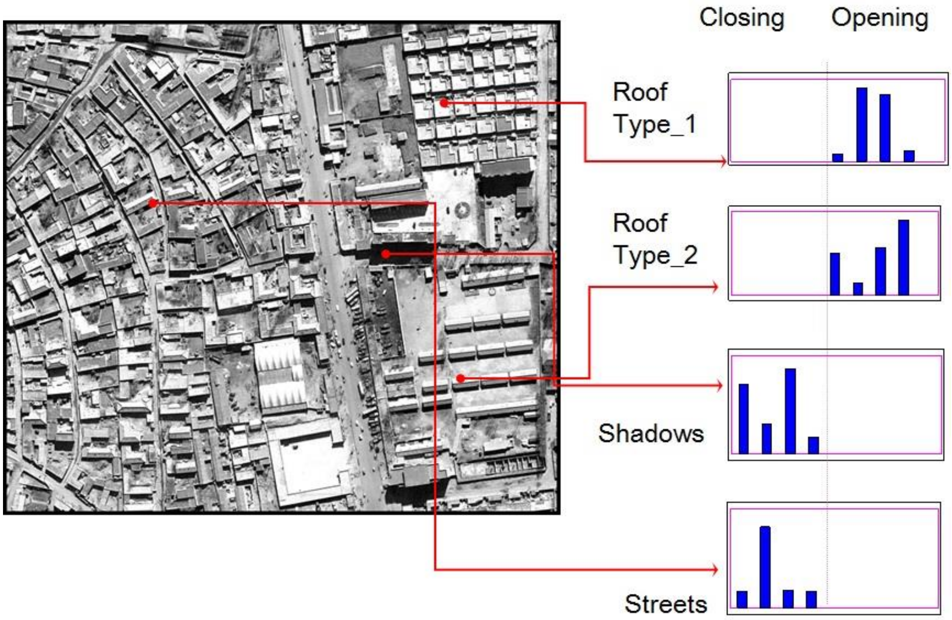

Fig.3.1.15. The DMP vector of attributes for each pixel

3.2 Building Roof Pattern Recognition with Template Matching.

The development of the MM operators to identify the building in the urban areas using gray color images is discussed in this section. Figure.3.2.1 shows the flow chart of the work. First the vectored profiles were created using morphological opening and closing by reconstruction with different SEs. The DMP employs a set of image operators to extract and analyze image components based on the shape and size of quasi-homogeneous regions in the image. Then the vectored structuring functions were filtered and generated the binary images. Finally the extended morphological Hit-or-Miss (HTM) transform is applied with different templates of shape and sizes with optimization process for building identification.

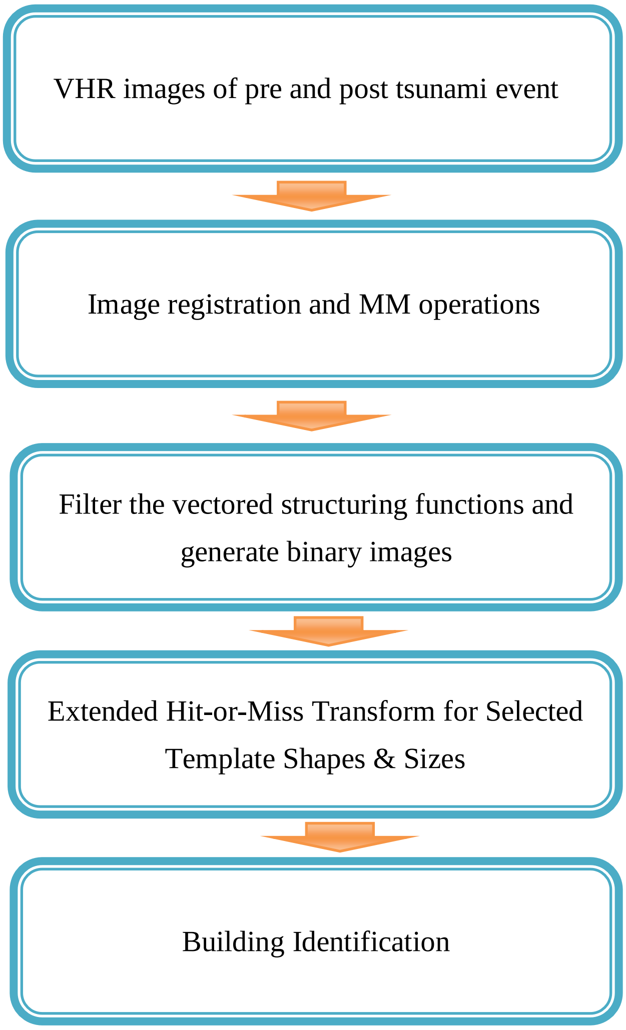

Fig.3.2.1. Flow chart of the study.

3.2.1 MM Operations

The differential morphological profile is defined as a vector where the measure of the slope of the opening-closing profile is stored for every step of an increasing SE series (see section 3.1). Usually the closing profile has influence the dark side of the building roof, shadow and other urban structures such as roads, trees, line and point features, because of these reasons, in this study, we only consider the opening profile range that would contain the possible building roof in the image, and also for this would be avoided the over-counting both of the high intensity the part and the low intensity part of the roof separately as two buildings. The *differential opening profile* Δ_{γ_λ} is defined as the vector with selected square shape SE $\lambda \in [7,11,15,19]$;

$$\Delta_{\gamma_\lambda}(f) = \{ \Delta_{\gamma_\lambda} : \Delta_{\gamma_\lambda} = \Pi_{\gamma_{\lambda-1}} - \Pi_{\gamma_\lambda} \} \quad \lambda \in [7,11,15,19]; \qquad (3.1.13)$$

Figure.3.2.2 shows the gray color images of tsunami hazardous Ishinomaki City area Miyagi Prefecture, Japan, before (IKONOS) and after (Quick Bird) the 2011 tsunami event. Post event GeoEye-1 that consists of 0.5m channel was converted to 1m resolution, while pre event IKONOS image has 1m resolution itself.

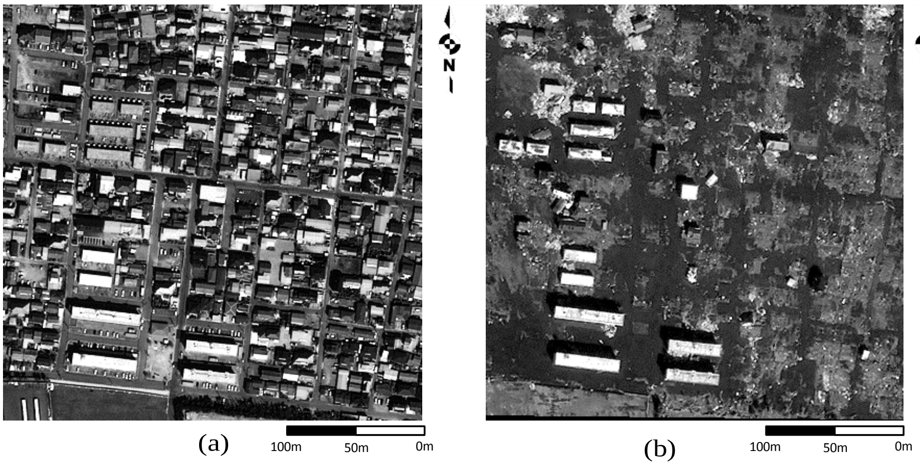

(a) (b)

Fig.3.2.2. Pre generated gray color images from IKONOS and Quick Bird satellite that contain Ishinomaki area before (a) and after (b) the tsunami event.

The differential morphological profiles with λ = 7 (a, d), 11 (b, e) and 15 (c, f) square shape SEs are shown in Figure.3.2.3 respectively. Images (a) to (c) represent the structural decomposition of the pre-event image DMP and (d) to (f) represents post event DMP. The images have been visually enhanced and the derivative has been calculated relative to a series generated by 3 iterations of the elementary SE with 7, 11, 15 and 19 rectangular shape roof.

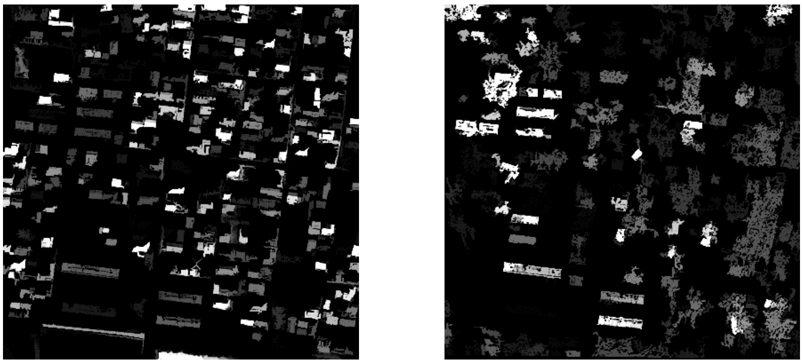

(a) Opening λ = 7 (d) Opening λ = 7

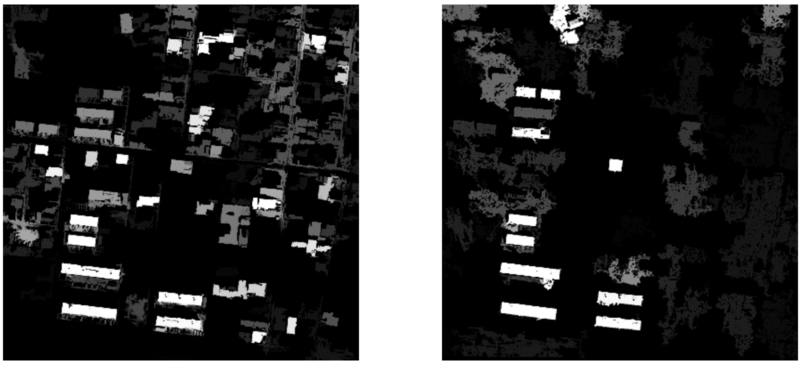

(b) Opening λ = 11 (e) Opening λ = 11

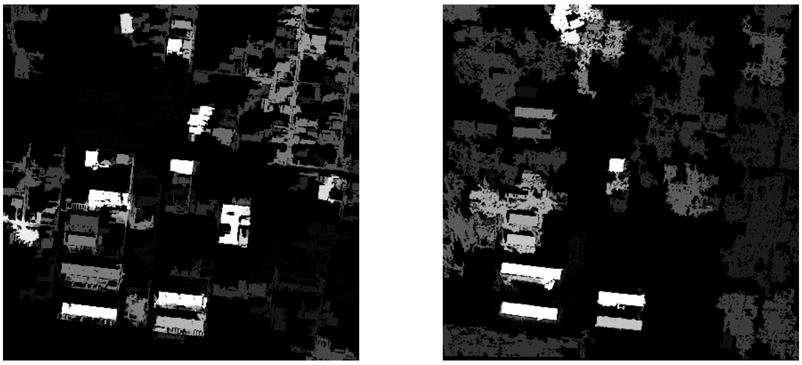

(c) Opening λ = 15 (f) Opening λ = 15

Fig.3.2.3. Images (a) to (c) represent the structural decomposition of the pre-event image DMP and (d) to (f) represents post event DMP. The images have been visually enhanced. The derivative has been calculated relative to a series generated by 4 iterations of the elementary SE with 7, 11 and 15 rectangular shape roofs. The differential opening profile with λ = 7(a, d), 11(b, e) and 15(c, f) are shown above respectively.

3.2.2 Generation of binary images

Selected threshold value (t_{γ_λ}) that depending on each iteration of γ_λ was applied for pre generated DMP. Binary image f'_λ series with different structure elements that contain 0 or 1 pixel values are built up using threshold function $T_{t_{\gamma_\lambda}}$ and Δ_{γ_λ}.

$$f'_\lambda(p) = [T_{t_{\gamma_\lambda}}(\Delta_{\gamma_\lambda}(f))](p) = \left\{ \begin{array}{ll} 1, & \text{if } t_{\gamma_\lambda} \le \Delta_{\gamma_\lambda}(f(p)) \\ 0, & \text{Otherwise} \end{array} \right\} ; \lambda \in [7,11,15,19]; \quad (3.2.1)$$

Assuming the gray pixel value range to be {0,.., 255} in each profile of the Δ_{γ_λ}, here the threshold value $T_{t_{\gamma_\lambda}}$ is set to 70 and it is enough for the building roof to be determined empirically. There are four differential morphological opening profiles that are created using square SE size 7 to 19 (increasing step size is equal to 4). The SE that less than 7 is not reliable to use, because they consist of the noise of small shadows and building rubble. The image binarization threshold was applied to each DMP profile for noise reduction to avoid misclassification. Figure.3.2.4 shows the binarized images of both pre and post event differential morphological opening profiles. The segmentation threshold value was set to 70 DN value and then the template matching based on Hit or miss transform method was applied to extract correspond building roofs.

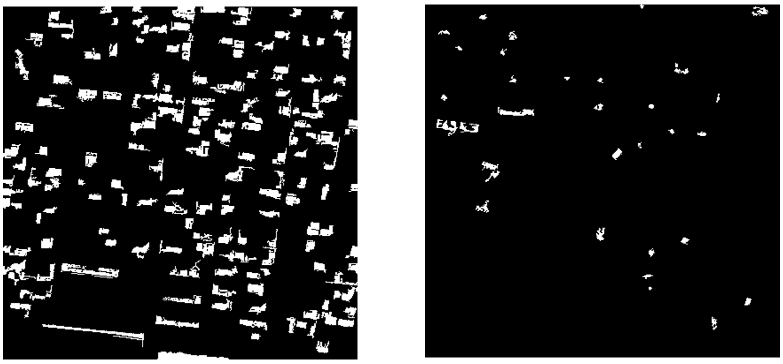

(a) Opening λ =7

(d) Opening λ =7

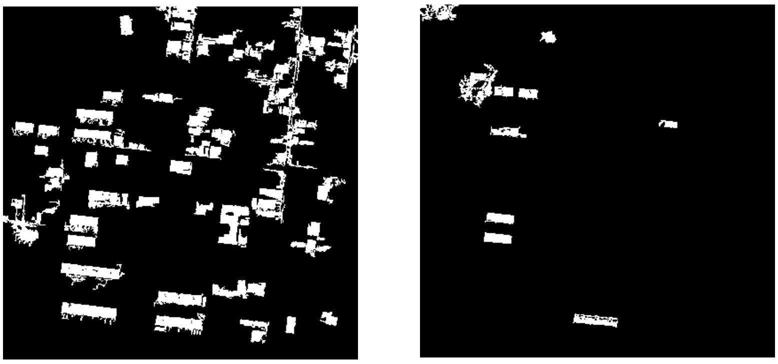

(b) Opening λ = 11

(e) Opening λ =11

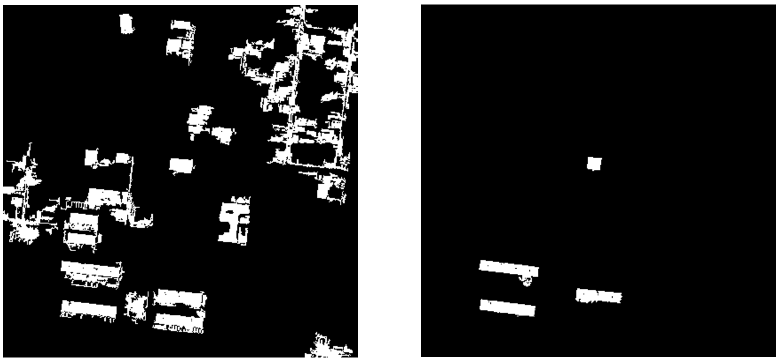

(c) Opening λ = 15

(f) Opening λ =15

Fig.3.2.4. Images (a) to (c) represent the binarized structural decomposition of the pre-event image DMP and (d) to (f) represents post event DMP. The images have been visually enhanced. The derivative has been calculated relative to a series generated by 3 iterations of the elementary SE with 7, 11 and 15 rectangular shape roofs. The differential opening profile with λ = 7(a, d), 11(b, e) and 15(c, f) are shown above respectively.

3.2.3 Hit-or-miss transform for binary case

The Hit or Miss Transform (HMT) is a morphological based technique which usually can be used for template matching of binary images in digital image processing. The standard HMT is a powerful tool for locating objects which are noise free in both background (BG) and foreground (FG) regions, they do not exhibit internal texture and where objects have well defined edges [9]. For the binary case, HMT is capable of recognizing objects in an image using the complementary pair of structuring elements of BG and FG which search for the shape and its complement in the case of successful feature detection [10, 11].

However, despite its potential usefulness, very few applications of the HMT have been proposed until now, because it is not straightforward for grey-level images. HTM usually fails in the presence of noise since signals which should be detected do not precisely match the geometry of the templates used to probe the image for those shapes. Therefore, usually this pattern recognition technique is applied for binary images which are not corrupted by noise.

The classical existing pattern recognition methods need a long processing pipeline such as segmentations, feature computation, filtering, clustering, classification, etc., and most of the techniques would not be adaptive directly with DMP. The HTM is a morphological based adaptive method to DMP based approaches and it is strong enough for fixed feature extraction (e.g. urban infrastructures, non-moving vehicles, ect.) in comparison with other methods. In this section we tested the capacity of building extraction in very noisy environments in hazardous areas and discuss the Structuring Element Template (SET) size and shapes used to improve their robustness.

The HMT, of a set of pixel p by a composite Structuring Element Template (SET) $\eta = (\eta_{FG}, \eta_{BG})$ is the set of points, p, such that when the origin of η coincides with p, η_{FG} fits $g(p)$ while η_{BG} fits $g(p)^c$:

$$HMT_{\eta}[g(p)] = \left\{ p \mid (\eta_{FG})_p \subseteq g(p), (\eta_{BG})_p \subseteq g(p)^c \right\} \tag{3.2.2}$$

where the η_{FG} is the foreground and η_{BG} is the background of the selected structuring element template (SET) η. The $g(p)^c$ is represented the complement of image $g(p)$ respectively. (see Figure.3.2.5(a) and Figure.3.2.5(b)).

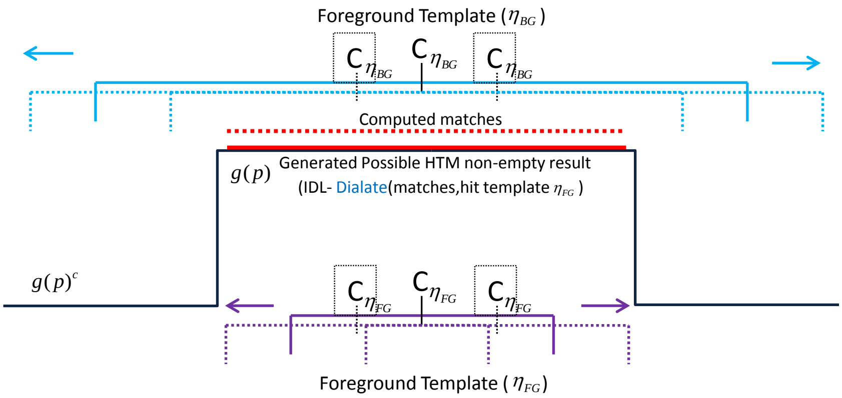

Fig.3.2.5 (a) Generation of the possible HTM result for one object.

Here the Figure.3.2.5 (a) shows the generation of one possible HTM non-empty result at every location for one object, where both the η_{FG} fits entirely within $g(p)$ and the η_{BG} fits the entirely within $g(p)^c$, the component of $g(p)$. It is common to assume that the hit structure template and the miss structure template arguments are disjoint and templates not in their union as *don't-cares*. The $C_{\eta_{FG}}$ and $C_{\eta_{BG}}$ are represent the centers of the complement of η_{FG} and η_{BG} respectively.

Fig.3.2.5(b) Image (a) shows the input binary image $g(p)$, (b) the sought template with η_{FG} foreground in black, η_{BG} background in white, and the output of Eq. 3.2.2. Image (c) shows the HMT results of Image (a) due to the sought template (b).

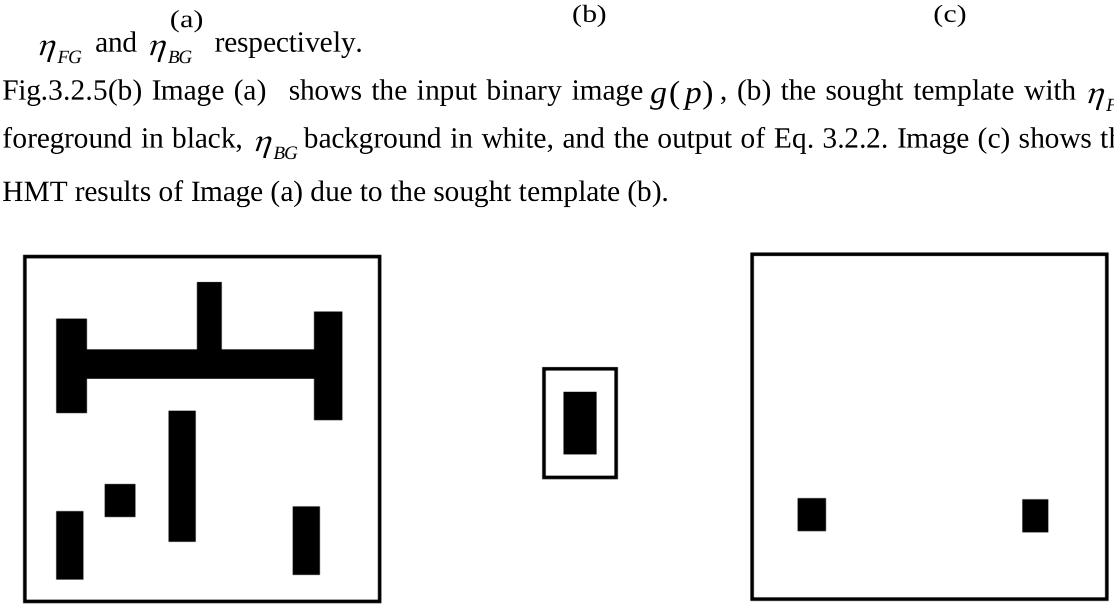
(a) (b) (c)

Applying the HMT for binarized DMP can be defined as follows

$$HMT_{\eta}[DMP_{\lambda}(f(p))] = \{p \mid (\eta_{FG})_p \subseteq DMP_{\lambda}(f(p)), (\eta_{BG})_p \subseteq DMP_{\lambda}(f(p))^c\} \qquad (3.2.3)$$

Here the DMP_λ is defined in eq.3.1.14. The different combinations of $\eta = (\eta_{FG}, \eta_{BG}); \lambda > \eta_{FG}, \lambda < \eta_{BG}$ of flat shape disk, triangle, square and rectangular structuring elements template SET are applied and tested for damage free building extraction which consists of 7, 11, 15, 19 size of structuring elements λ in DMP of the testing area. The tested η_{FG} are always fixed with λ and η_{BG} are increased by 2 as following sequence of i.

$$HMT_\eta[DMP_\lambda(f(p))] = \left\{ \begin{array}{lll} HMT_\eta[DMP_{\lambda=7}(f(p))], & \eta_{FG} = 3, & \eta_{BG} = i, i \in [5,7,..,21] \\ HMT_\eta[DMP_{\lambda=11}(f(p))], & \eta_{FG} = 7, & \eta_{BG} = i, i \in [7,9,..,23] \\ HMT_\eta[DMP_{\lambda=15}(f(p))], & \eta_{FG} = 9, & \eta_{BG} = i, i \in [9,11,..,25] \\ HMT_\eta[DMP_{\lambda=19}(f(p))], & \eta_{FG} = 11, & \eta_{BG} = i, i \in [11,13,..,27] \end{array} \right\} \quad (3.2.4)$$

3.2.4. Optimization the shape and size of the templates.

Several optimizations to improve algorithm performances will be highlighted in this section. For types of templates disk (round), triangular, square and rectangular were applied with different size of foreground and background sizes. Figure.3.2.6 shows the four types of templates and Figure.3.2.7 shows the foreground and background sets that applied for building recognition. The relevance of the HMT that might be matched with building shapes are shown in Figure.3.2.8 in case of rectangular SE.

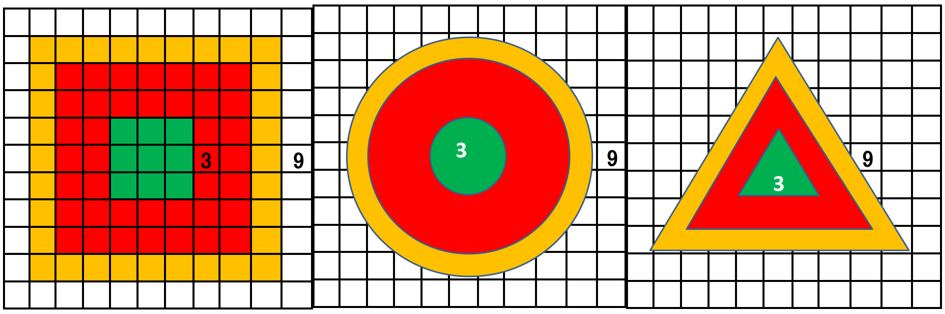

(a) (b) (c)

(continue)

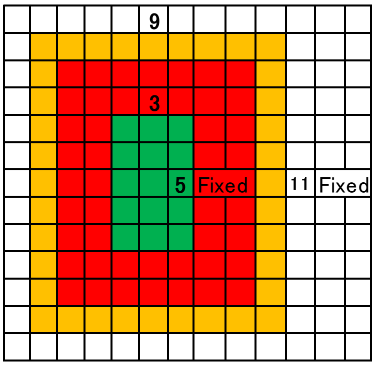

(d)

Fig.3.2.6. Selected SET size and shape for Hit-or-Miss Transform. Here in the visual interpretation of foreground ($\eta_{FG}=3$), background ($\eta_{BG}=9$) and Possible coincide shape of the building roof of SE λ show in green, yellow and red color respectively.

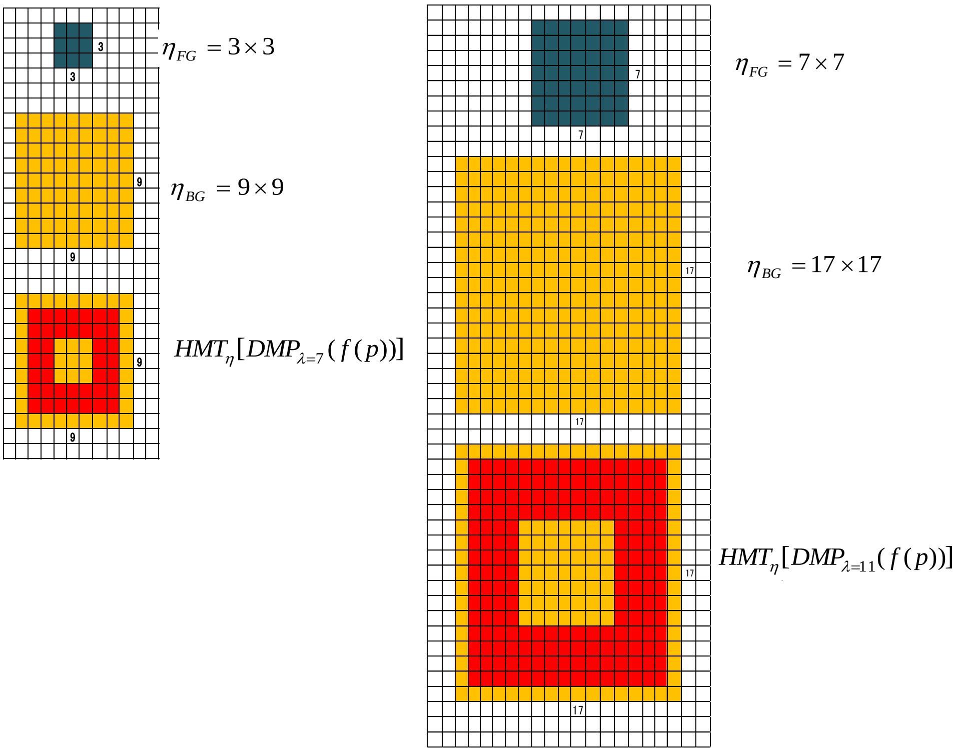

Fig. 3.2.7. Illustrate two applications of the binary HMT to detect building roof with possible extensions for square shape SE $\lambda = 7$ (Foreground $\eta_{FG} = 3$, Background $\eta_{BG} = 9$) and for SE $\lambda = 11$ (Foreground$\eta_{FG} = 7$, Background $\eta_{BG} = 17$) template windows. The Top images represent the foreground η_{FG} in green color, origin of the image is at the center of the squares. The middle images show the background η_{BG} in yellow, with the same origin as η_{FG} . And the bottom images show the possible extraction of building roof size in red color.

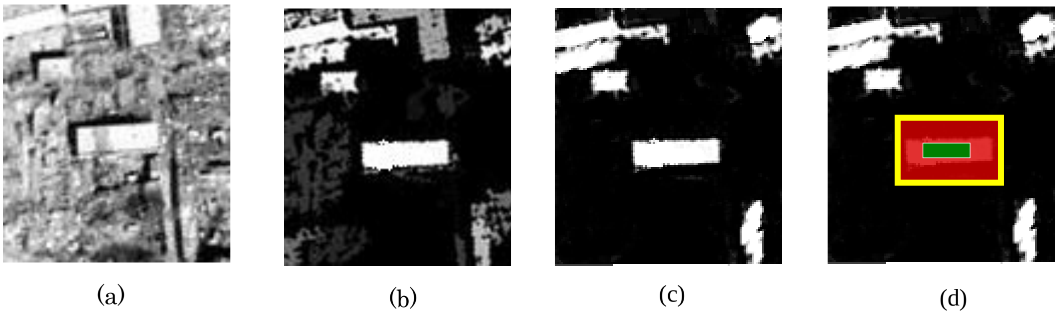
(a) (b) (c) (d)

Fig.3.2.8. Relevance of the HMT for imperfect building shapes; (a) original gray color panchromatic image, (b) DMP applied image, (c) binarized image and (d) application of the HMT for the image. In the image (d), the size of SET shows the background η_{BG} in yellow, foreground η_{FG} in green and the possible coincidate shape of the building roof with the uncertain area is located in between show in red color respectively.

The results of this section 3.1, including the SET characteristic and behaviour with the binarized differential morphological profile on building extraction is described under section 4.1.

3.3 Building Roof Reconstruction and Classification

The basic assumption in the segment based classification is to identify the roof on building which have not been subjected to damage roof intact. To segment the airborne images before the classification, the DMP method developed in section 3.1.3 is used.

3.3.1 Morphological Building Roof Reconstruction

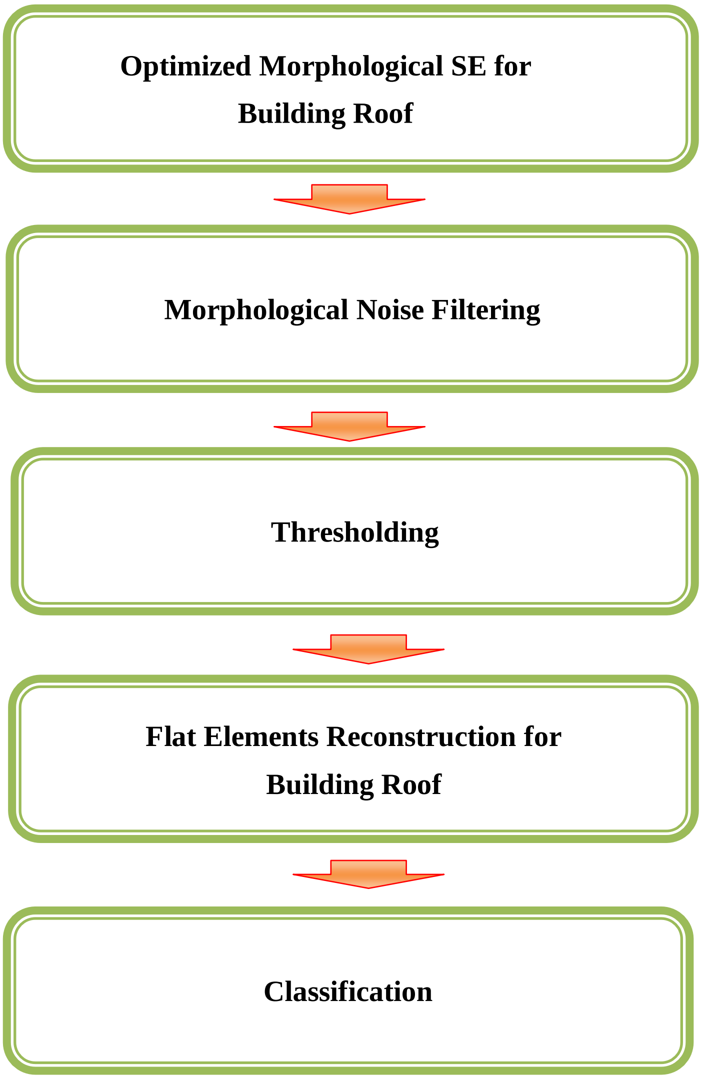

Fig.3.3.1. Flow chart of the building roof reconstruction process.

For the building roof identification without noise the differential morphological profile is extended as follows. Here Figure 3.3.1 shows the novel approach of building roof identification methodology. First, we selected morphological structuring element vector series of SE = 3, 5,7,9,11,13,15,17,19 for the process that optimized for building. All of the building structures in the image have a high response to one of a given SE size in this series, and lower response for other SE sizes, depending on the interaction between the SE size and the size of the building structure.

The DMP usually contains noise of unnecessary features and some building structures have low response with SE that is difficult to identify. For these reasons, in exploratory or more complex cases, it should be a good idea to use an extended morphological approach for building identification. The proposed process consists of several steps for extraction of every possible building structure in the image. These extended morphological profile approaches for building identification include the steps of noise filtering, thresholding and flat structure element reconstruction especially for building roof and classification. The process is described as follows.

(a) Noise Filtering

We applied selected difference derivation profiles with different SE sizes as defined in a vector format, where the measure of the slope of the opening-closing profile is stored for every step of an increasing SE series. For the roof extraction in the candidate area, the *differential opening profile* Δ_{γ_λ} is defined as the vector

$$\Delta_{\gamma_\lambda}(f) = \left\{ \Delta_{\gamma_\lambda} : \Delta_{\gamma_\lambda} = \prod_{\gamma_{\lambda-1}} - \prod_{\gamma_\lambda} \right\} \quad \lambda \in [3,5,....,21]; \qquad (3.3.1)$$

By duality, the *differential closing profile* Δ_{φ_λ} is the vector

$$\Delta_{\varphi_\lambda}(f) = \left\{ \Delta_{\varphi_\lambda} : \Delta_{\varphi_\lambda} = \prod_{\varphi_\lambda} - \prod_{\varphi_{\lambda-1}} \right\} \quad \lambda \in [3,5,....,21]; \qquad (3.3.2)$$

Grayscale erosion with a structuring element will generally darken the image. Bright regions surrounded by dark regions shrink in size, small bright spots (e.g. Salt-and-pepper noise) in images will disappear as they are eroded away down to the surrounding intensity value. The noises of both *differential opening profile* and *differential closing profile* are filtered using erosion as follows,

$$\Omega_{\gamma_\lambda}(f) = \varepsilon_\beta \Delta_{\gamma_\lambda}(f) \quad \lambda \in [3,5,....,21], \beta = 3; \qquad (3.3.3)$$

$$\Omega_{\varphi_\lambda}(f) = \varepsilon_\beta \Delta_{\varphi_\lambda}(f) \quad \lambda \in [3,5,....,21], \beta = 3; \qquad (3.3.4)$$

Here the Ω_{γ_λ} and Ω_{φ_λ} are defined as the noise filtered differential opening profile and noise filtered differential closing profile vectors using grayscale erosion.

(b) Thresholding

In the thresholding step, the selected threshold values t_{γ_λ} and t_{φ_λ} for iteration of γ_λ and φ_λ, are applied to noise filtered differential morphological profile vector (Ω_{γ_λ} and Ω_{φ_λ})images to extract possible building structures and avoid unnecessary feature extraction (eg. Shadow, watershed, roads, debris, large scale infrastructures such as road and streets, ect.). The filtered and thresholded DMP vector with different structuring elements, contain pixel values of higher or equal than the selected threshold value. The filtered and thresholded differential of the opening profile $f''_{\gamma_\lambda}(p)$ and differential of the closing profile $f''_{\varphi_\lambda}(p)$ are defined as

$$f''_{\gamma_\lambda}(p) = [T_{t_{\gamma_\lambda}}(\Omega_{\gamma_\lambda}(f))](p) = \begin{Bmatrix} \Omega_{\gamma_\lambda}(p), & \text{if } t_{\gamma_\lambda} \le \Omega_{\gamma_\lambda}(p) \\ 0, & \text{Otherwise} \end{Bmatrix} \quad (3.3.5)$$

$$f''_{\varphi_\lambda}(p) = [T_{t_{\varphi_\lambda}}(\Omega_{\varphi_\lambda}(f))](p) = \begin{Bmatrix} \Omega_{\varphi_\lambda}(p), & \text{if } t_{\varphi_\lambda} \le \Omega_{\varphi_\lambda}(p) \\ 0, & \text{Otherwise} \end{Bmatrix} \quad (3.3.6)$$

Where p is the pixel of the segmented image and the $T_{t_{\gamma_\lambda}}$ and $T_{t_{\varphi_\lambda}}$ are the thresholding functions here. The thresholded and filtered differential of the opening profile and differential of the closing profile are given as $f''_{\gamma_\lambda}(p)$ and $f''_{\varphi_\lambda}(p)$. Assuming the gray pixel value range to be {0,.., 255} in each profile of the Ω_{γ_λ} and Ω_{φ_λ}, here the both threshold values of t_{γ_λ} and t_{φ_λ} are set to 140 and it was enough the building roof to be determined empirically.

(c) Building Roof Reconstruction (BRR) using Flat square SEs (FE)

Filtering process changes the shape of the objects in the image by eroding the boundaries of the objects and enlarging the boundaries of the dark background. In this section we propose a method to recover all possible building objects in the image by dilating each filtered and thresholded differential profile vectors with appropriate Flat (2D) square shape SEs (FE) s. Here the sequential composition dilation of appropriate FE has always obtained using a size of $\lambda+1$ in each iteration vector profile of γ_λ and φ_λ as shown as the eq. 3.3.7 and 3.3.8.

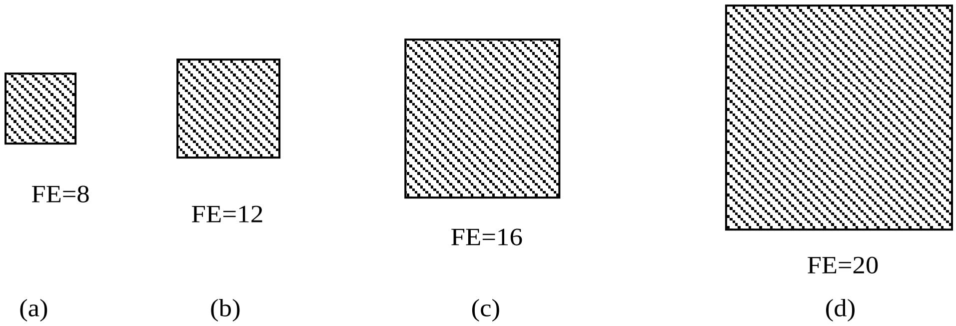

Fig.3.3.2 Selected flat(2D) square shape SEs (FE) for *Building Roof Reconstruction* (BRR). Here the Flat Element size $\lambda+1$ is selected as (a) 8, (b) 12, (c)16 and (d) 20 for SE = 7,11,15 and 19 repetitively.

According to the figure. 3.3.2, the selected FEs are applied to *Building Roof Reconstruction* (BRR). Building Roof Reconstruction (BRR) using flat square structuring elements for roof $\Phi_{\gamma_\lambda}, \Phi_{\varphi_\lambda}$ are defined as,

$$\Phi_{\gamma_\lambda} = \delta_{FE(\lambda+1)} f''_{\gamma_\lambda}(p), \forall\lambda \in [3,5,....,21]; \qquad (3.3.7)$$

for the filtered and thresholded differential opening profile and

$$\Phi_{\varphi_\lambda} = \delta_{FE(\lambda+1)} f''_{\varphi_\lambda}(p), \forall\lambda \in [3,5,....,21]; \qquad (3.3.8)$$

for the filtered and thresholded differential closing profile. Here $\delta_{FE(\lambda+1)}$ is the dilation using with size of $\lambda+1$ *Flat square SEs (FE)* respectively.

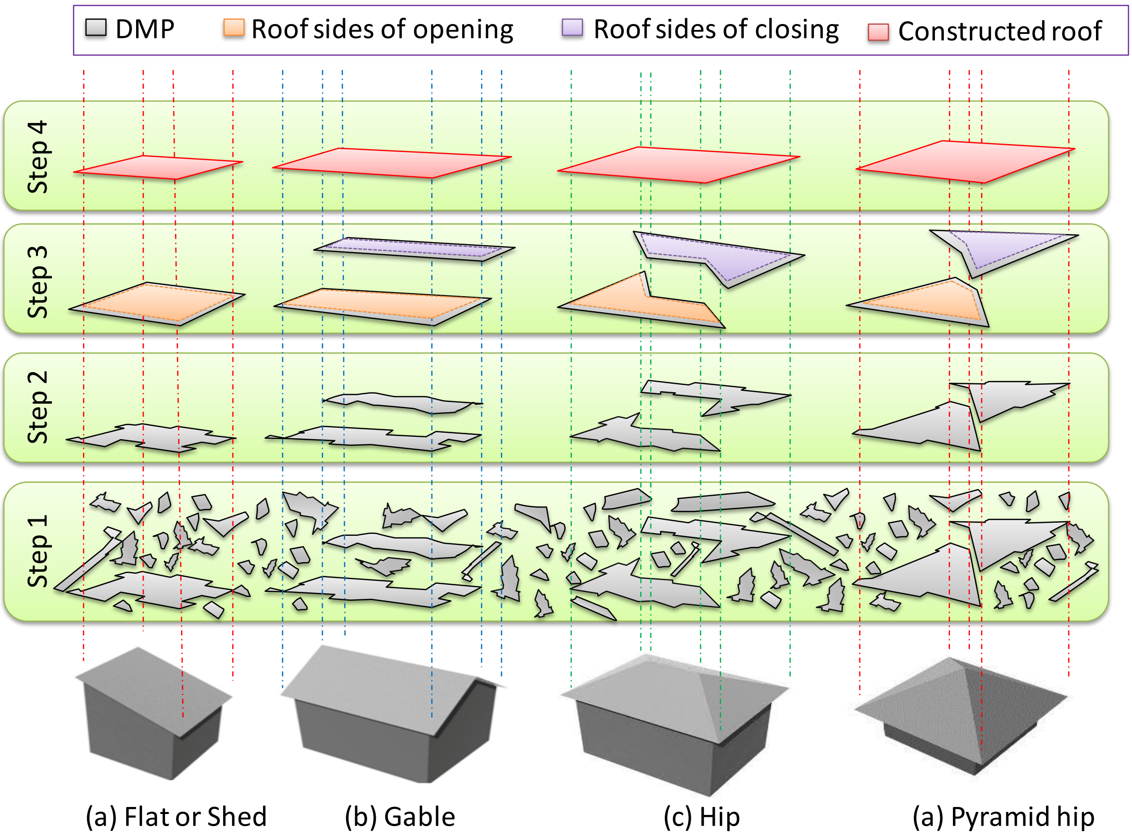

Fig.3.3.3. The process of building roof reconstruction using extended morphological profiles for various kinds of buildings.

Figure.3.3.3 visualizes the various types of building roof extraction using the proposed building roof reconstruction process. In other words the differential morphological profile has been extended to building roof recognition image processing technique, through filtering and thresholding morphological operators with appropriate and adequate SEs. We found the main roof types of Flat or Shed, Gable, Hip and Pyramid hip structures in the candidate area. In the 1st step gray color images of the tsunami hazard site applied the optimized structuring element of the differential morphological profile and create the vector images. Then morphological operators are applied for noise reduction and thresholding process in step 2. In the 3rd step, possible building roof are identified applying adequate dilation process of building roof reconstruction (BRR) method. Finally, a method has been applied called Random Forest (RF) for classification and to extract building. This classification method is explained in the next section and the results of applied to the Ishinomaki area will be given in section 4.2 and 4.3.

The figure. 3.3.4 and 3.3.5 show two examples of Gobel (3.3.4 (a)) and Hip (3.3.5 (a)) shape roof identification process. The images of (b) RGB aerial image, (c) DMP compositioning image, (d) filtering and Thresholding, (e) Morphological roof reconstructing and (f) show the identification the roof using classification respectively.

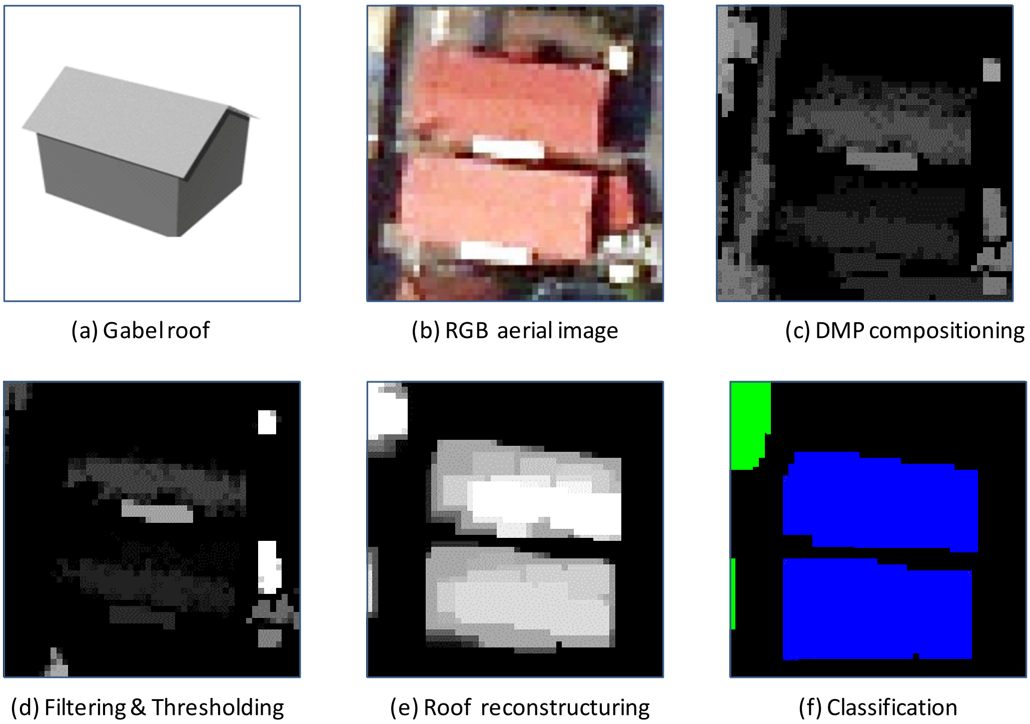
(a) Gabel roof
(b) RGB aerial image
(c) DMP compositioning
(d) Filtering & Thresholding
(e) Roof reconstructuring
(f) Classification

Fig.3.3.4. Identifying the Gabel shape roof.

(a) Hip roof (b) RGB aerial image (c) DMP compositioning

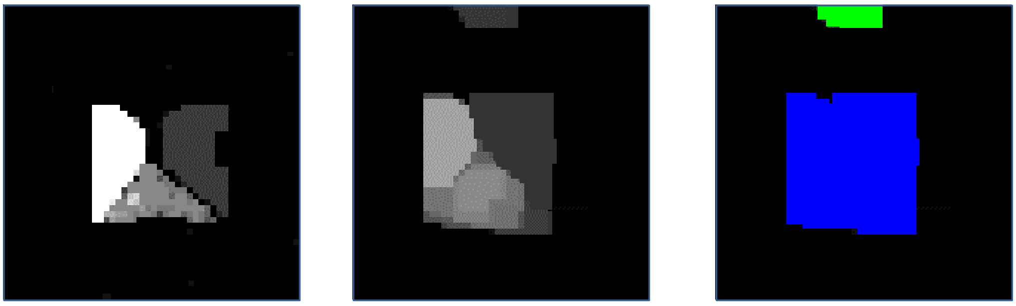

(d) Filtering & Thresholding (e) Roof reconstructuring (f) Classification

Fig.3.3.5. Identifying the Hip shape roof.

The classification method of Random Forest (RF) is introduced in detail in section 3.3.2. The results of applied area of Ishinomaki City, Miyagi prefecture using airborne VHR imageries with proposed method are described in section 4.2 and 4.3.

3.3.2. Random Forest Classification method

i . Introduction

Various ensemble based methods have been proposed for classification and regression in recent years. These methods have been proven called improve classification accuracy considerably. The most widely used ensemble methods are boosting and bagging. Boosting is based on sample re-weighting, but bagging uses bootstrapping. The Random Forest (RF) classifier uses bagging, or bootstrap aggregating, to form an ensemble of classification and regression tree (CART) -like classifiers. The Random Forest classification algorithm creates multiple CART-like trees [12, 13], each trained on a bootstrapped sample of the original training data. In addition, it searches only a random subset of the variables for a split at each CART node, in order to minimize the correlation between the classifiers in the ensemble [14,15].

Beside the areas of application, every Random Forest can be described by the following key parameters:

- Forest size T (number of trees)
- Maximum allowed tree depth D
- Choice of weak learner model
- Corresponding training energy function
- Injected amount of randomness influenced by ρ

ii . Decision tree

A decision tree is a set of questions organized in a hierarchical manner and represented graphically as a tree. For a given input object, a decision tree estimates an unknown property of the object by asking successive questions about its known properties. Which question to ask next depends on the answer of the previous question and this relationship is represented graphically as a path through the tree which the object follows. The decision is then made based on the terminal node on the path. A data point, is denoted by a vector $\mathrm{v} = (x_1, x_2, x_3, ..., x_d) \in F$, where the components x_i represent some attributes of the data point, called *features*. These features may vary from application to application. For instance, in a computer vision application **v** may correspond to a pixel in an image and the $x_i s$ represent the responses of a chosen filter bank at that particular location.

The number of features naturally depends on the type of the data point as well as the application. In theory, the dimensionality of the feature space F , *d*, can be very large. Based on this let us formulate the features of interest that are computed at any single time to be a subset selected from the set of all possible features as $\phi(\mathrm{v}) = (x_{\phi 1}, x_{\phi 2}, x_{\phi 3}, ..., x_{\phi d'}) \in F^{d'} \subset F$, where d' denotes the dimensionality of the subspace and $\phi_i \in [1, d]$ denote the selected dimensions. In most applications, d can be very large, but the dimension of the subspace $F^{d'}$ is much smaller $d' <<$.

iii. Weak learner model

A weak learner is defined to be a classifier which is only slightly correlated with the true classification and usually it can only label examples a little better than random guessing. In contrast, a strong learner is a classifier that is arbitrarily and well-correlated with the true classification and it can eventually provide a very low training error. A weak learner model is often used in ensemble learning models like the Random Forest. The algorithms similar to boosting are used by the weak learners to build a strong classifier out of a bunch of weak classifiers [16a,16b].

The weak learner model in Random Forests with binary decision trees is defined with a binary test function, that returns "*true*" or "*false*" which equals the forwarding of the test data to the "*right*" or "*left*" child. The weak learner function is selected during the conceptional stage before the training starts. In most Random Forests, the decision trees are always binary trees. This leads to a binary test function, because each split node needs a binary decision. In decision trees with *n* children, the split function must return an *n-ary* output. At first, some of the relevant symbols are explained:

The split functions play a crucial role both in training and testing. It formulates the *parameterization of the weak learner model* as $\theta = (\phi, \psi, \tau)$, where ψ defines the geometric primitive used to separate the data, here in this study we used axis-aligned hyperplane. The parameter vector τ captures thresholds for the inequalities used in the binary test ($\tau \in [\min_i \phi(x_i), \max_i \phi(x_i)]$) and the filter function ϕ selects some features of choice out of the entire vector **v**.

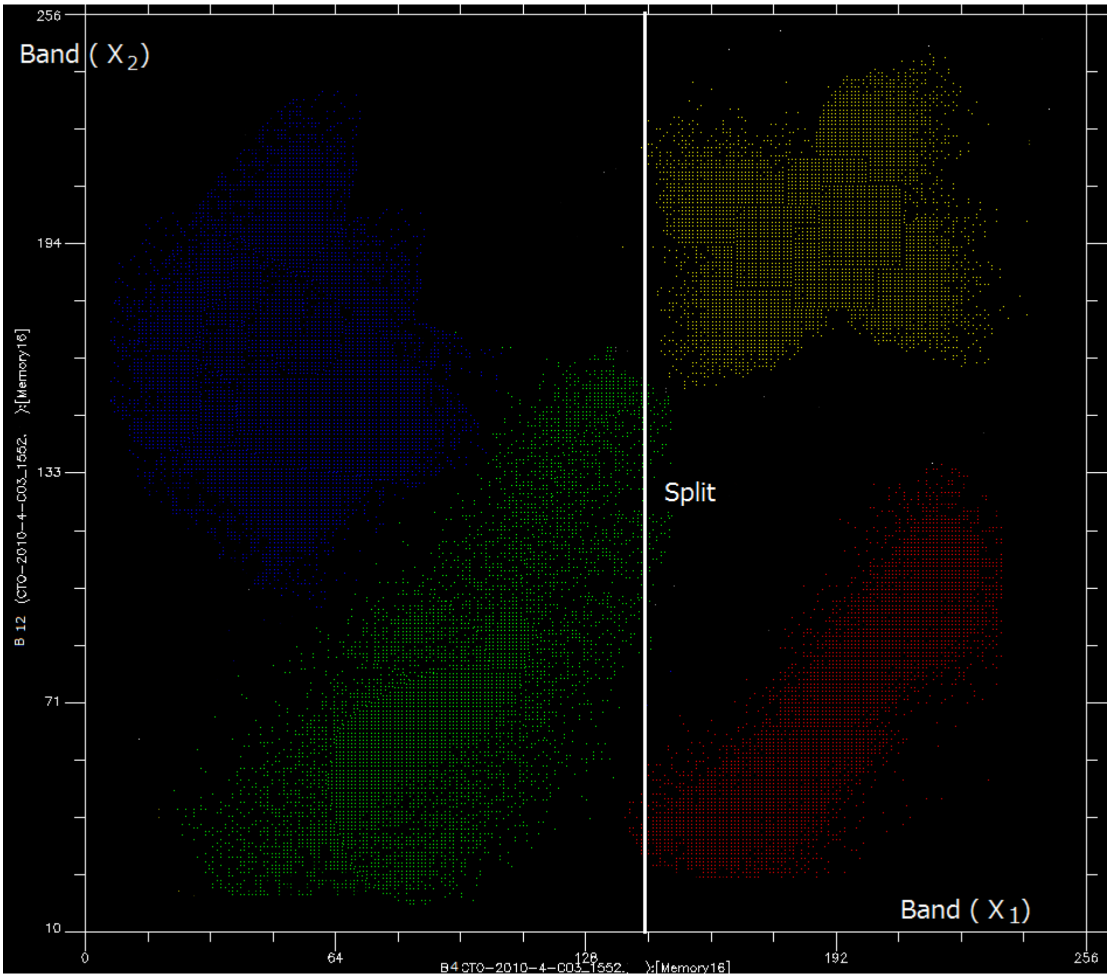

Fig. 3.3.6. Axis-aligned hyperplane is visualized here with 4 lable training data of two DMP in homogeneous coordinates.

Figure 3.3.6 illustrates a possible weak learner model $\mathrm{v} = (x_1;x_2)$, for example. The parameterization of the *linear data separation model* of axis-aligned hyperplane that used in this study is defined as

$$h(\mathrm{v},\theta_j) = [\tau_1 > \phi(\mathrm{v}) \cdot \psi > \tau_2] \qquad (3.3.9)$$

where $[\cdot]$ is the Indicator function of tree training that returns 1 if the argument is true and 0 if it is false (see Appendix). Each node of the tree has associated a different split function. For instance, in the 2D example in Figure 3.3.6 , $\mathrm{v}(x_1 x_2) \in \Re^2$ and $\phi(\mathrm{v}) = (x_1 x_2 1)$ are visualized in homogenious coordinates of axis-aligned hyperplane. Here the θ_j is the *parameterization of the weak learner model at* j *node*. The main important steps of Random forest, tree taining, energy modeling, tree testing and leaf predicting and esembling methos are briefly described below.

ⅳ. Tree training

The split functions stored at the internal nodes are key for the functioning of the tree. These functions could be designed manually [17]. The training phase takes care of selecting the type and parameters of the test function $h(\mathrm{v}, \theta_j)$ associated with each split node by optimizing a chosen objective function defined on an available training set.

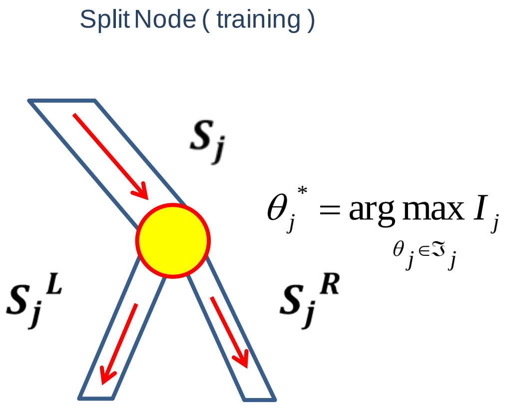

Fig.3.3.7 Split node of Training. Here the parameters of node *j* involve optimizing a chosen objective function is trained.

The optimization of the split functions proceeds in a greedy manner. At each node *j*, depending on the subset of the incoming training set S_j learn the function that "best" splits S_j into S_j^R and S_j^L, This problem is formulated as the maximization of an objective function at that node

$$\theta_j^* = \arg\max_{\theta_j \in \Im} I_j \tag{3.3.10}$$

With

$$I_j = I(S_j, S_j{}^R, S_j{}^L, \theta_j) \tag{3.3.11}$$

$$S_j{}^L = \{(\mathrm{v}, c) \in S_j \mid h(\mathrm{v}, \theta_j) = 0\}$$

$$S_j{}^R = \{(\mathrm{v}, c) \in S_j \mid h(\mathrm{v}, \theta_j) = 1\}$$

As before, the symbols $S_j, S_j{}^R, S_j{}^L$ denote the sets of training points before and after the split (see Figures 3.3.7). The objective function I_j (here the information gain I at j node) is of an abstract form. Its precise definition and the meaning of “best” depend on the task at hand. The term “best” can be defined as splitting the training subset S_j such that the resulting child nodes are as pure as possible, that is, containing only training points of a single class. In this case the objective function can, for instance, be defined as the information gain I (details will be given in the next section).

v. Energy model

The objective function used during training is essential in constructing decision trees that will perform the desired task. In fact, the result of the optimization problem in determining the parameters of the weak learners, which, in turn, determines the path followed by a data and thus its prediction. In summary, through its influence on the choice of weak learners the energy model determines the prediction and estimation behavior of a decision tree.

The tree training phase is driven by the statistics of the training set. The basic building blocks of the training objective function are the concepts of *impurity* and *information gain*. For discrete probability distributions of our study, we tested two impurity measure cost functions of Shannon entropy and Gini index, defined as

$$H(S)_{Shannon} = -\sum_{c \in C} p(c) \log_2 p(c) \tag{3.3.12}$$

$$H(S)_{Gini} = 1 - \sum_{c \in C} p^2(c) \tag{3.3.13}$$

where S is the set of training points and the letter c indicates the class label. The set of all classes is denoted C and $p(c)$ indicates the empirical distribution extracted from the training

points within the set S. The children distributions are more pure, their entropy has decreased and their information content increased. This improvement can be quantified by measuring the information gain. Figure 3.3.8 illustrates a toy classification example. The graph shows a number of training points on a 2D space, where each coordinate denotes a feature value and the colors indicate the known classes. During training our aim is to learn the parameters that best split the training data. In this example our objective is to separate two classes as much as possible. For instance, split the training data in t_1 this produces lowest entropy for class $c \in$red. meaning "best" split to two sets of data (as shown in Table.3.3.1).

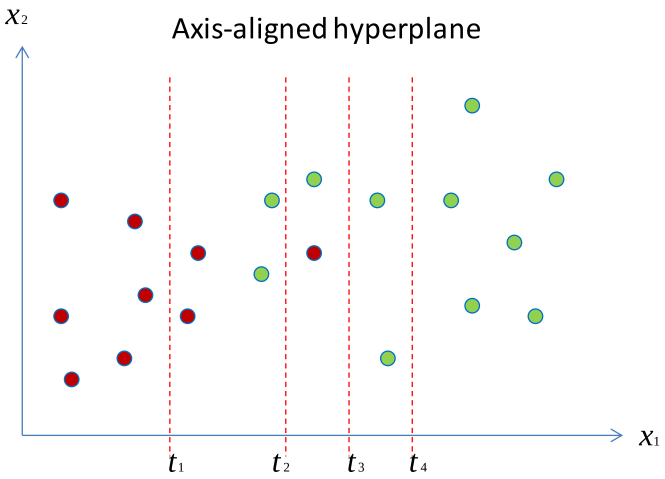

Fig. 3.3.8. Illustrate of a toy classification of 2 classes with 4 splits.

Table. 3.3.1. Shannon Entry for class $c \in$red according to each split

	Distribution	P(*L*)	P(*R*)	E(*L*)	E(*R*)	E
t_1	6R0G|3R11G	1.00	0.21	0.000	0.741	0.741
t_2	8R2G|1R9G	0.80	0.10	0.722	0.467	1.189
t_3	9R3G|0R8G	0.75	0.00	0.811	0.000	0.811
t_4	9R5G|0R6G	0.64	0.00	0.941	0.000	0.941

Thus, if we use the children rather than the parent node, we would have more chances of correct prediction; we have reduced the uncertainty of prediction. The children distributions are more pure, their entropy has decreased and their information content increased. This improvement can be quantified by measuring the information gain.

$$I = H(S) - \sum_{i\in\{L,R\}} \frac{|S^i|}{|S|} H(S^i) \qquad (3.3.14)$$

The splits have produced the information gain $I(t_2,t_3,t_4) < I(t_1)$ shown in Figure 3.3.8. This corresponds to lower child entropies and a higher information gain. Maximizing the information gain helps select the split parameters which produce the highest confidence in the final distributions and this concept is at the basis of RF training.

vi. Tree testing

The formulation of the test function at a split node *j* as a function with binary outputs

$$h(\mathrm{v},\theta_j): F \times \Im \rightarrow \{0,1\} \qquad (3.3.15)$$

where 0 and 1 can be interpreted as “false” and “true” respectively, $\theta_j \in \Im$ denote the parameters of the test function at the j th split node. Here the F and $[\times]$ denote the feature space and the indicator function on tree testing (see Appendix). The data point **v** arriving at the split node is sent to its left or right child node according to the result of the test function. The split functions stored at the internal nodes are key for the functioning of the tree.

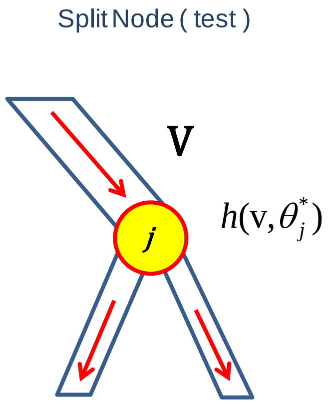

Fig.3.3.9. The split node of the testing. Here the parameters of node *j* involve optimizing a chosen objective function is trained.

The basic principle of tree testing is simple. Given a previously unseen data point v a decision tree hierarchically applies a number of predefined tests (see Figure 3.3.9). Starting at the root, each split node applies its associated test function $h(\mathrm{v},\theta_j)$ to v. Depending on the result of this binary test the data is sent to the right or left child. This process is repeated until the data point reaches a leaf node. The leaf nodes contain a predictor which associates an output class label with the input v.

vii. Leaf prediction

During training, besides the tree structure and the weak learners, we also need to learn how to make predictions. After training, each leaf node remains associated with a subset of (labeled) training data. During testing, a previously unseen point traverses the tree until it reaches a leaf. Since the split nodes act on features, the input test point is likely to end up in a leaf associated with training points which are all similar to itself. Thus, it is reasonable to assume that the associated label must also be similar to that of the training points in that leaf. This justifies using the label statistics gathered in that leaf to predict the label associated with the input test point.
In the most general sense the leaf statistics can be captured using the posterior distributions $P(c \mid \mathrm{v})$, where c represent the discrete labels respectively. v is the data point that is being tested in the tree and the conditioning denotes the fact that the distributions depend on the specific leaf node reached by the test point.

viii. Randomness model

Randomness is injected into the trees during the training phase. The two main ways of doing so are: random training set sampling [14] and randomized node optimization [18]. Here the bagging sample section algorithm is used for random training set sampling. This yield margin-maximization properties for the ensemble models and enables train trees on the entire training data are used to randomized node optimization. When training at the j^{th} node only makes available a small random subset $\Im_j \in \Im$ of parameter values from the entire parameter space. Thus, under the randomness model training a tree is achieved by optimizing each split node j by

$$\theta_j^* = \arg\max_{\theta_j \in \Im_j} I_j \tag{3.3.16}$$

ix. Ensemble of trees

A random decision forest is an ensemble of randomly trained decision trees. The key aspect of the forest model is the fact that its component trees are all randomly different from one another. This leads to decorrelation between the individual tree predictions and, in turn, results in improved generalization and robustness. The forest model is characterized by the same components as the decision trees. The family of split function, energy model, the leaf predictors and the type of randomness influence the prediction/estimation properties of the forests.

In a forest with T trees we use the variable $t \in \{1, \ldots, T\}$ to index each component tree. All trees are trained independently (and possibly in parallel). During testing, each test point v is simultaneously pushed through all trees (starting at the root) until it reaches the corresponding leaves. Combining all three predictions into a single forest prediction may be done by a simple averaging operation [14]. For instance, in classification

$$p(c \mid \mathrm{v}) = \frac{1}{T} \sum_{t=1}^{T} p_t(c \mid \mathrm{v}) \tag{3.3.17}$$

where $p_t(c \mid \mathrm{v})$ denotes the posterior distribution obtained by the t th tree.

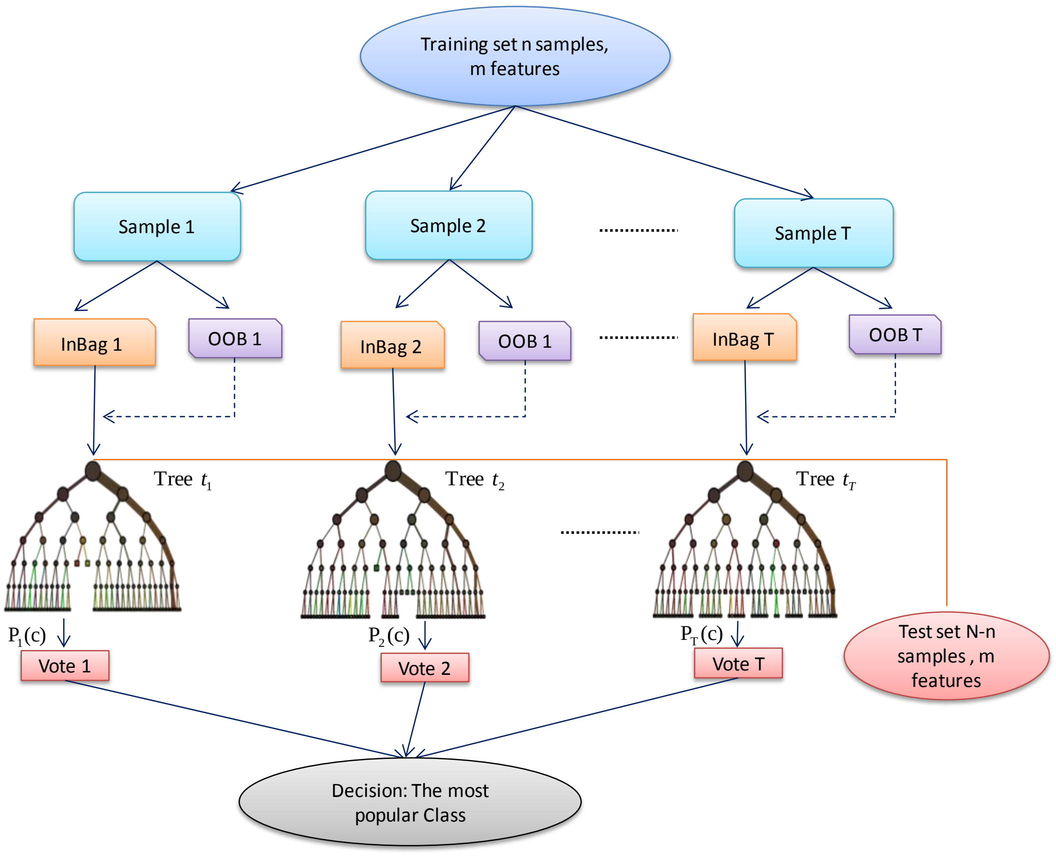

Fig.3.3.10. The probabilistic distribution of Random Forests $t_1..t_T$ and each of its average probability distributions of the categories $P_1(c)......P_T(c)$.

Each tree gives a unit vote for the most popular class at each input instance. The output of the classifier is determined by a majority vote of all the trees. The RF classifier has three parameters: the number of trees *T*, the depth of the tree *D* and the number of variables θ randomly chosen at each split. The Random Forest's error rate depends on two parameters: the correlation between any pair of trees and the strength of each individual tree in the forest. Increasing the correlation increases the forest error rate while increasing the strength of the individual trees decreases this misclassification rate. Reducing θ reduces both the correlation and the strength. As a result, the algorithm can handle high dimensional data and use a large number of trees in the ensemble. Here review of Random Forest (RF) illustrated in Figure. 3.3.10 , RF is an ensemble of *T* number of decision trees. When the training set for a particular tree is drawn by sampling with replacement, about one-third of the cases are left out of the sample set. These samples are called Out-Of-Bag (OOB) data (see Figure. 3.3.10) and are used to estimate the feature importance as detailed hereby. To estimate the test set error, the out-of-bag samples for each t tree are run down through the tree. Averaging the error produced by this, over the entire ensemble, yields an unbiased estimate of the test set error. This is actually an upper estimate [14], as each sample can only be tested on the trees for which it was OOB. In the following, we denote $\mathcal{B}^{(t)}$ by the In-Bag samples for a tree *t* and $\mathcal{B}^{c(t)}$ by the complementary samples, i.e., the OOB data for the tree t.

X. Feature importance measure (Variable importance)

As well as classification, Random Forests provide a measure of feature importance that is processed on OOB data and is based on the permutation importance measure [12]. The importance of a feature ϕ can be estimated by randomly permuting all the values of this feature in the OOB samples for each tree. This follows the idea that a random permutation of a feature mimics the absence of that feature from the model. The measure of feature importance is the difference between prediction accuracy (i.e., the number of observations correctly classified) before and after permuting feature ϕ , averaged over all the trees [12]. Decrease of high prediction accuracy denotes the importance of that feature. Suppose that the training samples consist of pairs of the form (x_i, l_j) where x_i is an instance, and l_j its true label. The importance of a feature ϕ per tree t is computed as follows:

$$\aleph^{(t)}(\phi) = \frac{\sum_{x_i \in \mathcal{B}^{c(t)}} \wp(l_j = c_i^{(t)})}{\left|\mathcal{B}^{c(t)}\right|} - \frac{\sum_{x_i \in \mathcal{B}^{c(t)}} \wp(l_j = c_{i,\pi_\phi}^{(t)})}{\left|\mathcal{B}^{c(t)}\right|} \qquad (3.3.18)$$

where $\mathcal{B}^{c(t)}$ corresponds to OOB samples for a tree t, with $t \in \{1,....,T\}$ and $\wp$ is the indicator function. $c_i^{(t)}$ and $c_{i,\pi_f}^{(t)}$ are the predicted classes for sample x_i before and after permuting the feature ϕ respectively. Note that $\aleph^{(t)}(\phi) = 0$, if feature ϕ is not in the tree t. The importance score for a feature ϕ is then computed as the mean importance over all the trees:

$$\aleph(\phi) = \frac{\sum_{T} \aleph^{(t)}(\phi)}{T} \qquad (3.3.19)$$

where T is the number of trees.

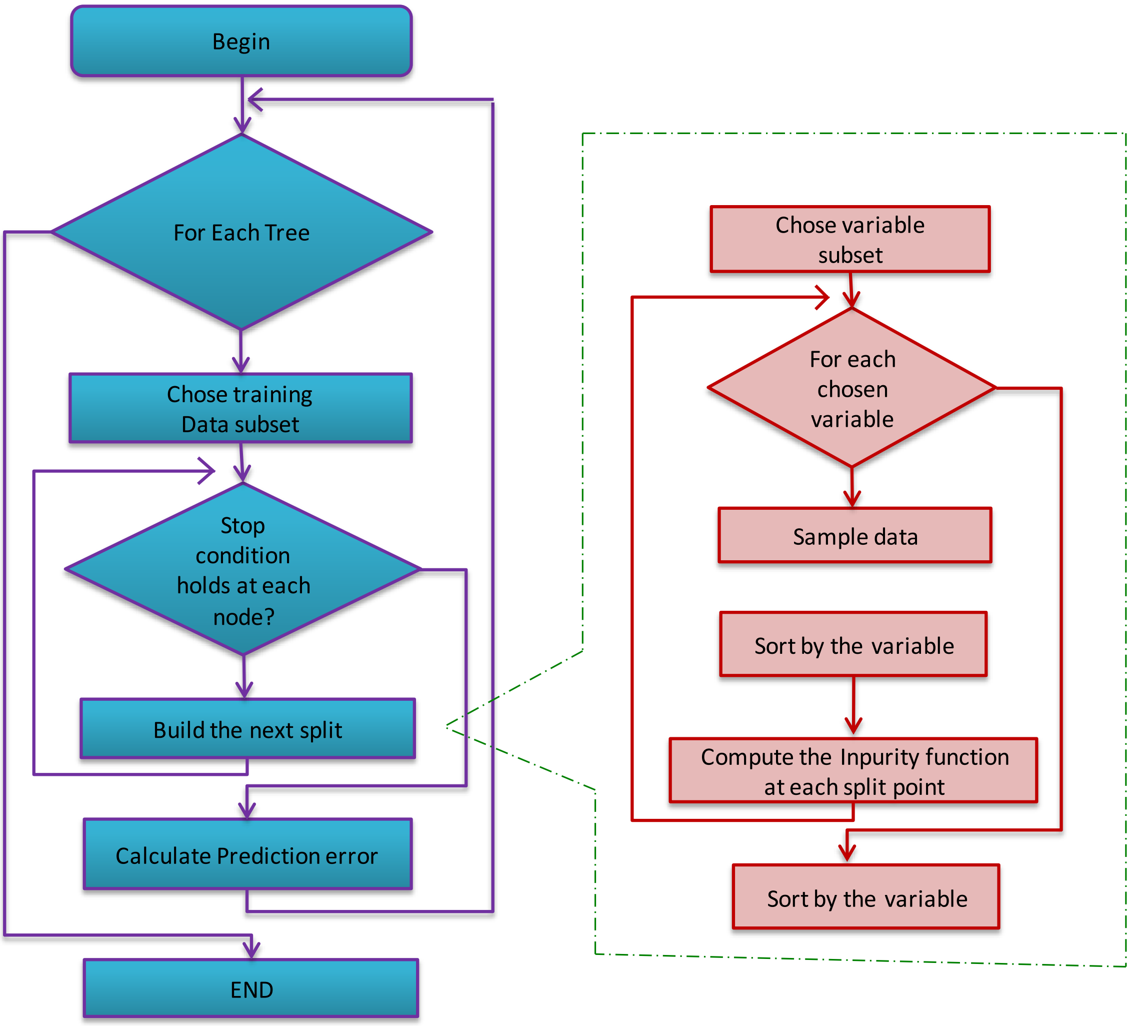

Fig.3.3.11. Flow chart of the Random Forest program.

Here Figure.3.3.11, the flow chart of the RF build up process is illustrated. The DMP segmented vectors (described in section 3.2) are applied to the RF implementation with the supporting QGIS open source software combined with the CRAN software package of R for ROI selection. RF software by Leo Breiman and A. Culter is distributed freely on the internet, both as a standalone FORTRAN program and as a package for the R statistics language (http://www.r-project.org). The reference image of three types of building in (small=red, medium=green, large= blue) and background (black) in Figure.3.3.12 (a), while (b) shows the generated Building Roof Reconstructed (BRR) with 20 channel image (described in section 3.3.1) that RF classification is applied.

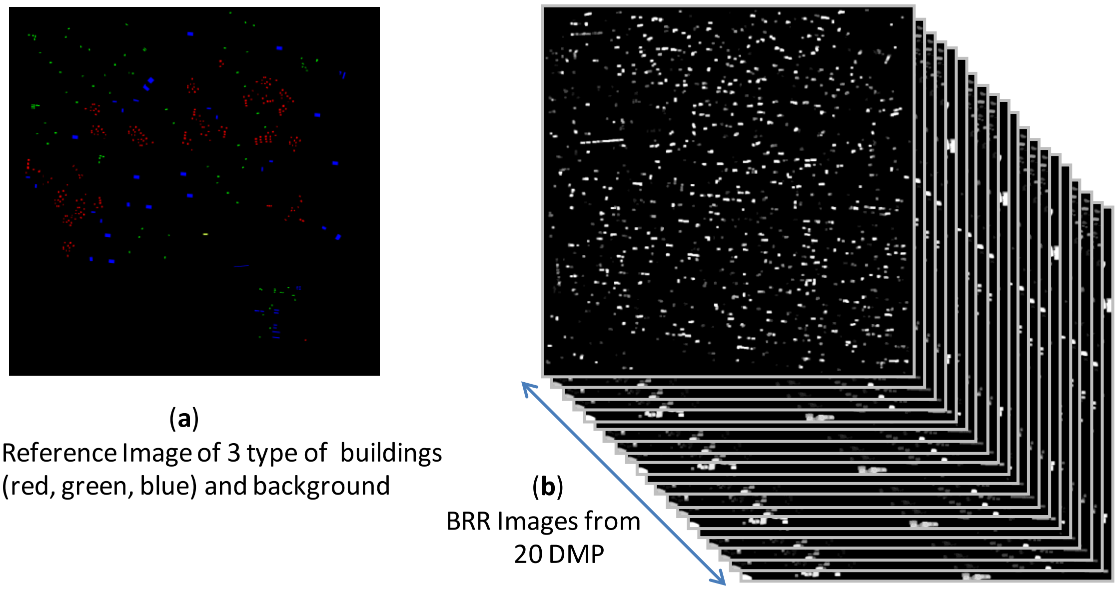

(**a**)
Reference Image of 3 type of buildings
(red, green, blue) and background

(**b**)
BRR Images from
20 DMP

Fig.3.3.12. (a) The reference image of 3 types of building (red, green, blue) and background (black), (b) generated 20 channels BRR image that classification is applied.

3.4. Building damage detection using Fast Fourier Transform.

In this section, we focused on an automatic damaged building detection methodology based on Fast Fourier Transform, which is helpful to recognize, rescue, recovery and disaster management tasks in an event of natural hazard such as earthquake and tsunami. The method proposed here is intended for image registration and damaged building detection under the following steps. First, we tested Reddy's [19] methodology to attempt to automatically register the pre and post event optical images in hazardous area. Then each pre and post event images are divided to sub imageries (64m x 64m) and are applied to two dimensions (2D) Discrete Fast Fourier Transform (DFT) process, which calculate different distributions of max-scaled log power spectrum with the vertical frequency to identify damaged building due to the natural hazard using the proposed method. The areas of damaged and undamaged building were identified by using their different spectral effectiveness value over 2D FFT. The airborne Very High Resolution (VHR) imageries consisting of pre and post 2011 Pacific coast Tohoku earthquake and tsunami site of the Ishinomaki area in Miyagi Prefecture, Japan were used for this study.

3.4.1. Fast Fourier Transform for image processing.

The 2D FFT images were constructed using Fast Fourier Transform (FFT), the fast algorithm for computing the Discrete Fourier Transform (DFT). The DFT has been widely used in signal and image processing [19]. An image with a two-dimensional function, *f(x)* which might be a row or column of pixel, can be represented by a Fourier series composed associated coefficients combination of sine and cosine terms. The DFT is effective to characteristic of spatial information [20, 21], e.g. homogeneous structures such as buildings, roofs and roads.

Let the image be a real-valued continuous function $f(x_1,x_2)$ defines an integer-valued Cartesian grid 0<= x1<=N1, 0<= x2<=N2, the DFT is defined as follows:

$$F(k_1,k_2)=\sum_{n_1=0}^{N_1-1}\sum_{n_2=0}^{N_2-1} f(x_1x_2)e^{-j2\pi x_1k_1/N_1-j2\pi x_2k_2/N_2} \qquad (3.4.1)$$

Where

x_1: Number of pixels horizontally
x_2 : Number of pixels vertically
k_1,k_2: Spatial frequency variables
j : Imaginary component of complex number

Once DFT is applied, the spatial domain is converted to the frequency domain, can be edited to identify specific features, reduce noise, and add or remove periodic features. Thresholding the high frequency coefficients correspond to reducing the noise effects, while the low frequency coefficients provide a trigonometric interpolation via a finite linear combination of sine and cosine of the various frequencies of interest [19]. The DFT frequency domain image can be transformed back into the spatial domain using Inverse Fast Fourier Transform (IFFT), which is defined a follows:

$$f(x_1,x_2)=\frac{1}{N_1N_2}\sum_{k_1=0}^{N_1-1}\sum_{k_2=0}^{N_2-1} f(k_1k_2)e^{j2\pi k_1x_1/N_1+j2\pi k_2x_2/N_2} \qquad (3.4.2)$$

$$0\le x_1\le N_1-1, 0\le x_2\le N_2-1$$

Figure.3.4.1. shows the pre and post event un- registered VHR airborne imagery in the same area.

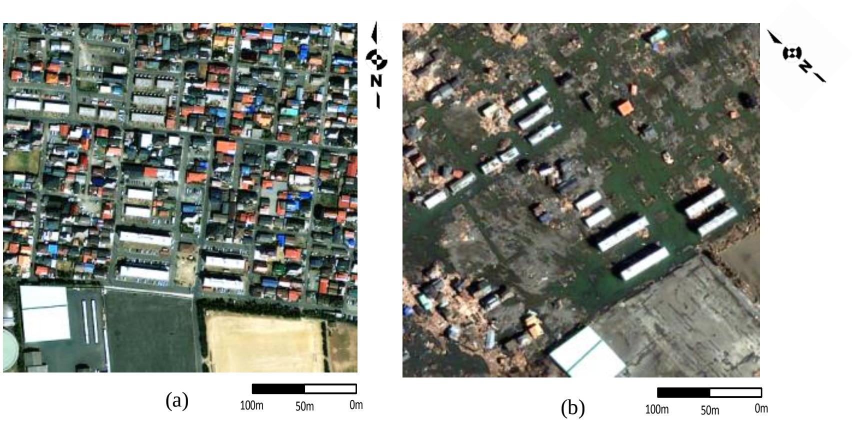

(a) (b)

Fig.3.4.1. Before the Tsunami Hazard Ishinomaki area (a) and after the tsunami hazard (b).

3.4.2. Image Registration Methodology

This method relies on the translation property of the Fourier transform, which is referred to as the Fourier Let $f_1(x,y)$ and $f_2(x,y)$ are the two images of I_1 and I_2 that differ only by displacement (x_0, y_0) i.e.,

$$f_2(x,y) = f_1(x - x_0, y - y_0) \qquad (3.4.3)$$

Their corresponding Fourier transforms F_1 and F_2 will be related by

$$F_2(\xi,\eta) = e^{-j2\pi(\xi x_0 + \eta y_0)} \times F_1(\xi,\eta) \qquad (3.4.4)$$

The cross-power spectrum R (ratio) of two images $f_1(x,y)$ and $f_2(x,y)$ with Fourier transforms F and Fi is defined as

$$R = e^{j2\pi(\xi x0 + \eta y0)} = \frac{F_1(\xi,\eta) \times Conj(F_2(\xi,\eta))}{Abs(F_1(\xi,\eta)) \times Abs(F_2(\xi,\eta))} \qquad (3.4.5)$$

Where ***Conj*** is the complex conjugate and ***Abs*** is the absolute value, the shift theorem guarantees that the phase of the cross-power spectrum is equivalent to the phase difference between the images. By taking the inverse Fourier transform of the representation in the frequency domain, we will have a function that is an impulse; that is, it is approximately zero everywhere except at the displacement that is needed to optimally register the two images.

If $f_2(x,y)$ is a shifted, rotated and scaled replica of $f_1(x,y)$ with shift (x_0, y_0), rotation (θ_0) and scaled factors of (a, b) for the horizontal and vertical directions , then

$$F_2(\xi,\eta) = \frac{1}{|ab|} F_1(\xi / a, \eta / b) \qquad (3.4.5)$$

By converting the axes to logarithmic scale[22], ignoring the multiplication factor $1/ab$, scaling can be reduced to a translational movement,

$$F_2(\log\xi, \log\eta) = \frac{1}{|ab|} F_1(\log\xi - \log a, \log\eta - \log b) \tag{3.4.6}$$

$$F_2(x, y) = F_1(x - c, y - d) \tag{3.4.7}$$

where $x = \log\xi, y = \log\eta, c = \log a$ *and* $d = \log b$.

The shift (c,d) can be found by the phase correlation technique and the scaling (a,b) can be computed from the shift (c,d) as

$$\begin{aligned} a &= e^c \\ b &= e^d \end{aligned} \tag{3.4.8}$$

Where e is the natural algorithm base. If (x,y) is scaled to (x/a, y/a), Their polar representation will be

$$\rho_1 = (x^2 + y^2)^{1/2} \tag{3.4.9}$$

$$\theta_1 = \tan^{-1}(y / x) \tag{3.4.10}$$

$$\rho_2 = ((x / a)^2 + (y / a)^2)^{1/2} = (1 / a)(x^2 + y^2)^{1/2} = \rho_1 / a \tag{3.4.11}$$

$$\theta_2 = \tan^1((x / a) /(y / a)) = \tan^1(x / y) = \theta_1 \tag{3.4.12}$$

If f_1 is shifted, rotated and scaled replica of f_2 their Fourier Magnitude spectra in polar representation are related by

$$M_1(\rho, \theta) = M_2(\rho / a, \theta - \theta_0) \tag{3.4.13}$$

$$M_1(\log\rho, \theta) = M_2(\log\rho - \log a,\ \theta - \theta_0) \tag{3.4.14}$$

$$M_1(\xi, \theta) = M_2(\xi - d,\ \theta - \theta_0) \tag{3.4.15}$$

Where

$$\begin{aligned} \xi &= \log\rho \\ d &= \log a \end{aligned} \tag{3.4.16}$$

Using the eq.(3.4.15) and (3.4.16) and the phase correlation technique,scale a and angle θ_0 can be found out. Once the scale and angle information are obtained, the image with the highest resolution is scaled and rotation by amounts a and θ_0 , respectively, and the amount of translational movement is found out using phase correlation technique.

3.4.3. Implementation

Here in Figure.3.4.2.shows the flow chart of the computational implement of the image registration method. First the two images of pre (I_1) and post(I_2) event airborne images applied to FFT and calculate the absolute values of $F_1(\xi, \eta)$ and $F_2(\xi, \eta)$. Then a high pass filter was applied to the absolute values to remove low frequency noise and transform the resulting values from rectangular coordinates to log-polar coordinates.

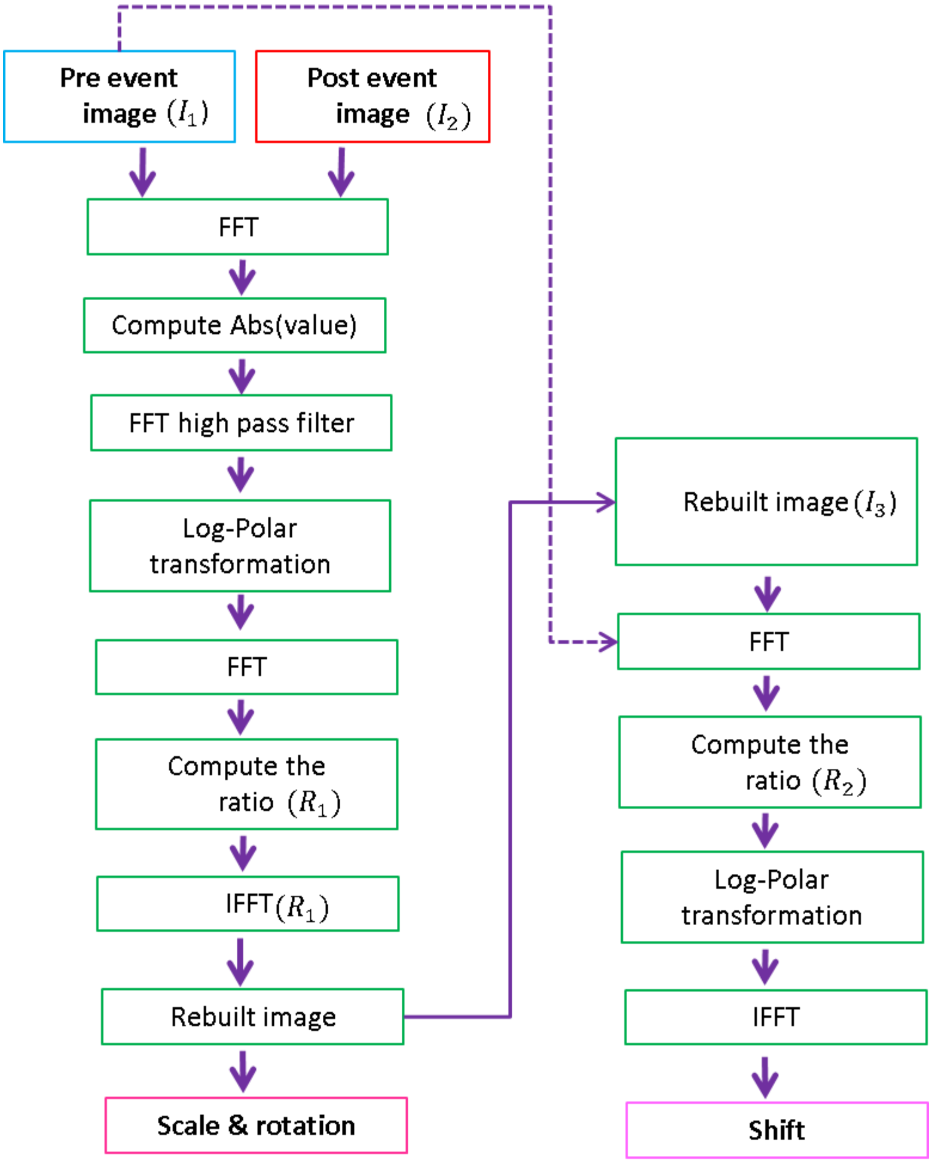

Fig.3.4.2. Flow chart of the pre event and post event image registration.

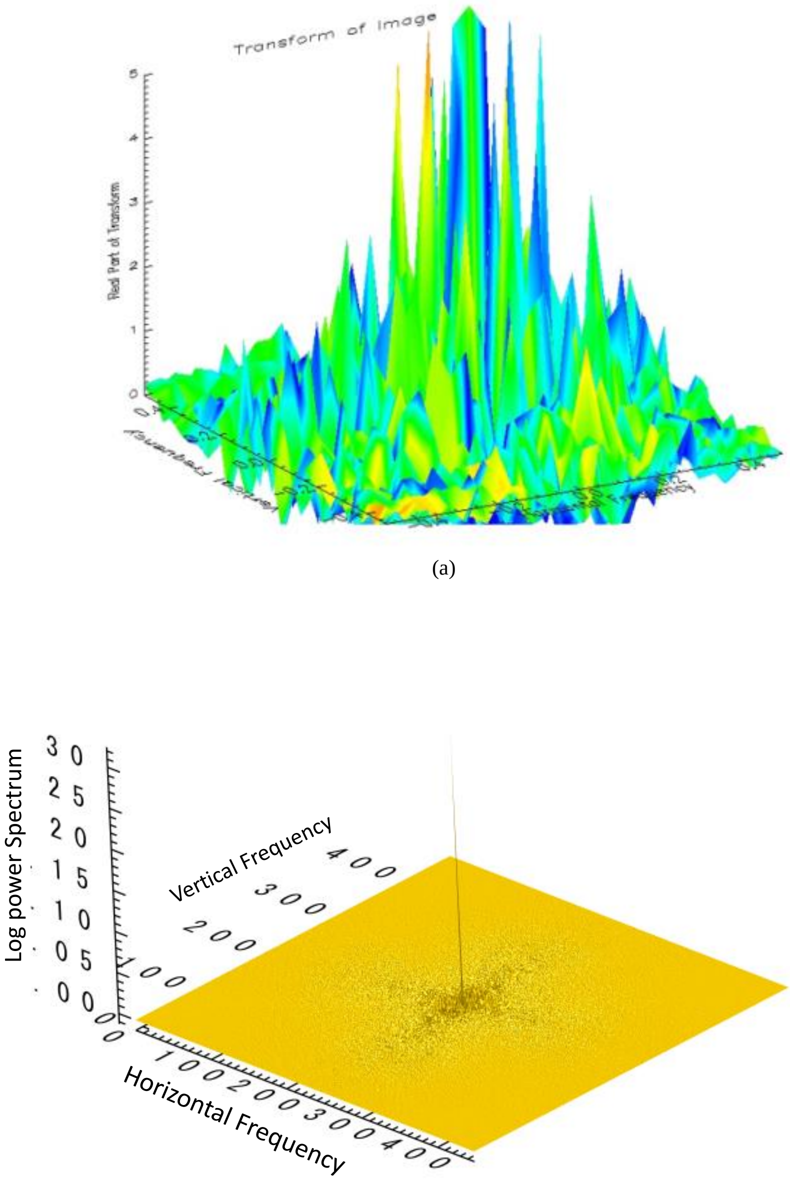

(a)

(b)

Fig.3.4.3. FFT log of image before (a) and after (b) high pass filtering.

In the next step the log-polar coordinates were applied to the FFT and compute the ratio R_1 using equation (3.4.17). Here R_1 is the ratio of $F_1(\xi, \eta)$ and $F_2(\xi, \eta)$. The "ratio" of two images I_1 and I_2 is defined as:

$$R_1 = \frac{F_1(\xi,\eta) * conj(F_2(\xi,\eta))}{abs(F_1(\xi,\eta)) * abs(F_2(\xi,\eta))} \tag{3.4.17}$$

Where ***conj*** is the complex conjugate and ***abs*** is the absolute value. Then compute the inverse FFT IR_1 of the ratio R_1 and Find the location $(\log(a), \theta_0)$ of the maximum of ***abs***(IR_1) and obtain the values of scale ($a = base^{\log(a)}$), and rotation angle (θ_0). Figure.3.4.3 shows the FFT log of image before (a) and after (b) the high pass filtering.

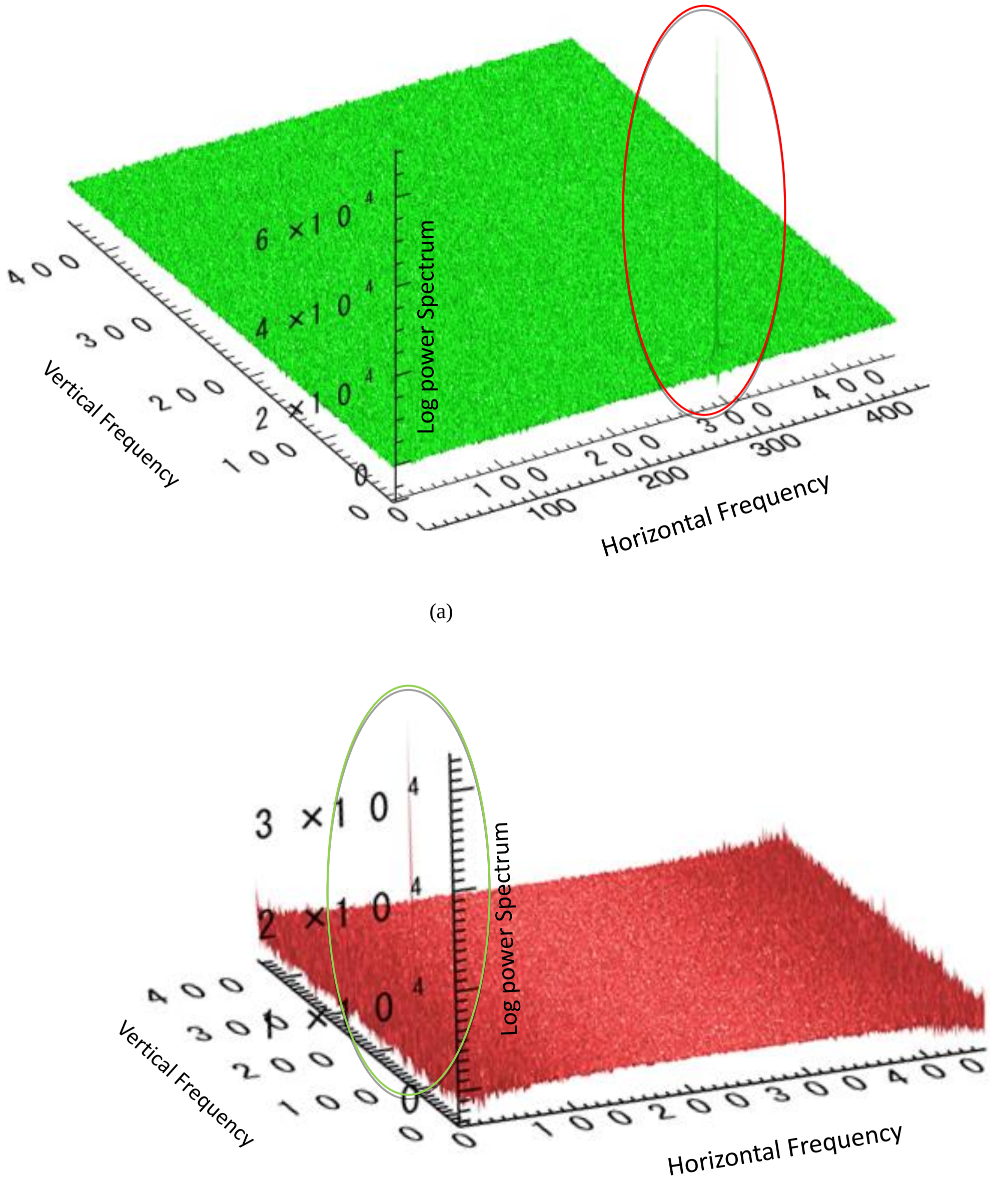

(a)

(b)

Fig.3.4.4. (a) The location $(\log(a), \theta_0)$ of the maximum of *abs(IR_1)* that corresponding to obtain (a) for scale and (θ_0) for rotation angle on cross power spectrum. (b) The location of the maximum *abs*(IR_2) that corresponding to obtain (x_0, y_0) for shift on cross power spectrum.

To find the shift, apply the FFT to the pre event image and post registered (scale and rotation) image I_3 again and compute the ratio R_2 using similarly equation (3.4.5).

$$R_2 = \frac{F_1(\xi,\eta) * conj(F_3(\xi,\eta))}{abs(F_1(\xi,\eta)) * abs(F_3(\xi,\eta))} \tag{3.4.18}$$

Here R_2 is the ratio of two images I_1 and rotated and rescaled image I_3. F_3 is corresponding Fourier transforms of I_3. Then by taking the inverse FFT IR_2 of R_2 and obtain the values (x_0, y_0) of the shift from the location of the maximum of $abs(IR_2)$. The result of this process is the values of the scale, rotation and shift parameters needed to register the two images. Figure.3.4.4 shows the location $(\log(a), \theta_0)$ of the maximum of $abs(IR_1)$ that corresponding to obtain (a) for scale and (θ_0) for rotation angle on cross power spectrum in (a) and (b) shows the location of the maximum $abs(IR_2)$ that corresponding to obtain (x_0, y_0) for shift on cross power spectrum.

3.4.4. Damage area identification

The 2D DFT surface consists of a range of spatial frequencies. The high frequency and shortwave length components are referred to as roughness, the medium frequencies as waviness. The frequency characteristic of these 2D DFT surfaces generated by pre and post event images are changed due to hazard effect. The damage building blocks are identified by analyzing these surface characteristic profiles. Figure 3.4.5 shows the flow chart of damage building block identification process.

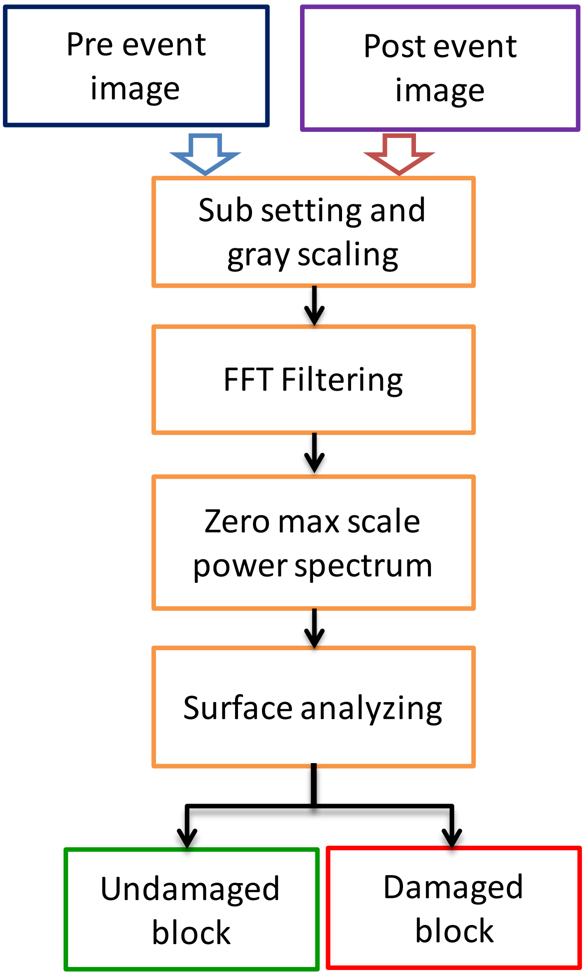

Fig.3.4.5. Flow chart of the damage area identification process.

In the first step the pre and post event images are divided into subsets of 64m×64m scale images. Then the subset images are gray scaled, applied to the FFT and filter using circular cut (high pass) filter. (Threshold the image value is set to -5.25, which is just below the peak of the transform for remove the noises). In the next step the maximum power spectrum value is shifted to 0 for further investigation of the FFT real part surface (see Figure.3.4.6). Here the log FFT power spectrum of the image scaled to a zero maximum. Zero Maximum scaled Power Spectrum (ZMPS) is considered as surface and amplitude parameters characterized based on the vertical deviations of the roughness profile. They are analyzed as shown bellow.

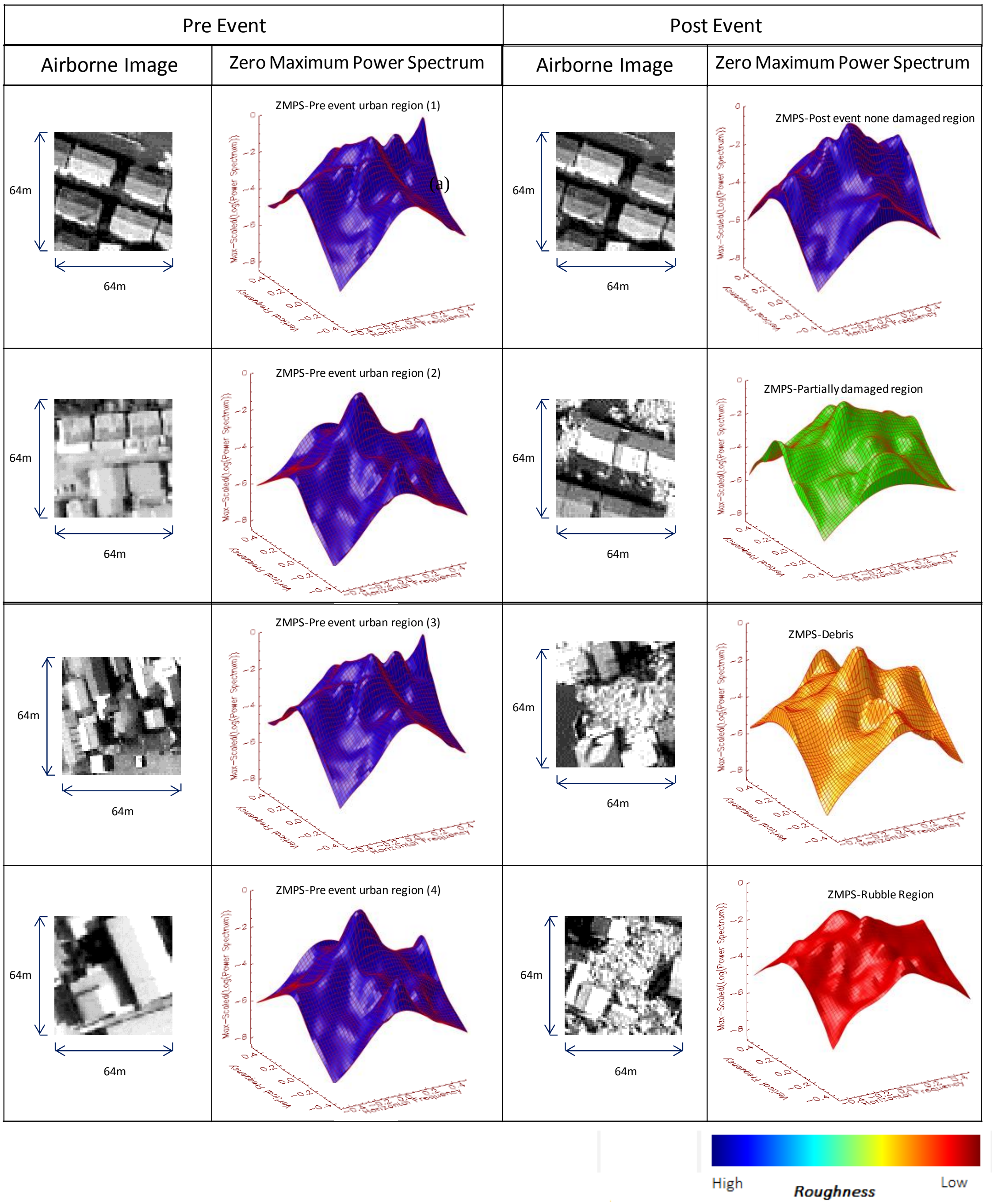

Fig.3.4.6. Pre event and post event ZMPS surfaces in same place. The amplitude parameters characterize are changed if the building of urban area damaged. (*Cont.*)

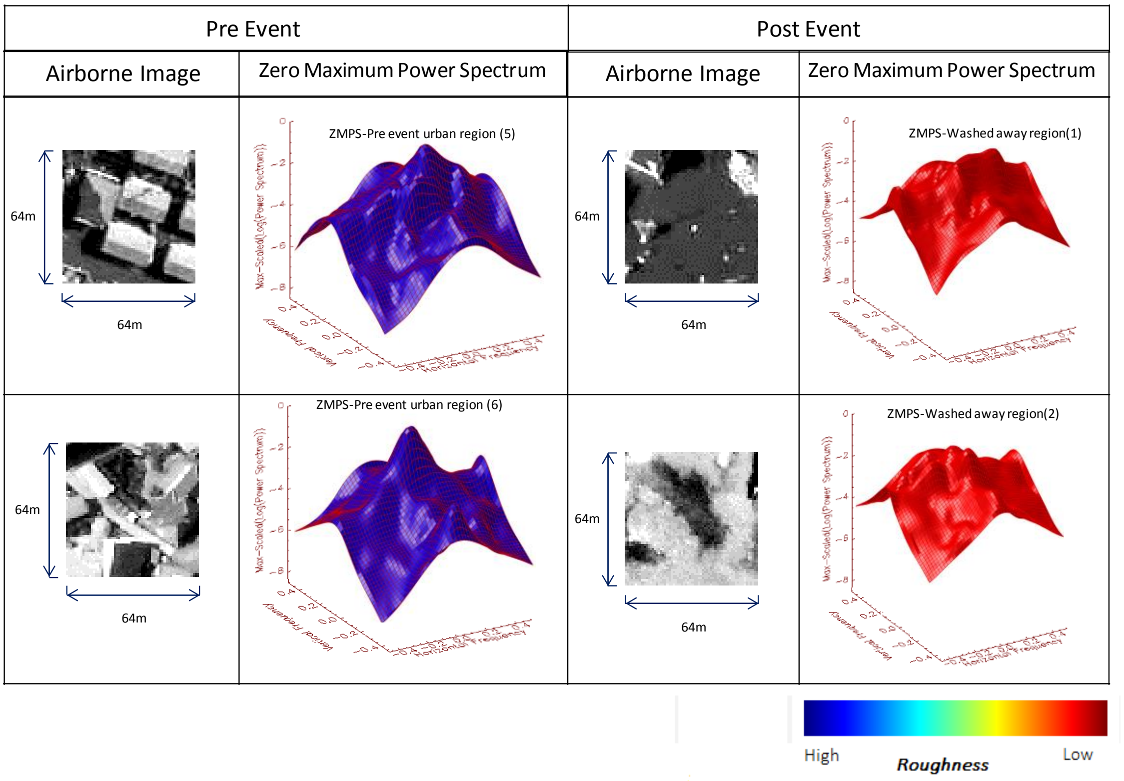

Fig.3.4.6. Pre event and post event ZMPS surfaces in same place. The amplitude parameter characterizes are changed if the building of urban area damaged.

Amplitude parameters characterize the surface based on the vertical deviations of the roughness profile from the mean line. Total profile depth P_t is the sum of the largest profile peak height and the largest profile valley depth of the primary profile within the evaluation reference length. R_a is the arithmetic average of the absolute values and R_q is the root mean squared among the profile roughness parameters.

$$R_a = \frac{1}{n}\sum_{i=0}^{n}|y_i| \tag{3.4.6}$$

$$R_q = \sqrt{\frac{1}{n}\sum_{i=1}^{n}{y_i}^2} \tag{3.4.7}$$

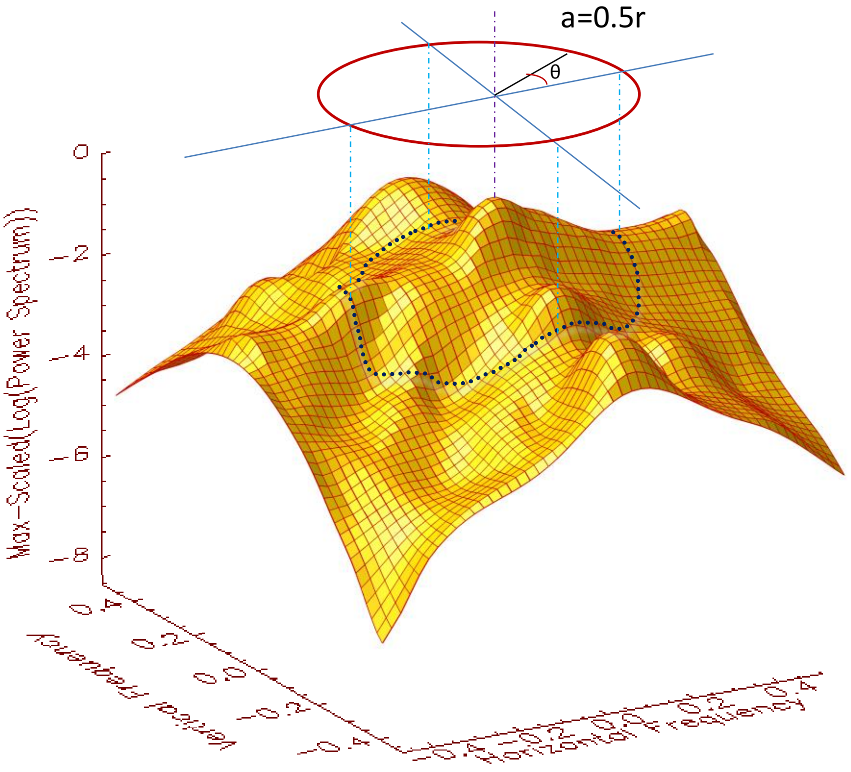

Fig.3.4.7. The cutoff cross section of the log power spectrum surface of 0.5r radius from the peak center.

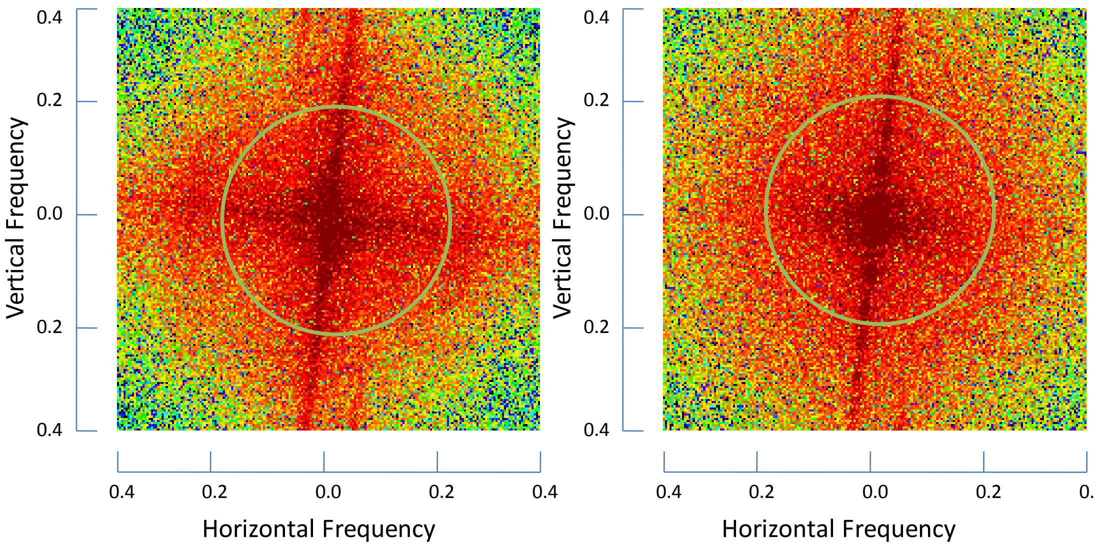

(a) (b)

Fig.3.4.8. Pre (a) and post (b) event 2D log power spectrum surfaces

Here the roughness profile contains nth order, equally spaced points along the trace, and y_i is the vertical distance from the mean line to the i^{th} data point. Height is assumed to be positive in the up direction, away from the bulk material. R_z is the average distance between the highest peak and lowest valley in each sampling length, ASME Y14.36M - 1996 Surface Texture Symbols[23].

The mean roughness depth R_z given as

$$R_z = \frac{1}{s}\sum_{i=1}^{s} R_{ti} \tag{3.4.8}$$

where s is the number of sampling lengths and R_{ti} is the maximum height of the profile R_t for the i^{th} sampling length. The Waviness profile is the mean line generated from the primary profile by the robust Gaussian filter. This filter tolerates the outliers, the definition for which can be found in ISO/TR 16610-10[24]. The Waviness height W_t (total height of W-profile) is the sum of the largest profile peak height and the largest profile valley depth of the W-profile within the evaluation reference length, DIN EN ISO 4287, ASME B46.1. 1999 Surface Texture Parameters [25].

Figure.3.4.7. shows the log FFT of pre event image, log of post event image, cross cutting value of power spectrum around blue circle of the 0.5r distance from the center of the surface. The cross cutting value of power spectrum around 0.5 radius circle in pre event (a) and post event (b) in 2D surfaces are visualized in Figure.3.4.8.

Figure.3.4.9. shows the Roughness profile of pre event and post event images FFT surfaces. The blue line shows primary profile and the red line shows the moving average profile of 20 samples. Figure.3.4.10. shows the 0 mean shifted filtered FFT surface using Gaussian filter. The R_q of cross section frequency value has changed from 0.7312 to 0.6433 μm and Waviness height W_t changed from 0.95 to 0.318 μm after the event. (180 sample areas were tested conducted to identify the damaged and non-damaged area). If the difference of the two values of root mean squared [R_q] is more than 0.0214 and the difference of the two values of Waviness height [W_t]is more than 0.52 , the block is identified as a damaged position.

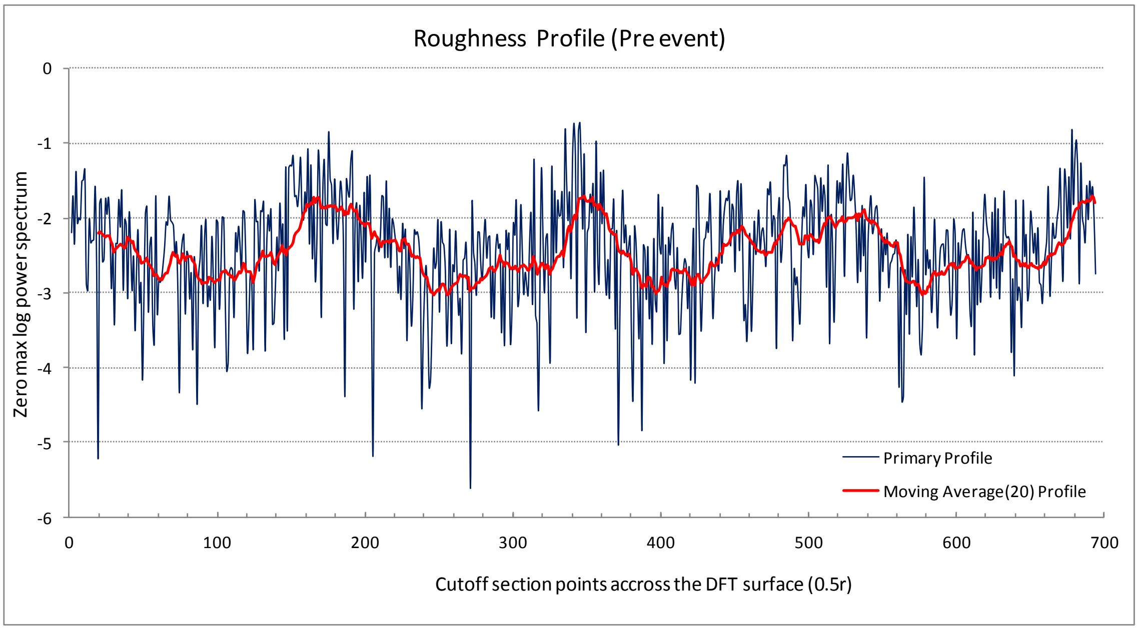

(a) Cross section of pre event 2D FFT surface, (radius=0.5 r)

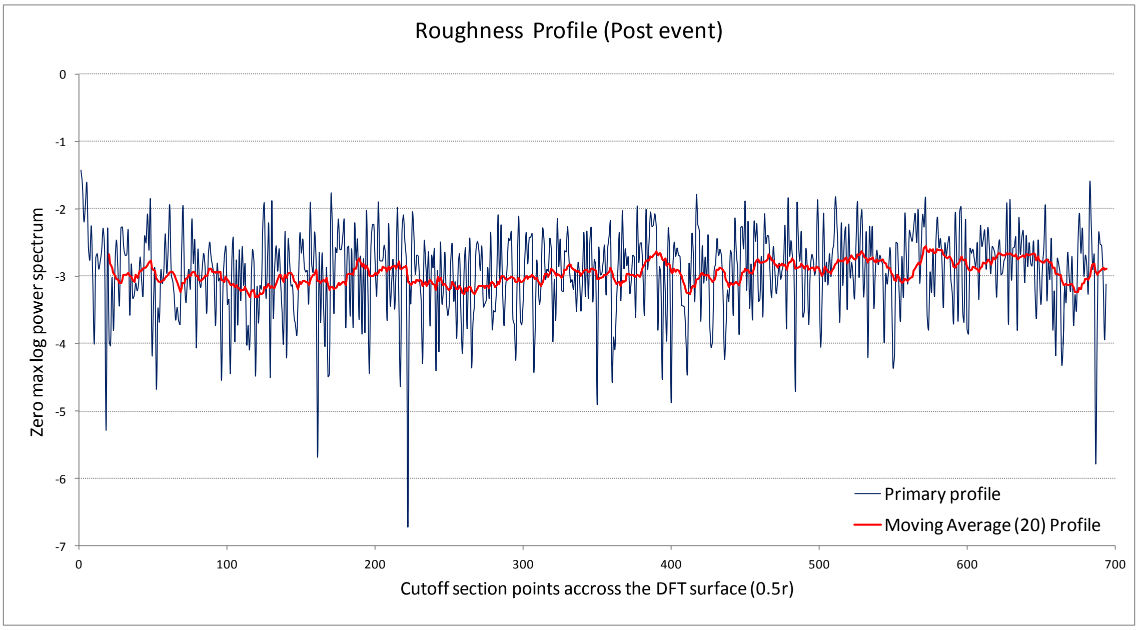

(b) Cross section of post event 2D FFT surface, (radius=0.5 r)

Fig.3.4.9. Roughness profile of pre event (a) and post event (b) images FFT surfaces. (blue line- primary profile, red line- moving average(20) profile)

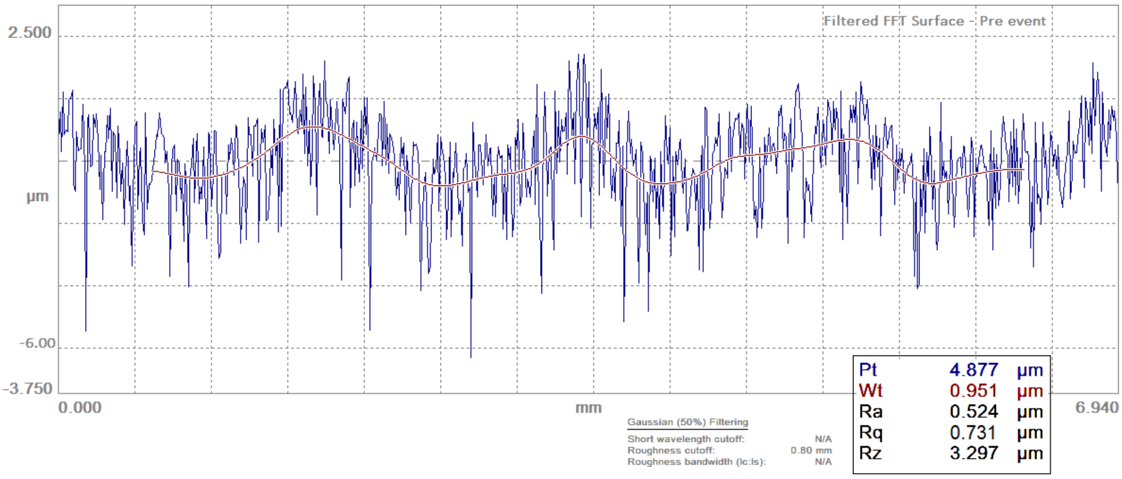

(a) Pre event Filtered FFT surface, (0 mean shifted)

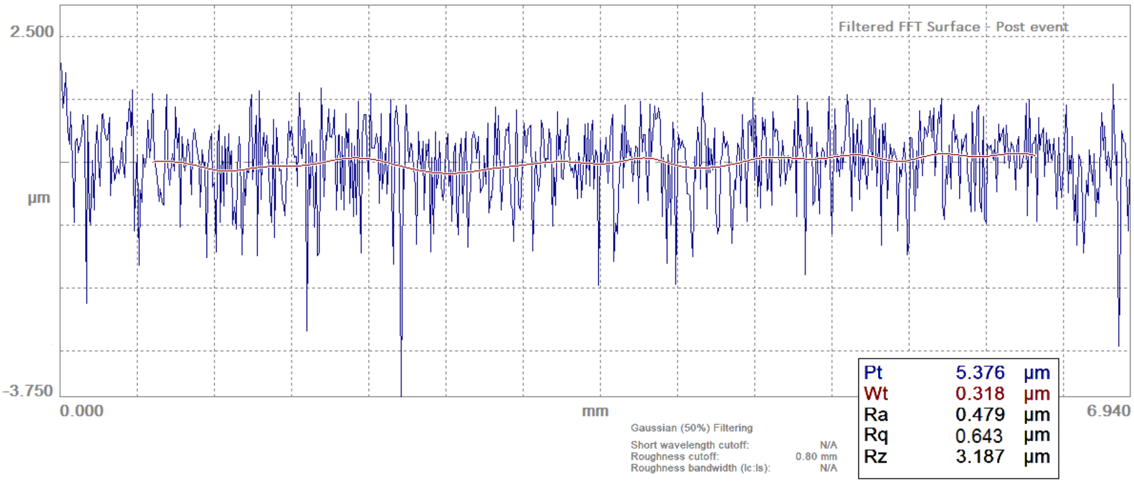

(b) Post event Filtered FFT surface, (0 mean shifted)

Fig.3.4.10. Filtered FFT surface of pre event (a) and post event (b). (0 mean shifted).

The results of the image registration of pre and post event aerial images and damage building extraction using FFT based method will be described at section 4.4.1 and 4.4.2 (Chapter 4) respectively.

3.5. Conclusions

The discussion of this chapter includes the methodologies that used for building extraction in hazardous areas using pre and post event optical images. At the beginning, we overviewed the Morphological profile (MP) and Differential Morphological Profile (DMP). Then the novel MM based method has been extended to pattern recognition conbining morphological filters and Hit-Or-Miss Transform. Furthermore, another novel building roof recognition method and a classification were proposed for building roof identification avoiding image processing difficulties in hazardous areas. Random Forest (RF) classification method that significantly increased the accuracies of the results was overviewed (explained in Chapter.4). As the proposed dual supported building damaged extraction method, the FFT based method has been evolved with a automated image registration method.

References

[1]Destival, I., 1986, “Mathematical morphology applied to remote sensing,” Acta Astronautica, vol. 13, no. 6/7, pp. 371–385.

[2] Vincent, L.,1993,” Morphological grayscale reconstruction in Image analysis: applications and effcient algorithms “, IEEE Transactions on Image Processing, Vol.2(2),pp.176-201.

[3] Soille, P. and Pesaresi,M,2002, “Advances in mathematical morphology applied to geoscience and remote sensing”, IEEE Transactions on Geoscience and Remote Sensing, Vol. 40(9), pp. 2042–2055.

[4] Mura, M.D., Benediktsson, J.A., Chanussot, J. and Bruzzone,L., 2011, “ The Evolution of the Morphological Profile: from Panchromatic to Hyperspectral Images”, Optical Remote Sensing, Sringer, pp. 123-141.

[5] Salembier, P. and Serra, J., 1995, “Flat zones filtering, connected operators and filters by reconstruction”, IEEE Transactions on Image Processing, Vol.4(8),pp. 1153-1160.

[6] Pesaresi, M. and Benediktsson, J.A.,2001, “A New Approach for the Morphological Segmentation of High-Resolution Satellite Imagery”, IEEE Transactions on Geoscience and Remote Sensing, Vol. 39(2), pp. 309-320.

[7] Soille, P. and Pesaresi, M., 2002 ,” Advances in mathematical morphology applied to geosciences and remote sensing”, IEEE Transactions on Geoscience and Remote Sensing, Vol.40(9), pp.2042-2055.

[8] Benediktson, J.A., Pesaresi, M., and Amason, K.,2003, “ Classification and feature extraction for remotesensing images from urban areas based on morphological transformations” IEEE transactions on Geoscience and Remote Sensing, Vol.46(10), pp. 2803-2813.

[9] Naegel, B., Passat, N., Ronse, C., 2007, “Grey-level hit-or-miss transforms”, pattern Recognition, 40, pp. 635-647.

[10] Matheron, G., 1975, “Random Sets and Integral Geometry”, Wiley, New York.

[11] Serra, J., 1982, “Image Analysis and Mathematical Morphology”, Vol.1, AcademicPress, London.

[12] Breiman,L., “Random Forest User Notes.”
ftp://ftp.stat.berkeley.edu/pub/users/breiman/notes_on_random_forests_v2.pdf
(Accessed on 22/03/2012)

[13] Breiman, L., Friedman, J.H., Olshen, R.A. and Stone, C.J., 1984, “Classification and Regression Trees”, Wadsworth Inc.

[14] Breiman, L., 2001, “Random Forests,” Machine Learning, Vol. 40.No. 1.

[15] Breiman,L., “Random Forest Readme file.”,

http://oz.berkeley.edu/users/breiman/randomforests.html (Accessed on 22/03/2012)

[16a] Mannor, S., Meir, R., Bengio, Y. and Schuurmans, D., 2002, "On the Existence of Linear Weak Learners and Applications to Boosting" , Machine Learning, Vol.48, pp. 219–251.

[16b] Vaghela, V.B., 2009, "Boost a weak learner to a Strong Learner Using Ensemble System Approach", Advance Computing Conference, IACC 2009, Patiala, pp. 1432-1436.

[17] Briem,G.J., Benediktsson, J.A., and Sveinsson, J.R., 2002, "Multiple Classifiers Applied to Multisource Remote Sensing Data." IEEE Trans. on Geoscience and Remote Sensing.Vol. 40.No. 10.

[18] Ho, T.K., 1998, "The random subspace method for constructing decision forests", Institute of Electrical and Electronics Engineers Transactions on Pattern Analysis and Machine Intelligence, Vol. 20(8), pp. 832–844.

[19] Reddy, B. S., Chatterji, B. N., 1996, "An FFT-based technique for translation, rotation, and scale-invariant image registration", IEEE Transactions on Image Processing, Vol.5, pp.1266-1271.

[20] Xie, H., Hicks, N., Keller, G.R., Huang, H., and Kreinovich, V., 2000, "Automatic image registration based on a FFT algorithm", In Proceedings of the ICORG-2000 International Conference on Remote Sensing and GIS/GPS, Hyderabad, India, pp.397-402.

[21] Celentano, A., Lecce, V. D., 2005," A FFT based technique for image signature generation".

[22] Casasent, D. and Psaltis, D., "Position oriented and scale invariant optical correlation," Appl. Opt., vol. 15, pp. 1793-1799, 1976.

[23] Surface texture symbols, An American national standard, The American Society of Mechanical Engineers, ASME Y14.36M-1996, pp.3-4.

[24] ISO/TS 16610-10, Geometrical Product Specification (GPS) – Data extraction techniques by sampling and filtration – Part 10: Robust Gaussian Regression filter.

[25]. Surface texture parameters, New standards, DEN EN ISO 4287/ ASME B46.1, MAHR GMBH, Germany, Edition 09-01-99.

CHAPTER 4

RESULTS AND DISCUSSION

Contents

4.1 Building Extraction using HTM Based Pattern Recognition Method with Template Matching.

4.1.1 Applied area

Considering the applicability of huge natural disasters like tsunami damaged large scale urban cities, we applied aerial images of the 2km×2km tsunami hazardous area of Ishinomaki, Miyagi prefecture. The freely available airborne image series that consists of 2011 East Japan earthquake site was used for this study. The RGB images were taken from 1986 to 2011 with different path and different azimuth angles in the same corresponding area.

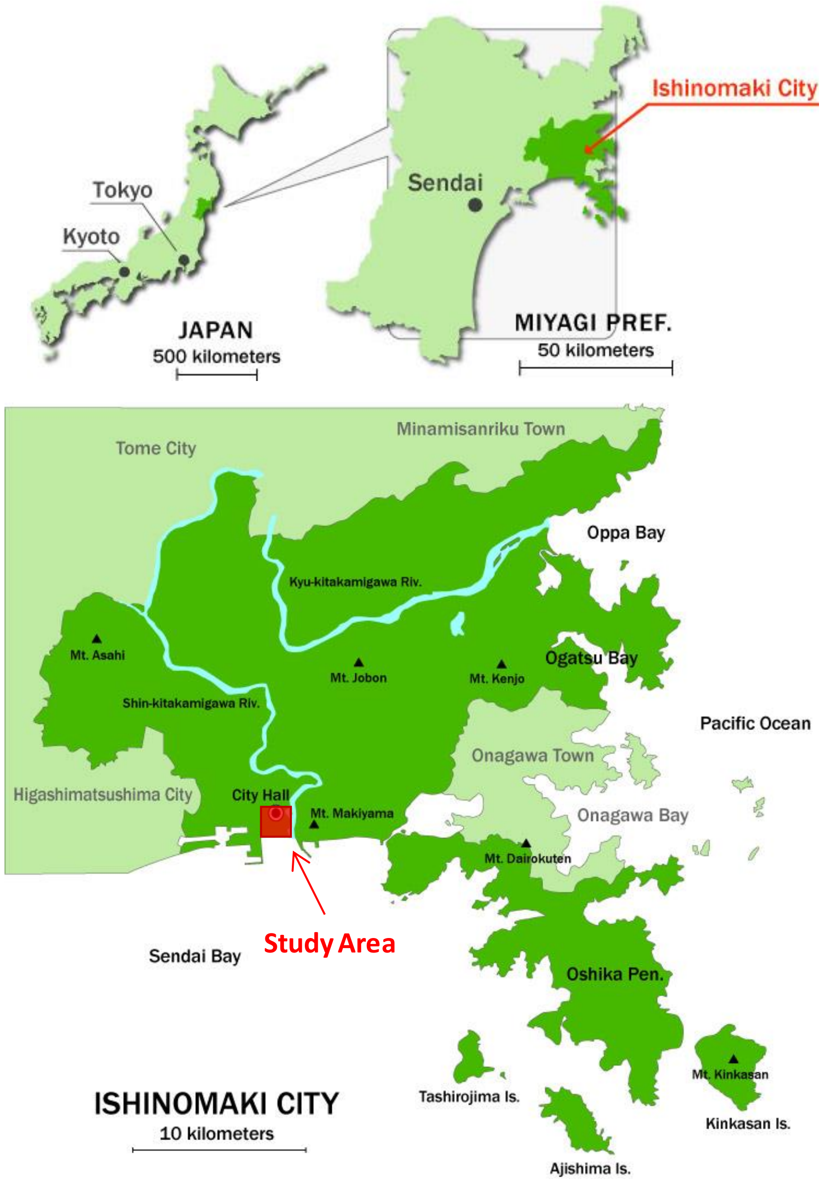

Fig.4.1.1. Applied area (2km×2km) in the Ishinomaki City, Miyagi Prefecture. Source-Ishinomaki City, http://www.city.ishinomaki.lg.jp/.

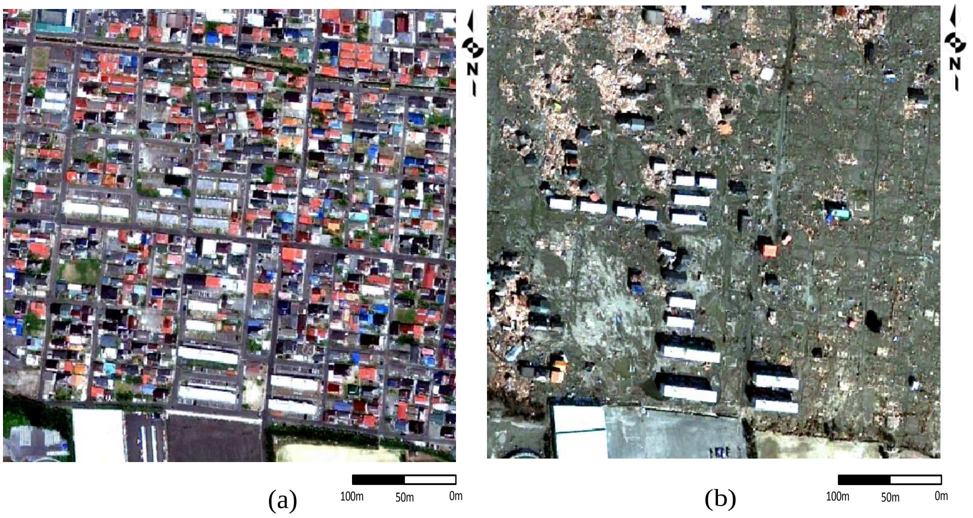

(a) (b)

Fig.4.1.2. The RGB color images of IKONOS and Quick Bird show Ishinomaki area before (a) and after (b) the Tsunami event.

Figure.4.1.1 shows the areal image download facility interface of the Geospatial Information Authority of Japan and Figure.4.1.2 shows sample images of time series that downloaded from the same location in candidate area near Ishinomaki bay.

4.1.2 Results

The results of building roof extraction using of morphological pattern matching techniques that was explained in section 3.2are presented in this section. (Refer section 3.2., Chapter 3.)
It shows the optimization of the templates of SE size and shape gives extracted results, for the correspondent's shape of building roof chosen. (Refer 3.2.3. Optimizations the shape and size of the templates in chapter 3). In this study, we found that square shape structural elements template (SET) gave quite high accuracy building extraction rather than other shapes such as disk, triangular or rectangular. The optimization of HTM for effectiveness of building sizes 7×7, 11×11, 15×15 and 19×19, the SE size of foreground and background gave values of 3:9, 7:17, 5; 19 and 9; 21 or 23.

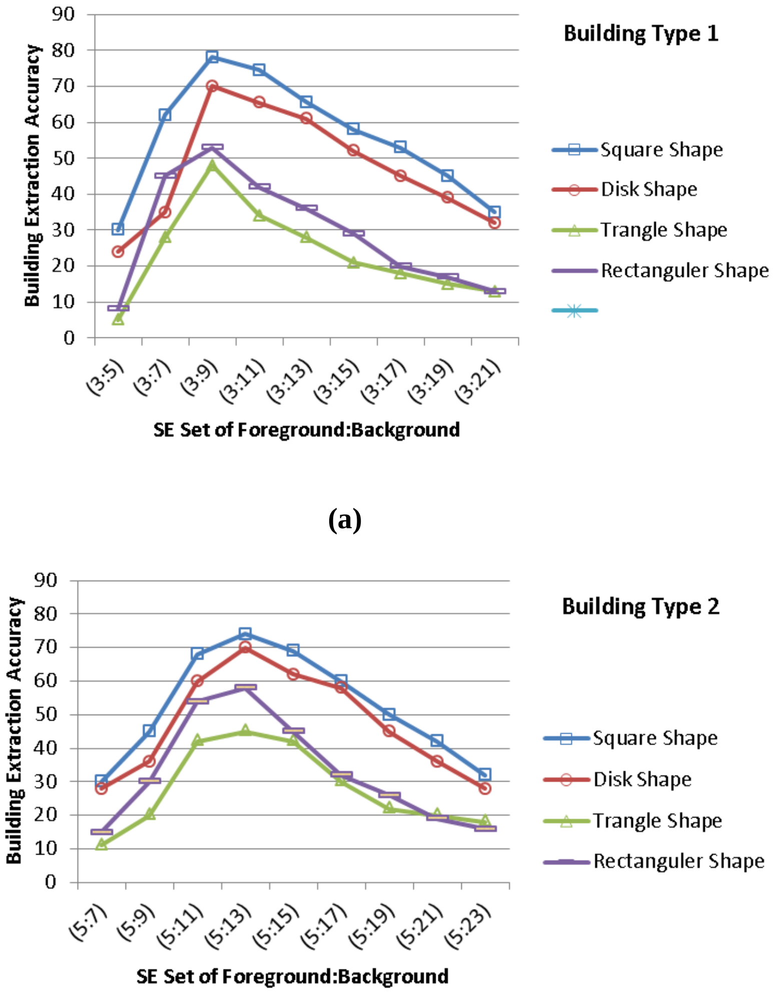

(a)

(b)

Fig.4.1.3. Building extraction amount according to the SET type and FG: BG sizes.

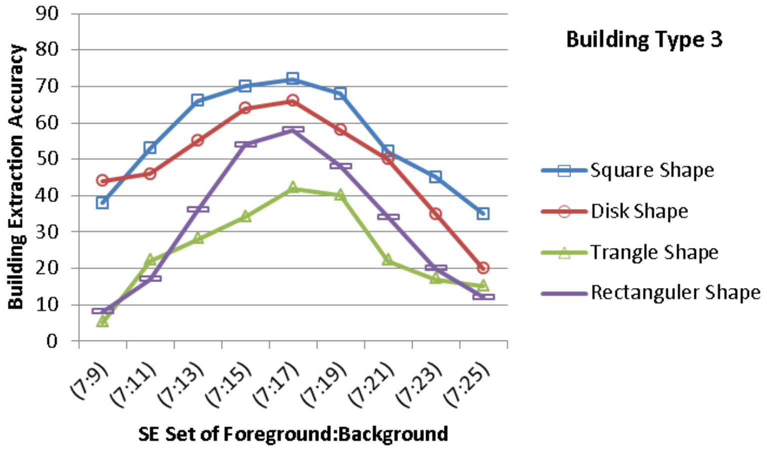

(c)

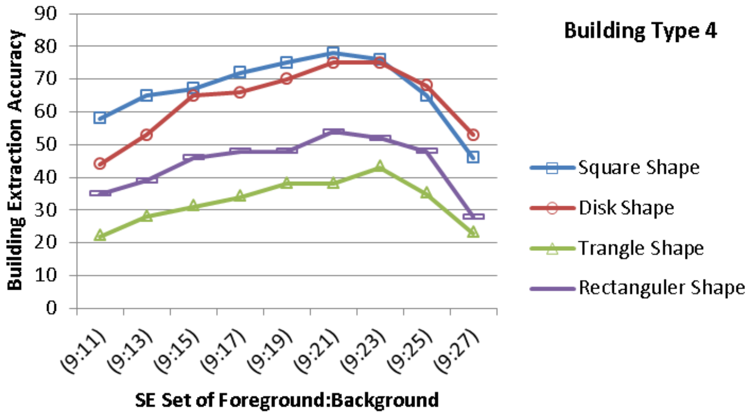

(d)

Fig.4.1.3. Building extraction accuracy according to the SET type and FG: BG sizes.(*continue*)

Figure.4.1.3 shows building extraction accuracy due to the structural element type. Building extraction accuracy according to structural element type in maximum FG; BG sizes are shown in Figure.4.1.4.

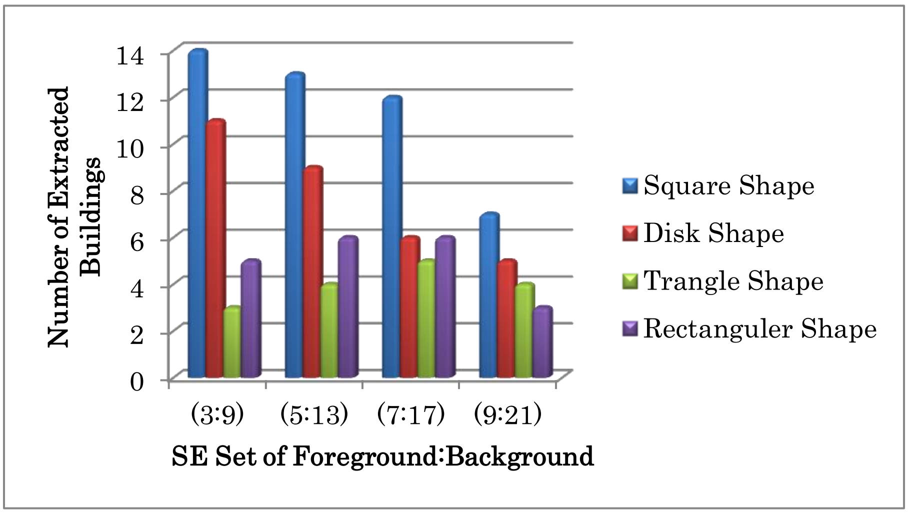

Fig.4.1.4. Building extraction accuracy according to structural element type in maximum FG; BG sizes.

The results have shown the usefulness of the proposed method during detection of various types of building, as illustrated by the portions given in Figure 4.1.5.

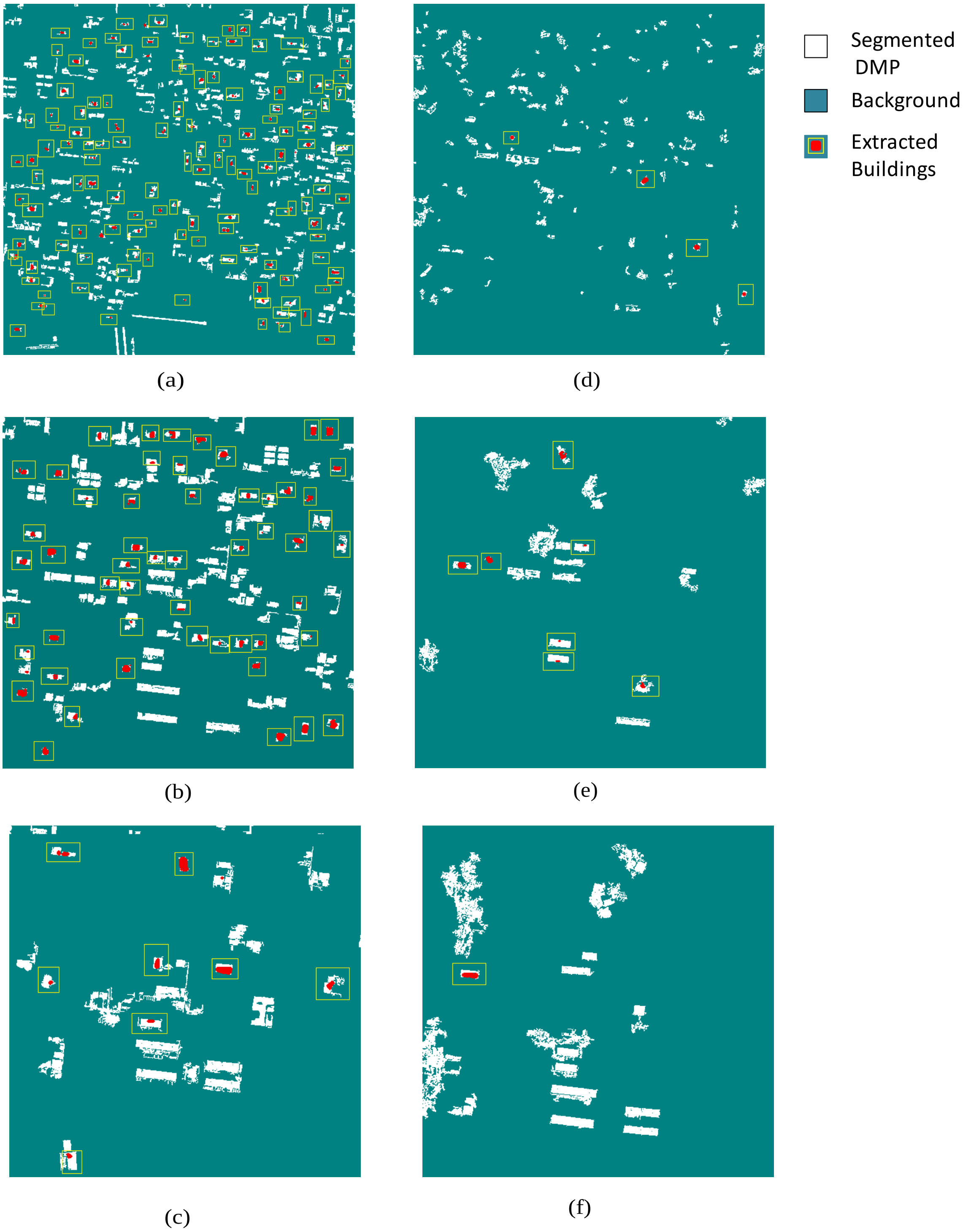

(a) (d) (b) (e) (c) (f)

Fig.4.1.5. The results of the building extraction according to approached method. Identified buildings are shown in red color, (a),(d) pre and post event building roofs corresponded to SE=7, (b),(e) pre and post event building roofs corresponded to SE=11 and (c), (f) show the pre and post event building roofs corresponded to SE=15 respectively. The color of violet, green and red are correspond the background, binarized features and identified building.

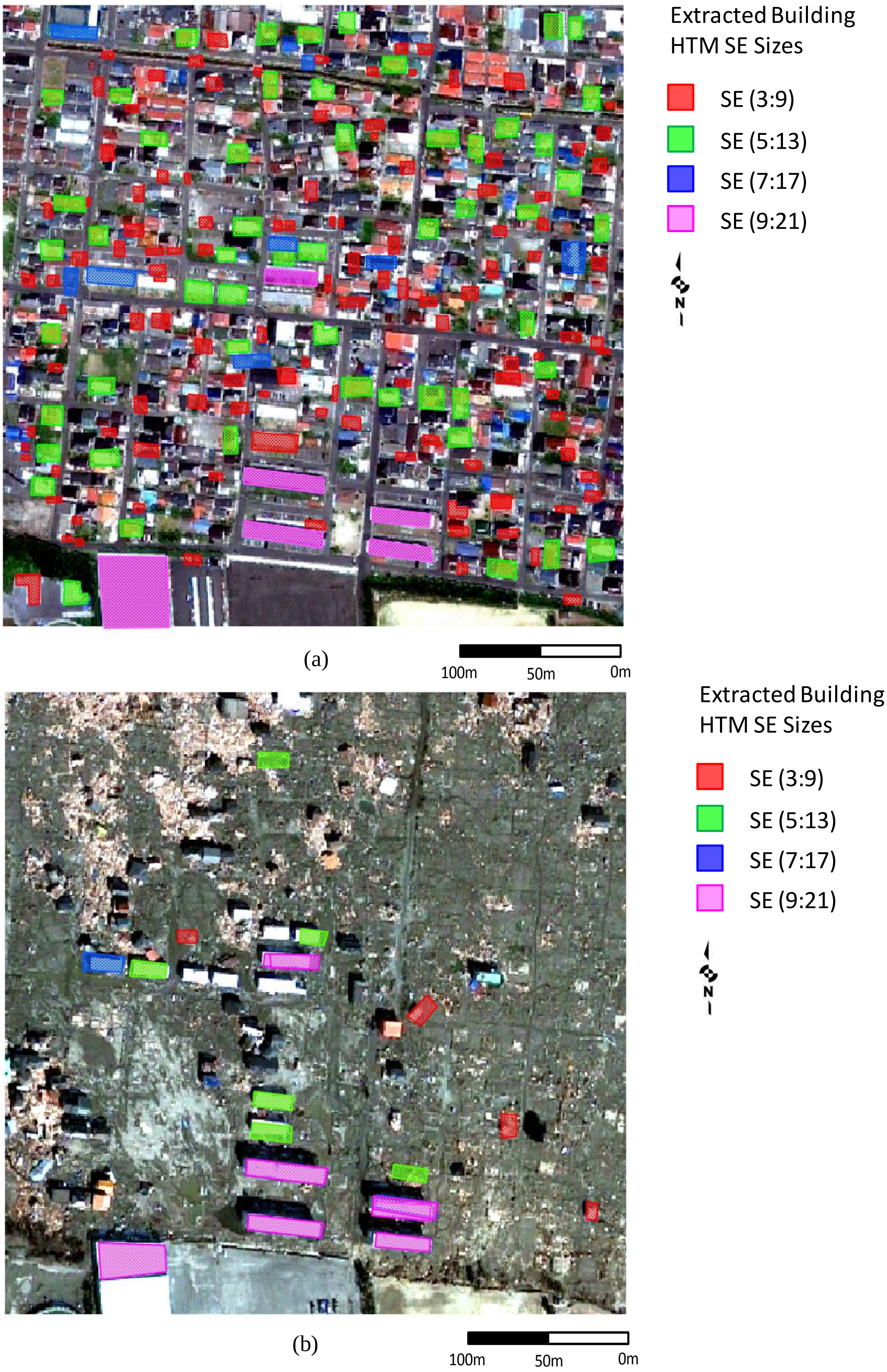

(a)

(b)

Fig.4.1.6. Recognitions of building for each SE template set before (a) and after (b) the tsunami event.

The sample area was selected from Ishinomaki area, Miyagi Prefecture. The ground references for the accuracy assessments have been obtained by careful visual inspection of separate data resources, including aerial imagery, existing GIS data and *in situ* field survey. Here the recognition of building for each SE template set before and after the tsunami event are shown in Figure.4.1.6. The Table.4.1.1 and further the Table.4.1.2 show the building recognition results before and after the tsunami hazard.

Table.4.1.1. Accuracy assessment of building recognitions in each SE sets using the proposed method before the tsunami event.

Before the Tsunami event			
SE size of HTM	**Precision**	**Recall**	**Overall Accuracy**
SE=3;9	93.86	75.08	71.59
SE=5;13	95.61	77.34	74.68
SE=7;17	96.21	79.54	77.13
SE=9;21	96.25	80.51	78.25

Table.4.1.2. Accuracy assessment of building recognitions in each SE sets using the proposed method after the tsunami event.

After the Tsunami event			
SE size of HTM	**Precision**	**Recall**	**Overall Accuracy**
SE=3;9	92.07	78.24	73.3
SE=5;13	93.18	77.36	73.21
SE=7;17	93.26	78.31	74.11
SE=9;21	94.52	82.81	78.41

Here the Figure.4.1.7 shows the accuracy of the building recognition using the proposed methodology.

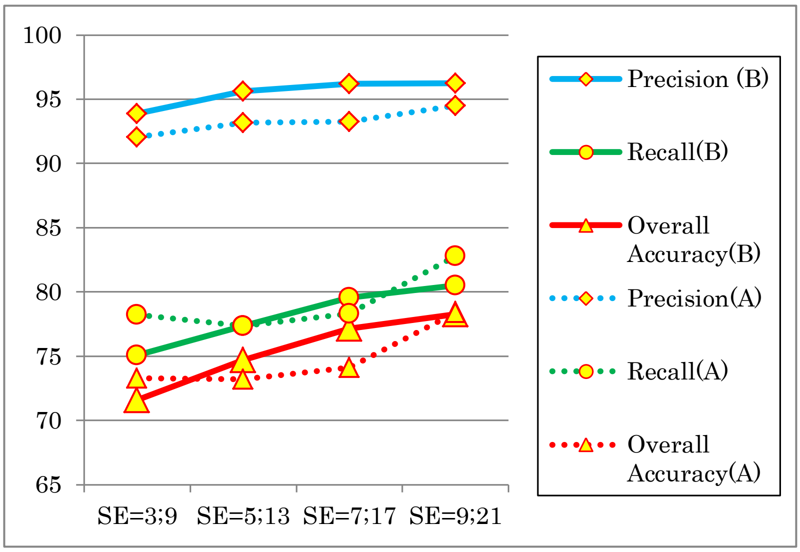

Fig.4.1.7. The graph of accuracy assessment of building recognitions in each SE sets before and after the tsunami event. (Here the (B) means before and (A) after the tsunami event).

The quality of the results was assessed by using existing GIS data as ground truth. The Table.4.1.3 shows the accuracy assessment of damaged building recognitions using the proposed method. For the application area, the method detected 904 washed away or damaged buildings among 1150 and 389 survived among 442 buildings due to the tsunami event. The error extraction of building structure could be due to over fitting of the decision surface to the data. According to the results of building recognitions the HTM based algorithm shows a quite high accuracy for large scale building extraction. The Precision accuracies of the building recognitions of both before and after the tsunami are always high, that means the building that identified using the proposed method has a high probability to match with ground truth. But quite low recall accuracy shows the difficulties of the pattern matching process.

Table.4.1.3. Accuracy assessment of the damaged building recognitions using the proposed method.

Unit Base Accuracy Assessment (HTM)		Damaged Building Extracted Result			
		Damaged or washed away	Survived	Total	Producer Accuracy
Ground Truth Data	Damaged or washed away	904	246	1150	78.61%
	Survived	53	389	442	88.00%
	Total	957	635	1592	
	User Accuracy	94.46%	61.26%		81.22%

4.1.3. Discussion.

Automated detection of features such as building roof for template matching and pattern recognition is a great significance in the image processing field. In this section, a method which is developed optimizing the shape and size of hit-or-miss morphological filtering parameters with morphological operators is presented for building roof target detection. Morphological operations of opening and closing with constructions are applied to segmented images. Hit-or-miss transform has been successfully applied for template marching in binary images. The proposed approach involves several advanced morphological operators among which an adaptive hit-or-miss transform with varying size and shape of the structuring elements. VHR space borne images consisting of a pre and post 2011 Pacific coast of Tohoku earthquake and tsunami site of the Ishinomaki, Miyagi area in Japan were used.

The first step was to segment structural information using morphological opening and closing by reconstruction operators. There for the pre-generated gray level airborne images of pre and post-earthquake and tsunami event in the Ishinomaki area in Miyagi prefecture were applied to the morphological operators. The shadows of the buildings were masked and removed using their low spectral values. This work is a further extension of our previous study by introducing binary images and hit-or-miss transform. The segmented images were applied to hit-or-miss transform to extract the building roofs. The HMT is useful for binary document image pattern matching tasks. We have shown the results of an experiment on pattern matching for building roofs, to illustrate the effects of FG and BG blur, and of regular sub-samplings of the templates. Pattern matching techniques are critical for all aspects of the analysis of document images. One of the most important uses of pattern matching is in the analysis of roof shapes. For binary input, the result of image processing can be either binary or gray color (integer value) images. DMP applied before the HTM, because the binary results are much faster to compute. We have shown the results of an experiment with pattern matching for building roofs, to illustrate the effects of FG and BG blur, and of regular sub-samplings of the templates. The templates of SE size and shape gives extracted results, for building roof in the chosen candidate area. The Square shape and disk shape SE gives high recognition accuracy for building roof. The optimized FG and BG sizes for building roof detection are investigated in this study.

4.2. Building Extraction using SVM and Random Forest Classification Methods.

Building extraction results using morphological operators and classification methods that were explained in section 3.1, 3.3 and 3.4 (Refer section 3.1, 3.3 and 3.4 in chapter 3) are demonstrated here.

4.2.1. Study Area

In the first step small area (480m×480m) was tested for damaged building identification. We used freely available airborne image series and the GIS data sets of 2011 East Japan earthquake site in Ishinomaki area in Miyagi prefecture. The RGB images were taken between May and September in the year 2011 after the earthquake and tsunami hazard in the corresponding area. Figure.4.2.1 shows the GIS building footprint database (left) and the optical image (right) facility interface website of the Geospatial Information Authority of Japan

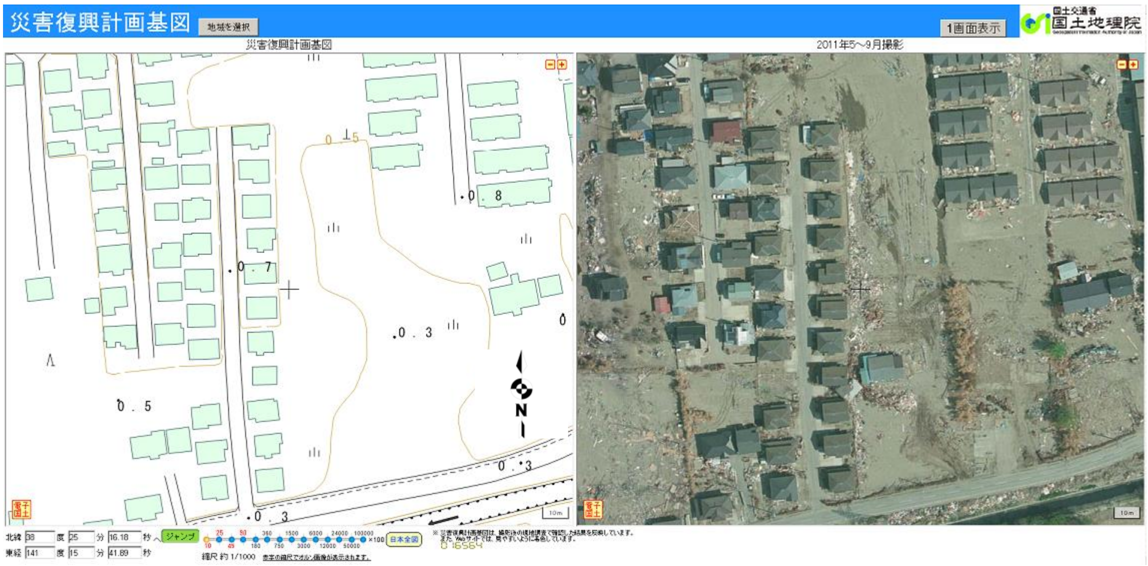

北緯 38 度 25 分 16.18 秒
東経 141 度 15 分 41.89 秒
縮尺 約 1/1000

Fig.4.2.1. Interface of the GIS data of building footprint and correspond aerial image of the tsunami damage area in the Ishinomaki from Geospatial Information Authority of Japan.Source- (平成 23 年東日本大震災に関する情報提供,国土地理院).

4.2.2. Results

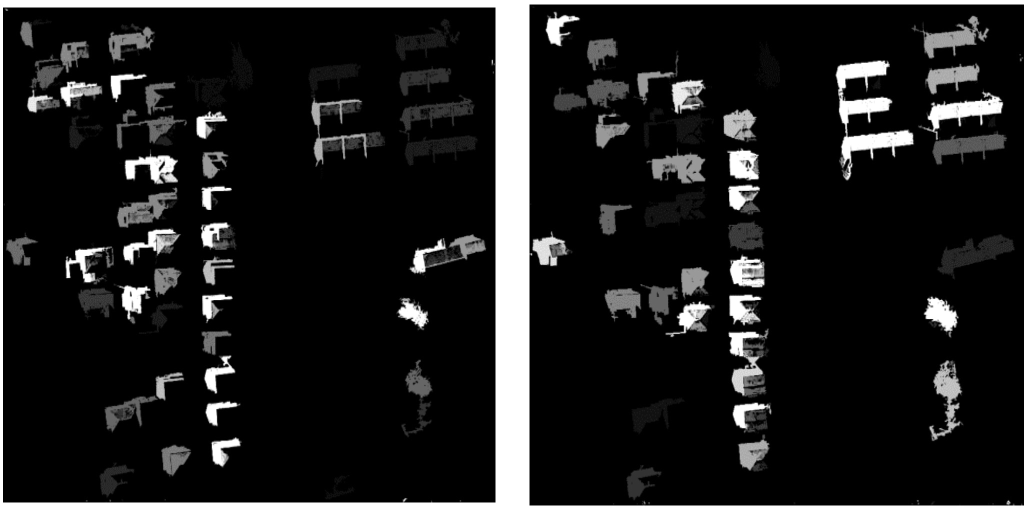

(a) Closing (SE =7) (b) Opening (SE = 7)

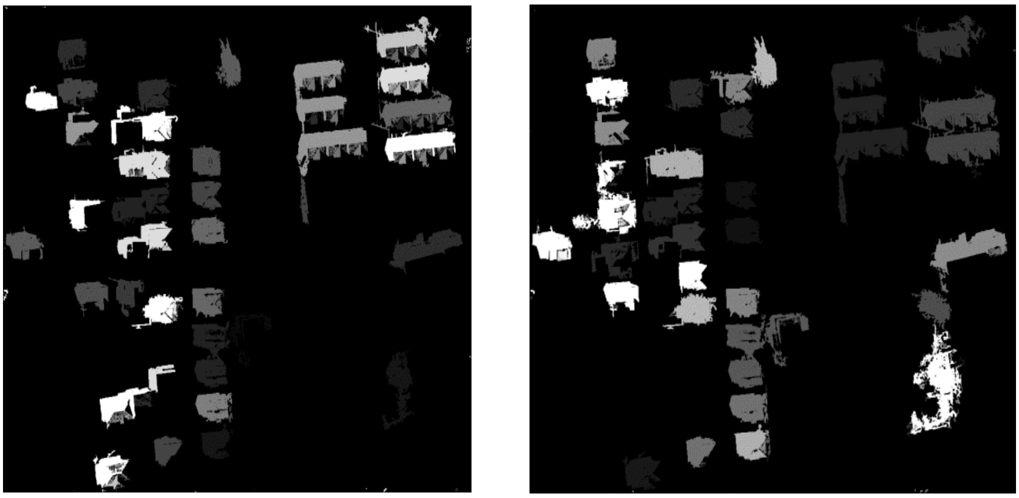

(c) Closing (SE =15) (d) Opening (SE=15)

Fig. 4.2.2. DMP of corresponding sample area.

The Figure.4.2.2 shows produced digital morphological profile of sample area in image that downloaded from the location in candidate area near Ishinomaki bay.

In our previous approaches in chapter 2, 4, 5 and 6, the classification was done either with a statistical classifier of Gaussian maximum likelihood (ML), neural network, or ISODATA.SVM shows high accuracy results in the situation of limited training set in hazardous areas and is definitely among the most used kernel learning algorithms. It performs robust nonlinear classification of samples using the kernel trick. Here, it is proposed to use the Support Vector Machine (SVM) and the Random Forest (RF).

Random forest (RF) is a new and powerful statistical classier that is well established in many other disciplines. Advantages of RF compared to other statistical classifiers include (1) very high classification accuracy; (2) a novel method of determining variable importance; (3) ability to model complex interactions among predictor variables; (4) flexibility to perform several types of statistical data analysis, including regression, classification, survival analysis, and unsupervised learning; and (5) an algorithm for imputing missing values. We compared the accuracies of RF and SVM classifiers for DMP based building extraction in this chapter.

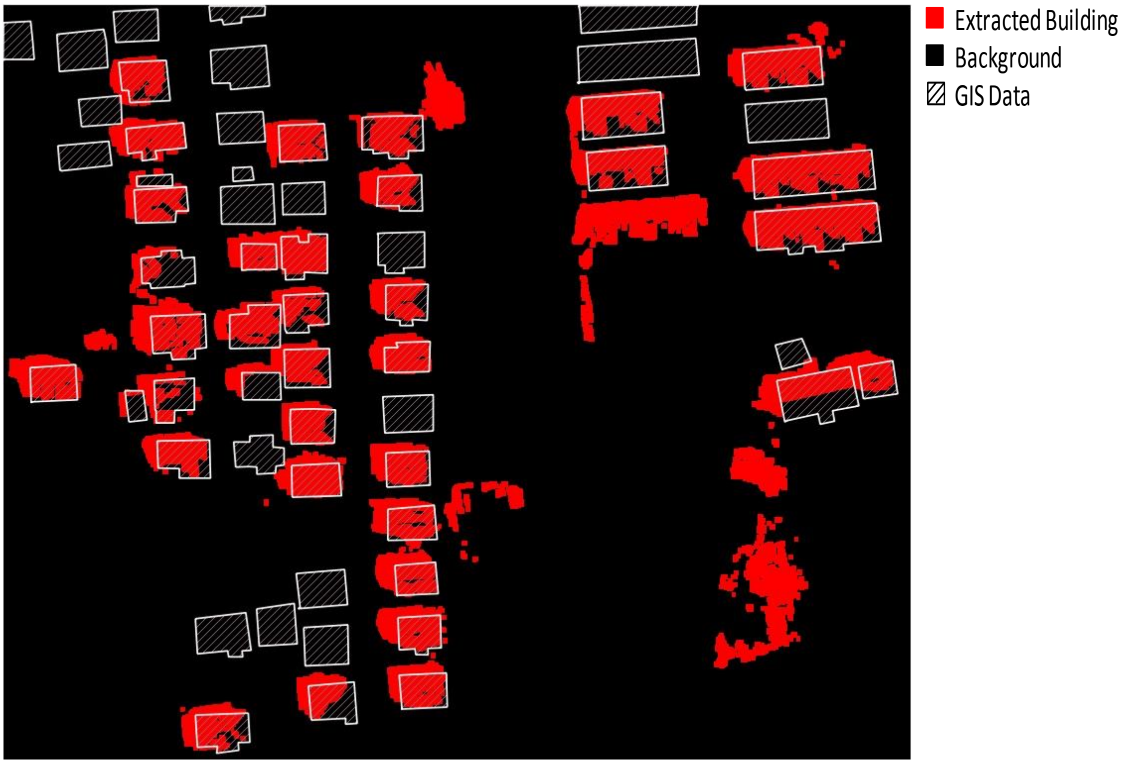

(a) SVM classification results

(b) Random Forest classification results

Fig. 4.2.3. Building extraction results of corresponding sample area. (a) Shows the results of the SVM base classification method and (b) shows the Random Forest based classification results.

Figure.4.2.3 shows the results obtained by using the SVM and Random forest classification methods. The Table.4.2.1 and Table.4.2.2 give an overview of the final results. The accuracy assessments were carried out using GIS data as ground truth.

The SVM classification method detected 40 remaining building correctly, whereas 9 buildings were undetected. Sums of 48 building were detected correctly by RF classification approach, but 5 building remain undetected. According to the accuracy assessment, RF classification method gives quite high overall accuracy value 84.21% than the SVM approach which gave 76.92%.

Table.4.2.1. Accuracy of the extracted result based on SVM Classification

Unit Base Accuracy Assessment (SVM)		Damaged Building Extracted Result			
		Building	Non	Total	Producer Accuracy
Ground Truth Data	Building	40	9	49	81.63%
	Non	3			
	Total	43		52	
	User Accuracy	93.02%			76.92%

Table.4.2.2. Accuracy of the extracted result based on Random Forest Classification

Unit Base Accuracy Assessment (RF)		Damaged Building Extracted Result			
		Building	Non	Total	Producer Accuracy
Ground Truth Data	Building	48	4	52	92.31%
	Non	5			
	Total	53		57	
	User Accuracy	90.57%			84.21%

This study shows higher success in the application of RF to building extraction using DMP and object-based parameters. Results from this study suggest that RF, used in conjunction with object-based data derived from high resolution airborne imagery, can accurately classify urban features fallow despite variability in the DMP data set of closing, here in Ishinomaki area SE size was 7m to 19m. The incorporation of O-O methodology with RF efficiently allows for the integration of complex machine learning techniques with an advanced approach to image analysis. It was also found that classification predictions generated through RF could be easily incorporated into the object database format for GIS-based spatial analysis also.

4.2.3. Discussion

This section presented an approach for automated, multi-scale building extraction from high-resolution airborne imagery in an event of a large scale natural hazard. Our algorithm tested here combines techniques from mathematical morphology with Support Vector Machine (SVM) and Random Forest (RF) classification methods to identify building footprints in scenes, the tsunami event remote sensing airborne image data set, which is both a challenging and important classification problem in building extraction. Pre and post airborne imagery of 2011 East Japan earthquake and tsunami site of Ishinomaki area in Miyagi prefecture is used. The proposed method was tested for small scale (480m×480m) area in Ishinomaki, Miyagi prefecture. There are three major components exists in this work: First, the Differential Morphological Profile (DMP) of the images is constructed using structuring elements (SE) of varying sizes from 7 to 19. Several preprocessing techniques were applied to the pre and post event airborne images such as geometric registration and the gray color image generation. Then the SVM and RF are applied to DMP serious for building extraction. In the final stage, extracted candidate objects from both SVM and RF methods are evaluated as accuracy assessment.

Indeed, a new method of the image classification Random Forest was investigated for classification of a multi-source remote sensing and geographic data set, which is both challenging and important classification problems in remote sensing. Both SVM and RF classifying methods are investigated for close range airborne imagery that consists of Tsunami hazard. This gave higher accuracy in building extraction than all other classification methods. However, in this experiment, the Random Forest classifier performed well than SVM. The proposed method has full automated rapid building extraction process from pre and post image registration to damage estimation for images with very large and complex homogeneous regions. In the next step we propose to apply this methodology with further extend into large scale area. The Random Forest will be used as the classifier that performed well in this study.

4.3 Building Extraction using Random Forest Classification Method in Large areas

4.3.1 Study area

Considering the applicability of huge natural disasters like tsunami damaged in large urban cities, we applied aerial images of the size 2km×2km in a tsunami hazardous area of Ishinomaki, Miyagi prefecture. The freely available airborne image series that consists of 2011 East Japan earthquake site was used for this study. The RGB images were taken from 1986 to 2011 with different path and different azimuth angles in the same corresponding area.

Fig.4.3.1. Applied area (800mx800m) in the Ishinomaki City, Miyagi Prefecture. Source- Ishinomaki City, http://www.city.ishinomaki.lg.jp/

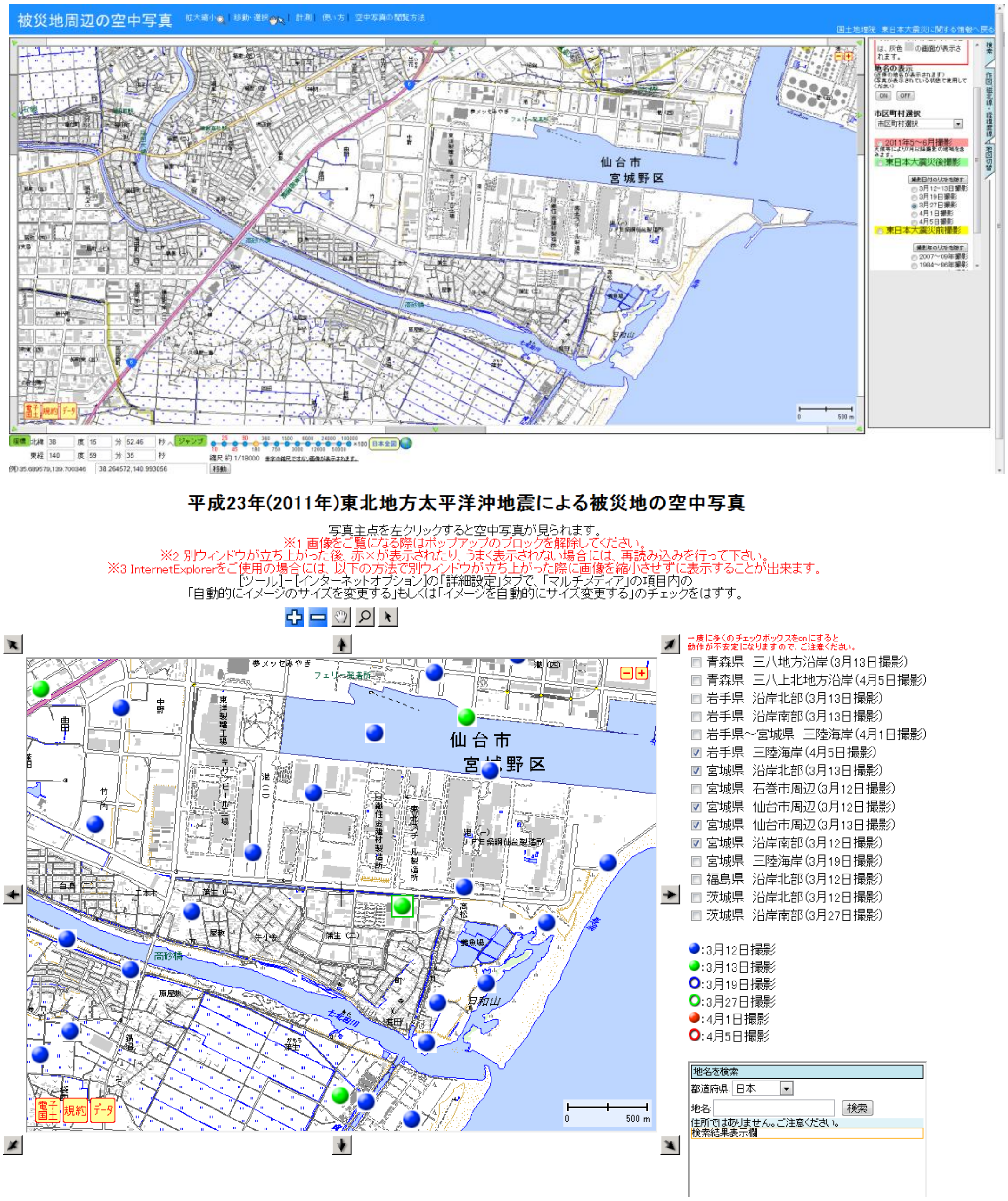

平成23年(2011年)東北地方太平洋沖地震による被災地の空中写真

写真主点を左クリックすると空中写真が見られます。
※1 画像をご覧になる際はポップアップのブロックを解除してください。
※2 別ウィンドウが立ち上がった後、赤×が表示されたり、うまく表示されない場合には、再読み込みを行って下さい。
※3 InternetExplorerをご使用の場合には、以下の方法で別ウィンドウが立ち上がった際に画像を縮小させずに表示することが出来ます。
[ツール]−[インターネットオプション]の「詳細設定」タブで、「マルチメディア」の項目内の
「自動的にイメージのサイズを変更する」もしくは「イメージを自動的にサイズ変更する」のチェックをはずす。

一度に多くのチェックボックスをonにすると
動作が不安定になりますので、ご注意ください。

☐ 青森県　三八地方沿岸(3月13日撮影)
☐ 青森県　三八上北地方沿岸(4月5日撮影)
☐ 岩手県　沿岸北部(3月13日撮影)
☐ 岩手県　沿岸南部(3月13日撮影)
☐ 岩手県〜宮城県　三陸海岸(4月1日撮影)
☑ 岩手県　三陸海岸(4月5日撮影)
☑ 宮城県　沿岸北部(3月13日撮影)
☐ 宮城県　石巻市周辺(3月12日撮影)
☑ 宮城県　仙台市周辺(3月12日撮影)
☑ 宮城県　仙台市周辺(3月13日撮影)
☑ 宮城県　沿岸南部(3月12日撮影)
☐ 宮城県　三陸海岸(3月19日撮影)
☐ 福島県　沿岸北部(3月12日撮影)
☐ 茨城県　沿岸北部(3月12日撮影)
☐ 茨城県　沿岸南部(3月27日撮影)

●:3月12日撮影
●:3月13日撮影
○:3月19日撮影
○:3月27日撮影
●:4月1日撮影
○:4月5日撮影

地名を検索
都道府県: 日本
地名: 検索
住所ではありません。ご注意ください。
検索結果表示欄

Fig.4.3.2. Areal image download facility interface of Geospatial Information Authority of Japan.

Source- (平成 23 年東日本大震災に関する情報提供,国土地理院)

Here in Figure.4.3.1 shows the areal image download facility interface of the Geospatial Information Authority of Japan and Figure.4.3.2 shows sample images of time series that downloaded from the same location in candidate area near Ishinomaki bay. The downloaded pre and past event airborne images of Ishinomaki area are shown in Figure 4.3.3 (a) and (b).

(a) Year 2010 image

(b) Year 2011 image

Fig.4.3.3. Pre and post event airborne RGB images of Ishinomaki area in same candidate location.

4.3.2 Results

Following figures, Figure.4.3.4 and Figure 4.3.5 show 6 differential morphological profiles among 20 SE (SE set of 3, 5, 7, 9, 11, 13, 15, 17, 19, 21) of opening and closing before and after the event respectively. The DMP result was applied to Flat Element (FE) Building Roof Reconstruction (BRR) process before the classification (refer 3.3.1.(c)). Figure.4.3.6 and Figure.4.3.7 illustrate set of 4 BRRs (1 closing DMP and 3 opening DMP) among 20, before and after the tsunami event respectively.

In this case the training data were selected using the size of the roof (small, medium and large, according to approximately the size of 9×9, 13×13 and 17×17). Both pre event and post event BRRs were applied to the RF classification method for building extraction. For the general theory of this classification method, refer section 3.3.2 in Chapter 3.

In the Random Forest classification, we tested two cost functions of Gini index and Shannon entropy for pre generated 2km×2km BRR dataset. Table.4.3.1 shows the classification accuracies for the impurity of Gini index and entropy. According to the results, the choice of the cost function (Gini index or entropy) has a small effect on the performance of the Random Forest that consists of a large number of trees because they are quite consistent with each other. However Gini index shows better performance than entropy considering the time consumption of running the algorithm. The low split variables (e.g.4) of each node give high accuracy because of high randomness rather than high split variables (e.g. 20). For further study, we selected Random Forest algorithm parameterized with impurity=Gini index, number of trees= 1000 and split variables of each node=4 up to now.

Table.4.3.1. Classification accuracies for the impurity of Gini index and entropy

Impurity	Number of trees	Split variables	Runtime (min:s)	Out-of-bag acc. (%)	Test set acc. (%)
Gini index	100	4	02:32	83.81	81.66
	500	4	05:40	87.73	88.14
	500	12	11:24	88.63	87.42
	1000	4	14:25	95.12	94.43
	1000	20	22:06	92.61	91.41
Shannon entropy	100	4	03:41	79.44	81.92
	500	4	06:08	88.55	86.83
	500	12	13:39	87.03	89.19
	1000	4	18:25	93.76	92.85
	1000	20	31:09	91.61	92.11

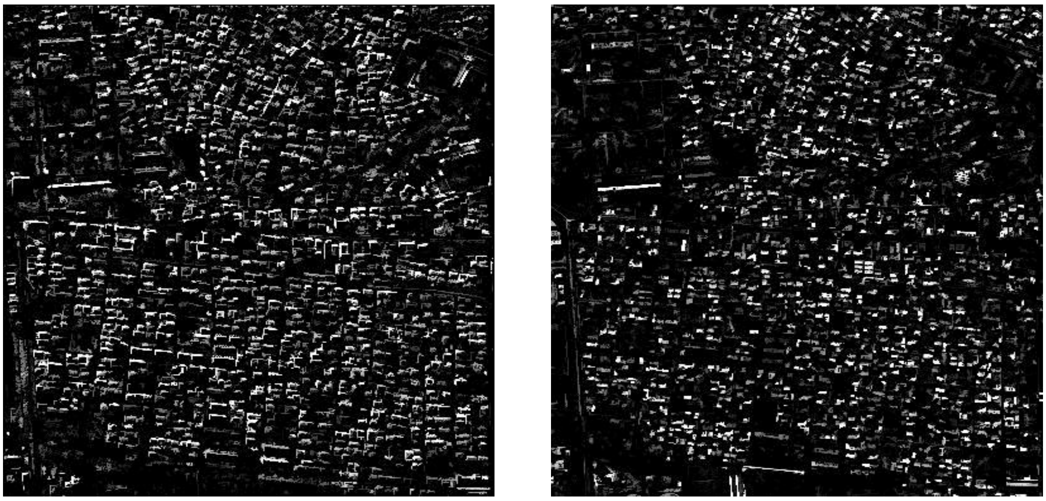

(a) Closing D=(7)

(d) Opening D=(7)

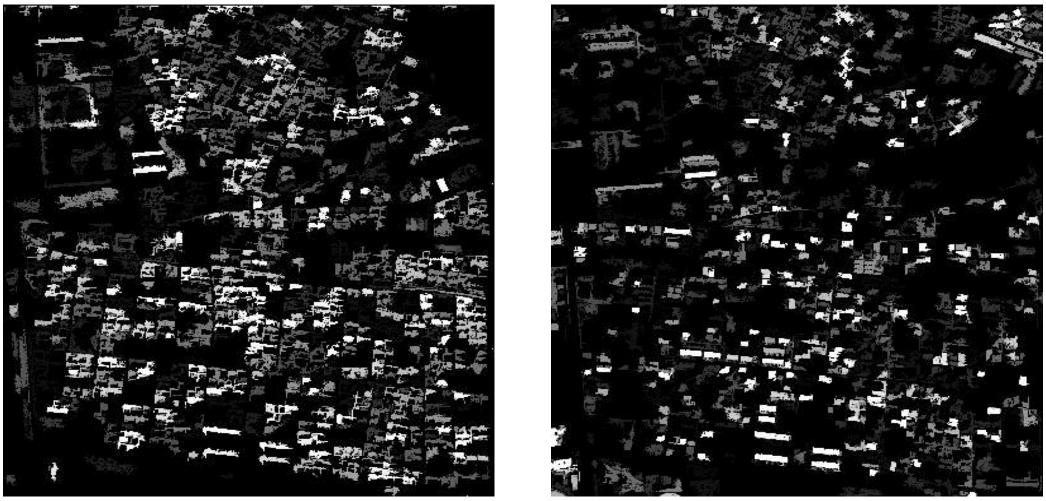

(b) Closing D=(11)

(e) Opening D=(11)

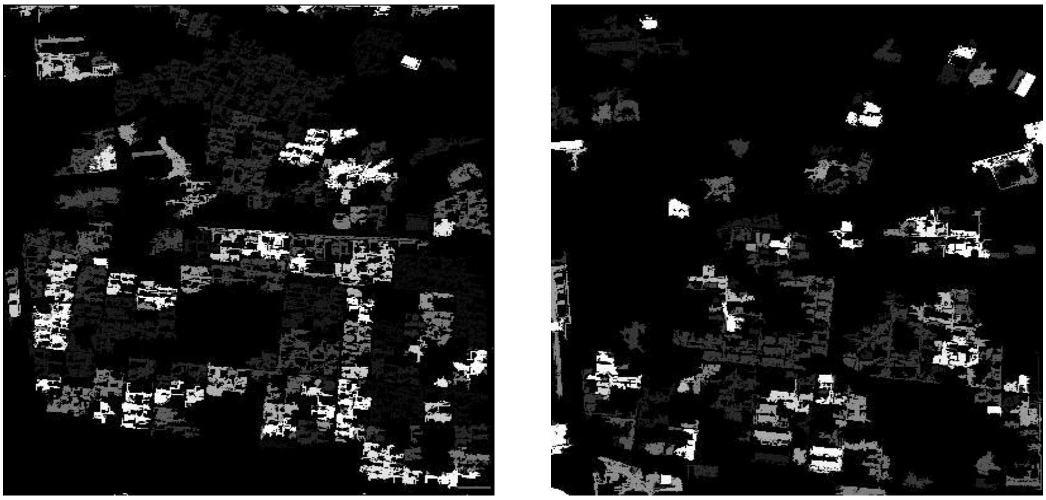

(c) Closing D=(15)

(f) Opening D=(15)

Fig.4.3.4. The differential morphological profile sets of opening and closing before the tsunami event.

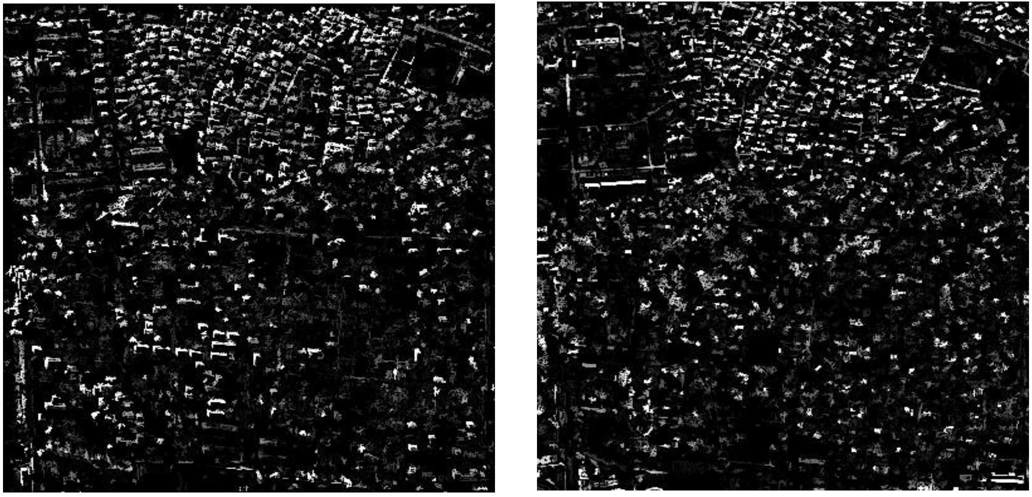

(a) Closing D=(7)

(d) Opening D=(7)

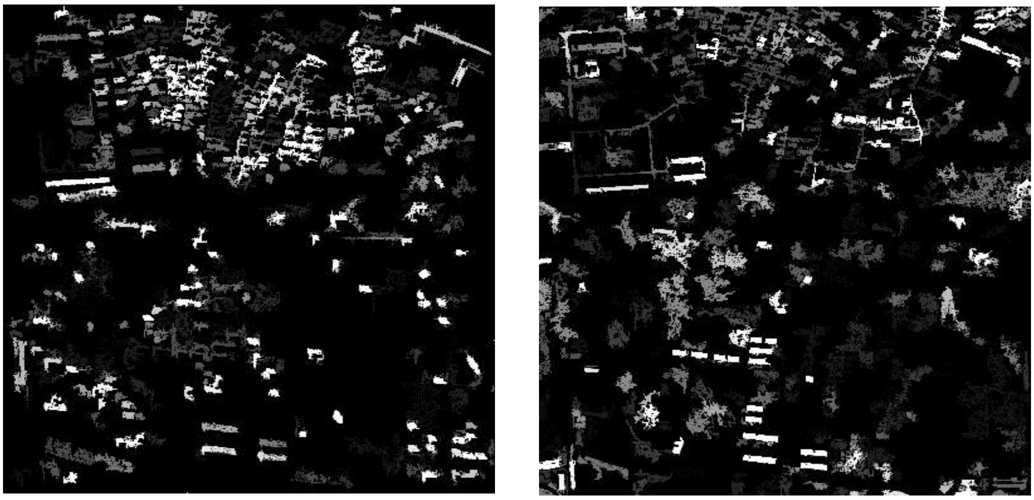

(b) Closing D=(11)

(e) Opening D=(11)

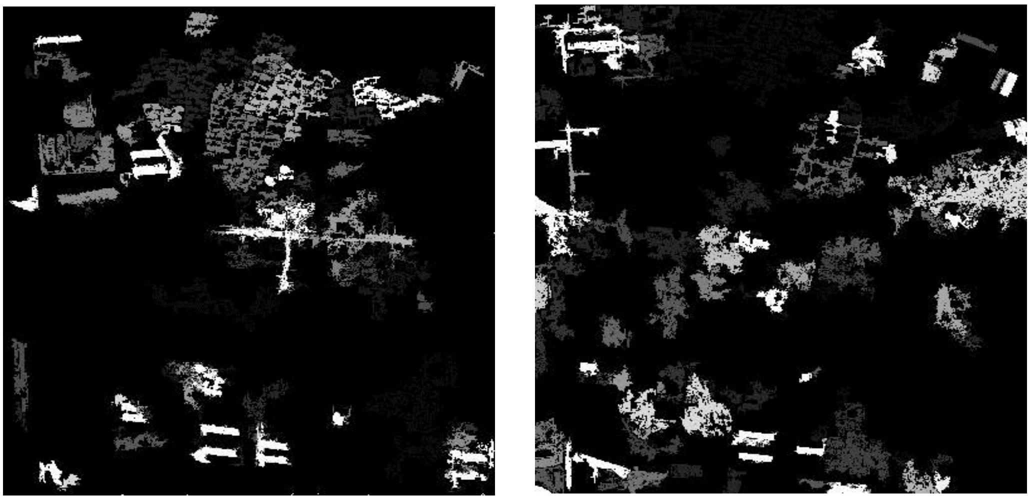

(c) Closing D=(15)

(f) Opening D=(15)

Fig.4.3.5. The differential morphological profile sets of opening and closing after the tsunami event.

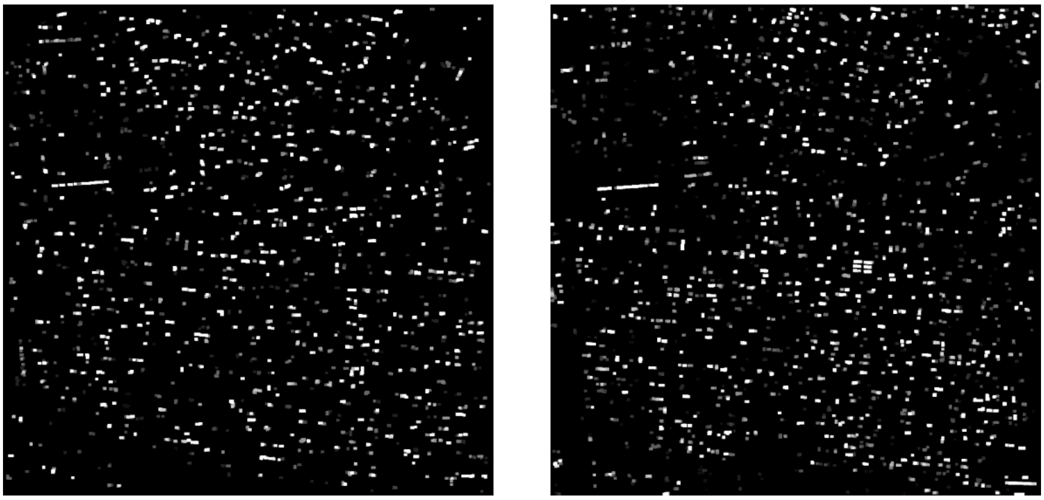

(a) Closing D=(7) (d) Opening D=(7)

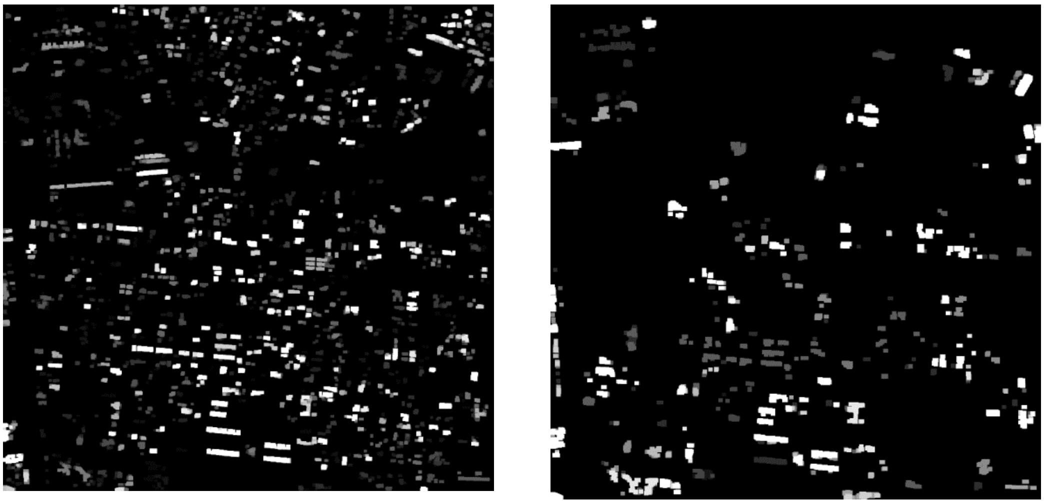

(b) Opening D=(11) (e) Opening D=(15)

Fig.4.3.6. The extended differential morphological profile sets of opening and closing before the tsunami event.

The test set was selected in a random manner (uniform) among the whole data in RF. To estimate the test set accuracy, the out of bag samples (the remaining training set samples that are not in the bootstrap for a particular tree) of each tree can be run down through the tree (cross-validation). The results are combined with a majority vote as before, and when compared to the actual labels, they yield a lower estimate of the classification error [34], as each sample can only be tested on the trees for which it was out-of-bag (so the effective ensemble for the out-of-bag estimate is smaller than the full ensemble used to train the entire forest).

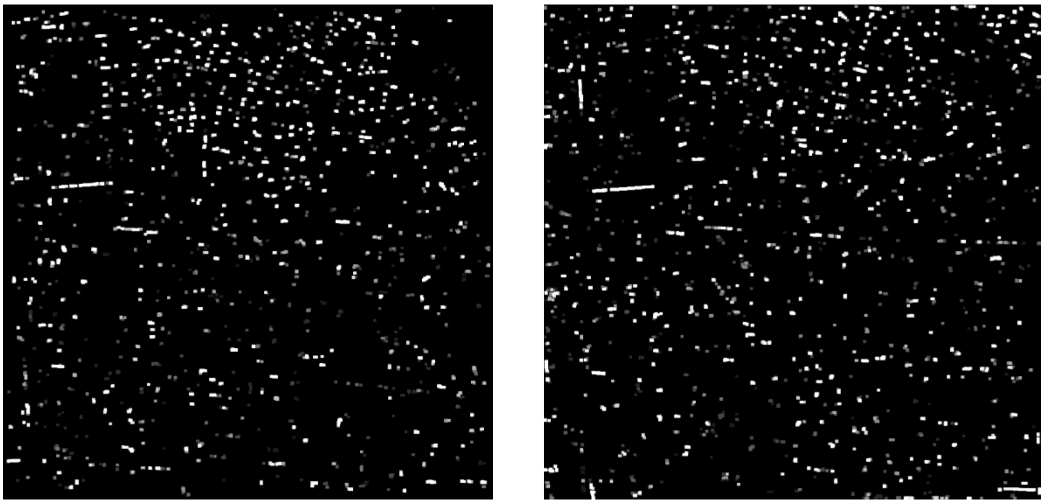

(a) Closing D=(7) (d) Opening D=(7)

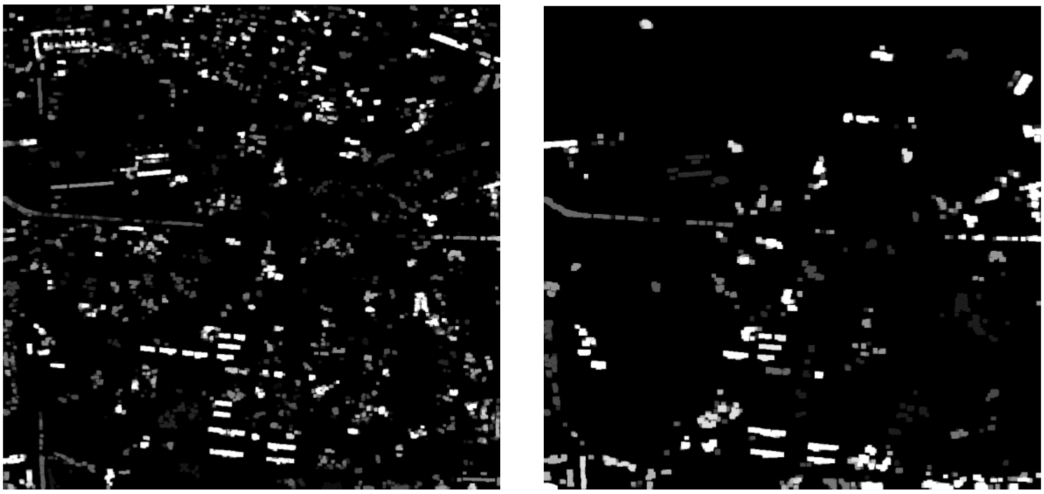

(b) Opening D=(11) (e) Opening D=(15)

Fig.4.3.7. The extended differential morphological profile sets of opening and closing after the tsunami event.

Table.4.3.2 and 4.3.4 show the pre and post event experimental results for Random Forest classification. The highest OOB accuracy and test accuracies were obtained with 1000 trees and with, 4 and 3 split variables. The OOB accuracy quit low than the test accuracy, this is mostly due to the fact that each bootstrap uses a large amount of training samples while few remaining samples use to estimate OOB accuracy. It is interesting to note that the large value of split variables (20) gives lower accuracy because of lower randomness.

Table.4.3.2. Pre event classification accuracies for the Random Forest classifier

Number of trees	Split variables	Runtime (min:s)	Out-of-bag acc. (%)	Test set acc. (%)
100	2	2.01	82.21	83.05
200	2	3.18	84.56	85.21
400	2	5.39	85.44	85.22
600	2	6.52	87.33	88.37
800	2	7.25	88.12	90.02
1000	2	8.51	88.77	91.32
400	3	6.33	87.18	86.01
1000	3	11.08	93.91	95.41
1000	4	14.25	**94.12**	**96.43**
1000	12	18.05	93.51	95.38
1000	20	22.06	92.62	93.77

Table.4.3.3. Post event classification accuracies for the Random Forest classifier

Number of trees	Split variables	Runtime (min:s)	Out-of-bag acc. (%)	Test set acc. (%)
100	2	1:48	73.22	82.55
200	2	2:50	74.21	86.98
400	2	5:07	74.81	86.96
600	2	6.21	75.17	88.31
800	2	7.15	77.82	84.23
1000	2	9.34	79.52	87.22
400	3	6.41	74.16	86.52
1000	3	12:16	**81.93**	**90.54**
1000	4	15:44	80.86	88.92
1000	12	22:27	79.44	85.74
1000	20	34.13	78.82	85.23

The particular OOB data of each tree in the forest are used for predicting and the results are aggregated over all trees to compute the OOB error. Compared to cross validation the OOB error is unbiased and a good estimate for the generalization error. The OOB error was decreased when increased the number of trees and converges to a threshold (94% for pre event data and 82% for post event data), as shown in Figure.4.3.8. (1000 trees and 4 split variables) and Figure 4.3.9. (1000 trees and 3 split variables).

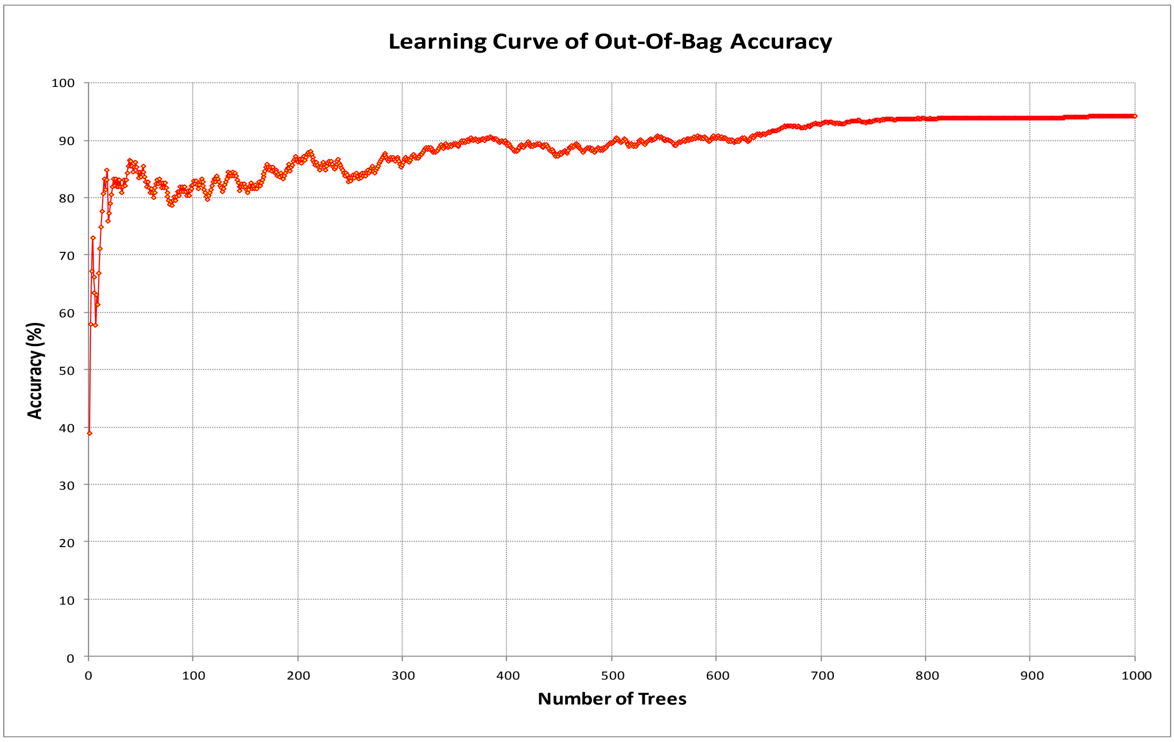

Fig.4.3.8. Learning curve of OOB accuracy pre event training data

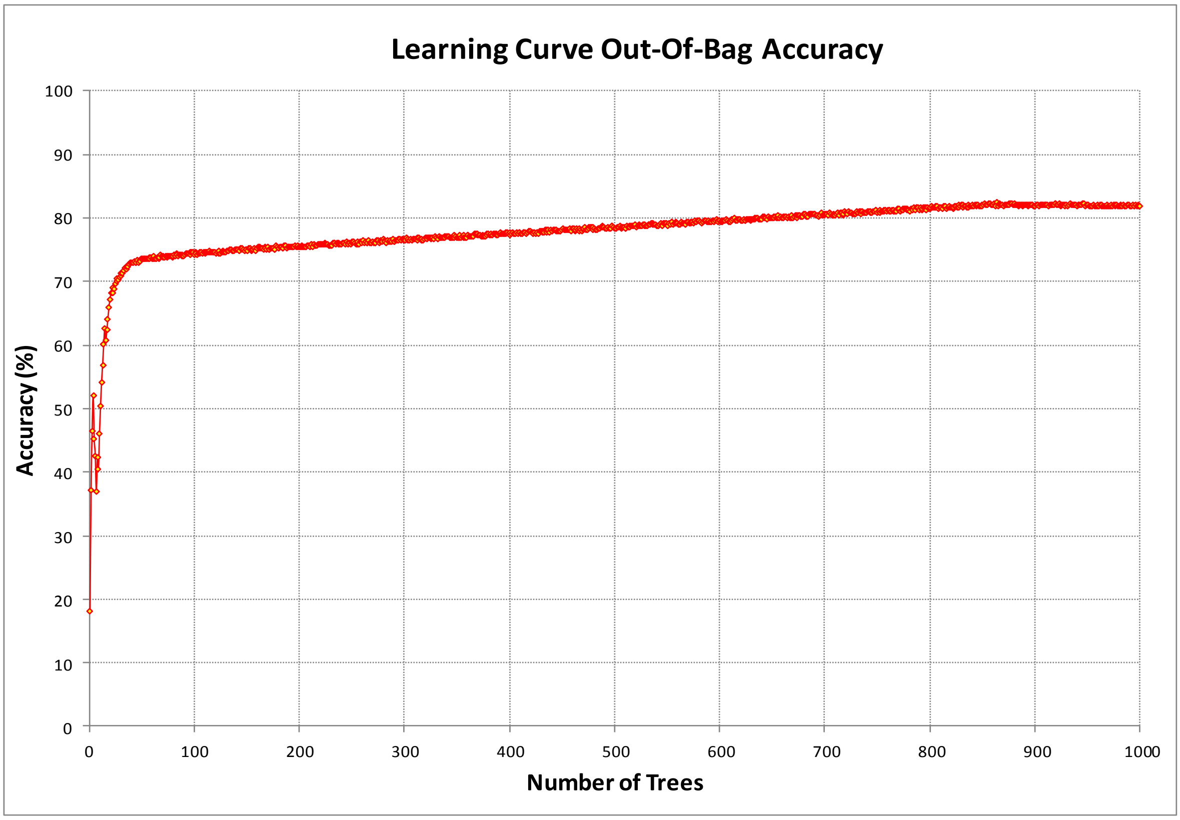

Fig.4.3.9. Learning curve of OOB accuracy post event training data

The variable importance of pre and post event BRR training data can be seen in Figure.4.3.10 and 4.3.7. Each data channel (profile) is represented by one variable. According to these figures, conclusions can be made as, opening 5 and 7 channels from pre and post data are important for the classification process. Also of interest, opening 11, 15 and closing 7, 9 are other important channels for whole classification.

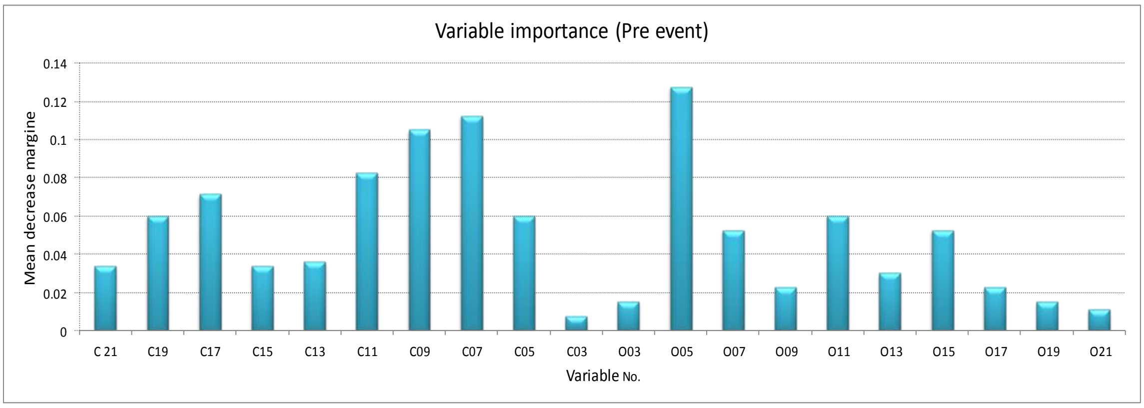

Fig.4.3.10. Variable importance against the 20 variables before the event

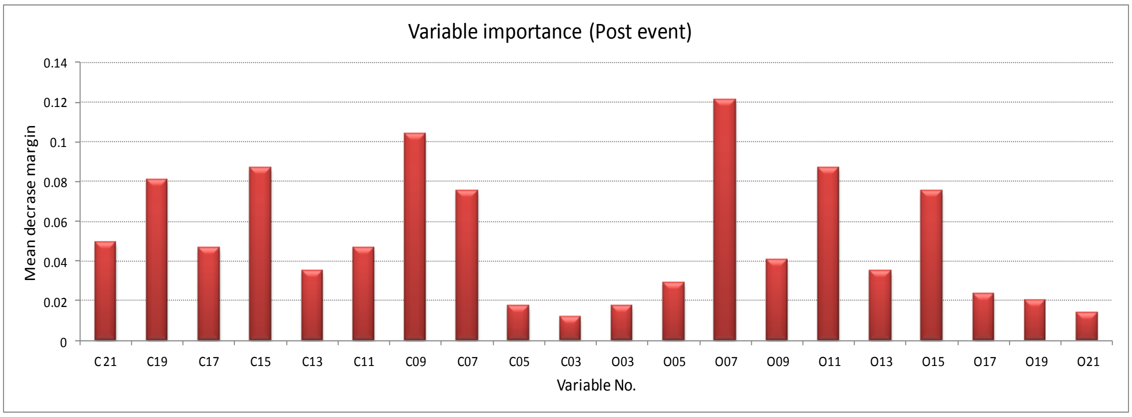

Fig.4.3.11. Variable importance against the 20 variables after the event

The variable importance for individual classes is shown in Figure.4.3.12. It is interesting to note that classification for small size of the building (type 1), opening 7 and closing 9 channels are important while opening 11, 15 are much more effective for large size of the building. Classification with opening 15 and 21 give negative effect for the type 1 building class that might increase the error rate.

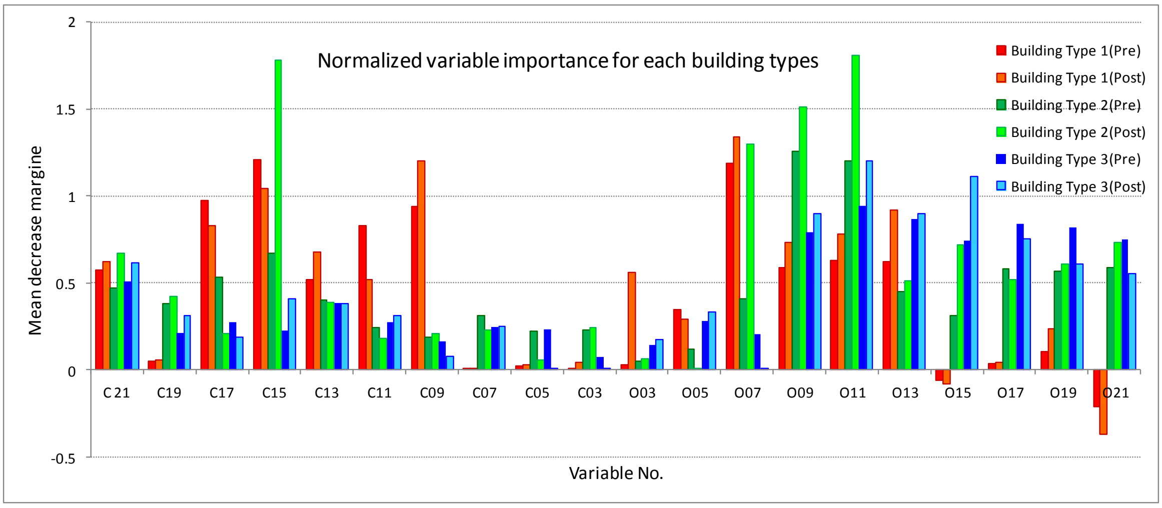

Fig.4.3.12. Normalized variable importance for 20 variables before and after the event

Here in Figure.4.3.13 and 4.3.14 show the building extraction results using Random Forest classifier before and after the earthquake and tsunami in Ishinomaki area. The red, green and blue colors indicate the 3 types of selected building types according to the size and black shows the background.

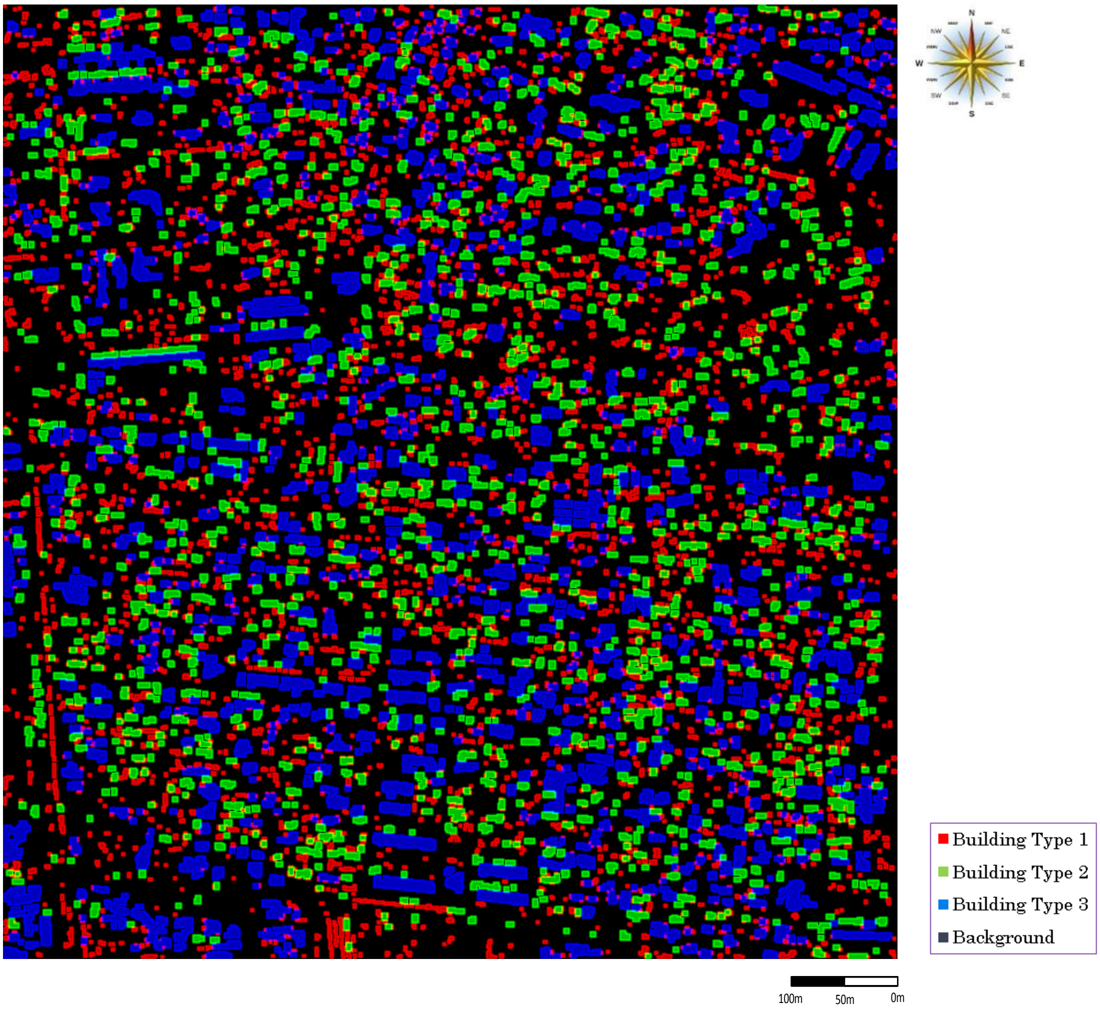

Fig.4.3.13. Building extraction results using RF classifier before the earthquake and tsunami in Ishinomaki area. (The aerial image consists of a 2km × 2km area in Ishinomaki City, Miyagi Prefecture)

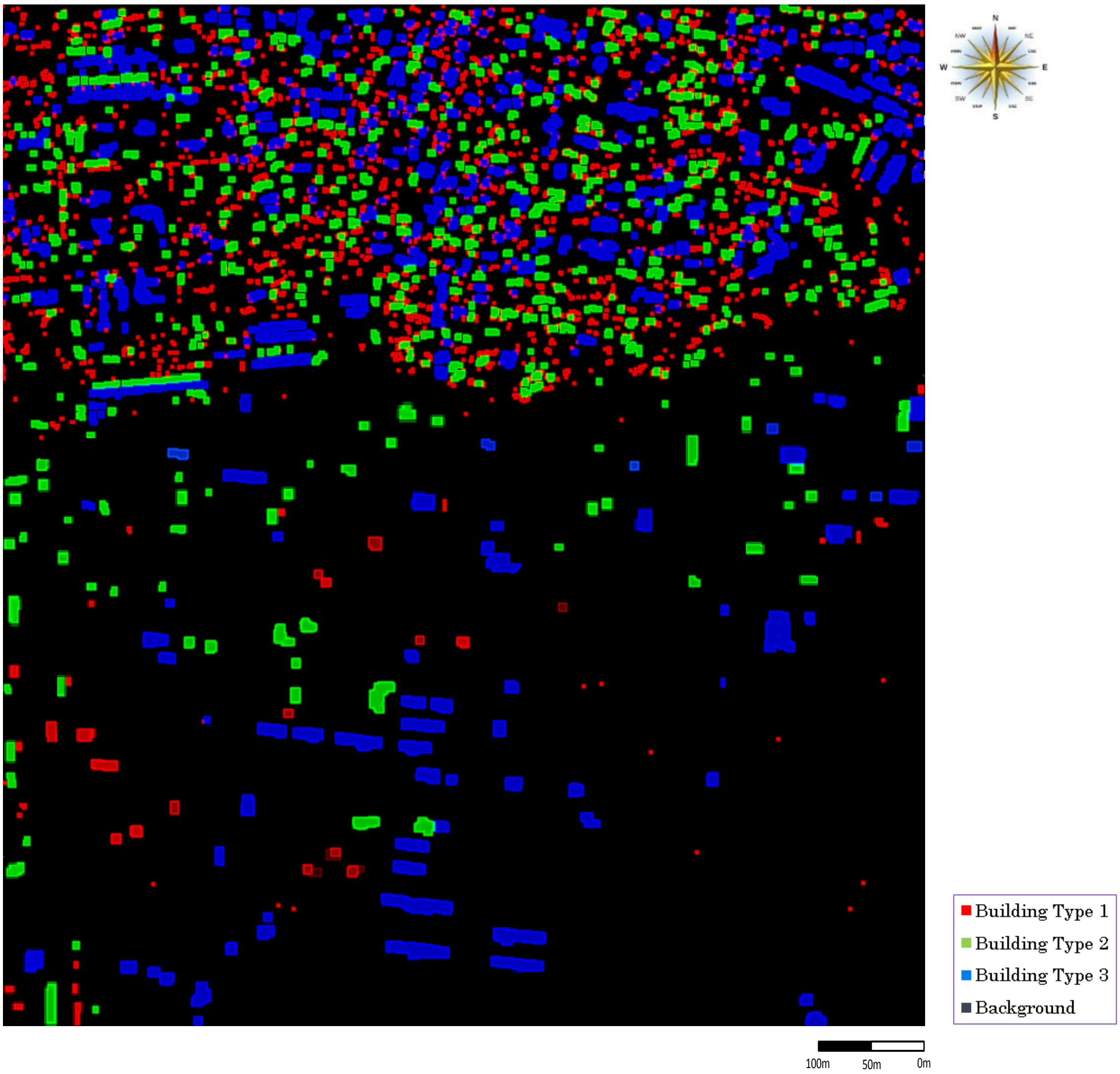

Fig.4.3.14. Building extraction results using RF classifier after before the earthquake and tsunami in Ishinomaki area. (The aerial image consists of a 2km×2km area in Ishinomaki City, Miyagi Prefecture)

4.3.3. Accuracy assessment

There are four types of features (3 type of buildings and Background) that are classified by RF. The obtained classification accuracy statistics of the tested large scale optical data of Ishinomaki tsunami hazardous area are shown in Figure.4.3.15. Considering these results with existing GIS data, it can be seen that 3 kinds of building types and background were classified with high accuracy.

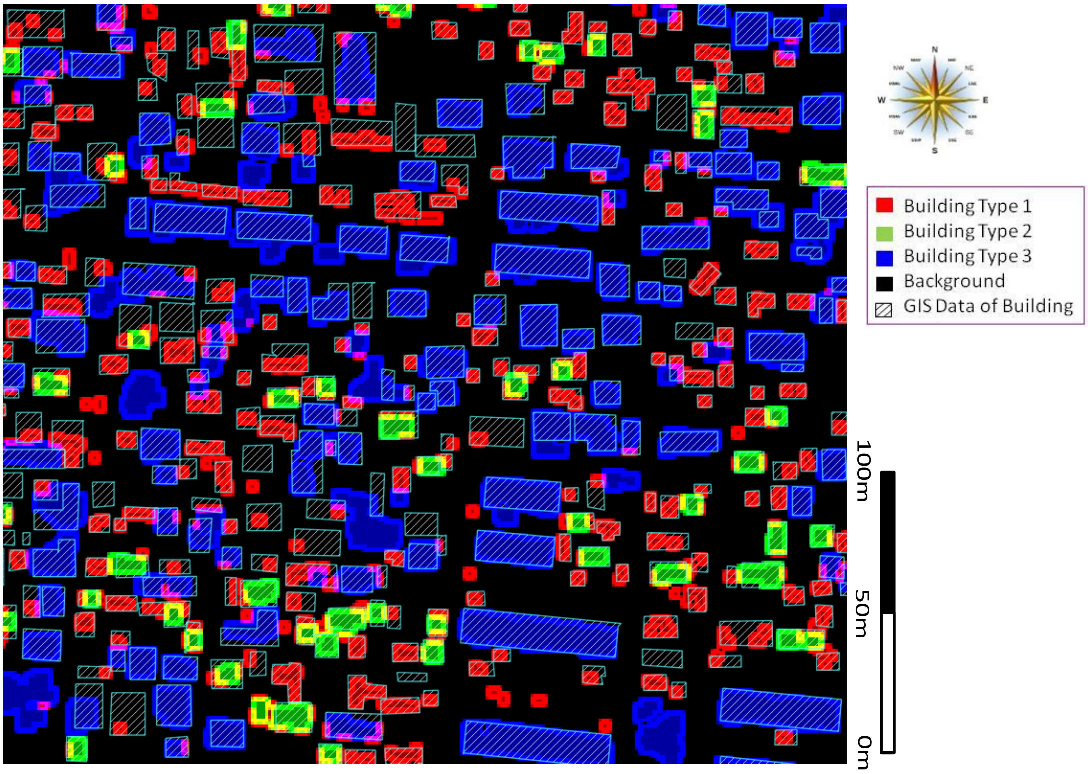

(a) Result of building identification overlaying GIS data before the event

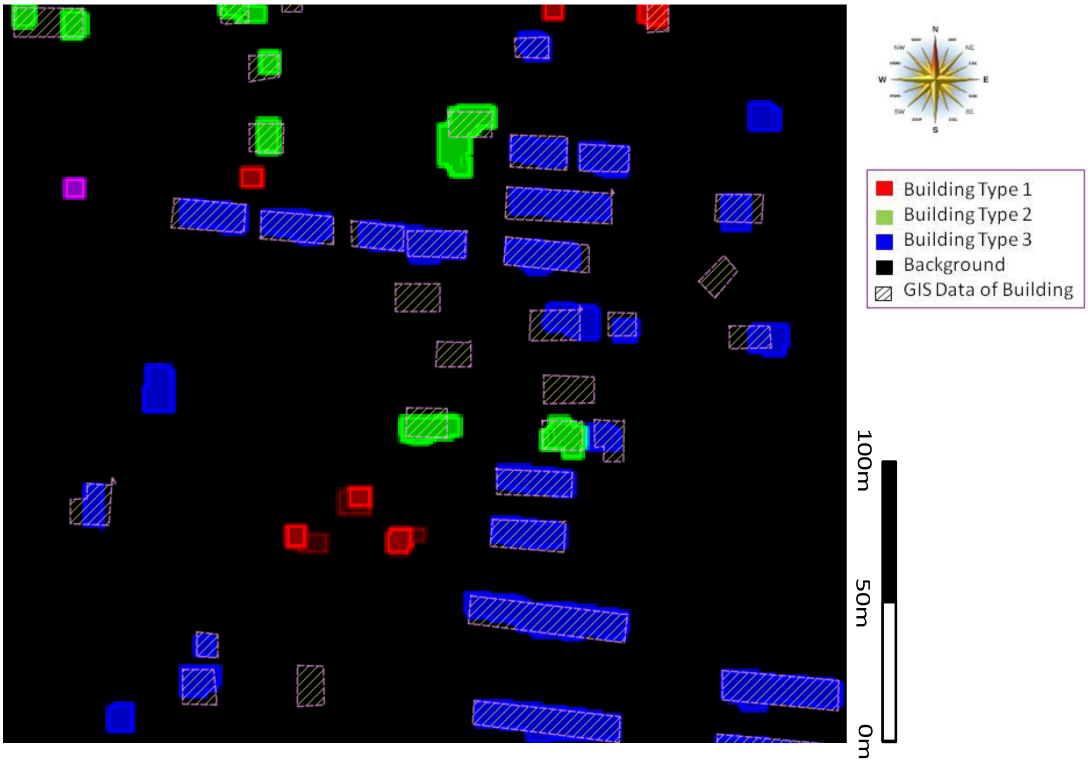

(b) Results of building identification overlaying GIS data after the event

Fig.4.3.15. Accuracy assessment of damage building results using GIS data (white diagonal polygons). Here the red, green color shows the 3 types of building and background in black.

Therefore, using DMP vector features as texture features are expected to be better explored for rural area classification.

The Table.4.3.4 shows the accuracy assessment done for the damaged building extraction in the applied area. Though out the experiments, the Random Forest classifiers performed well for building extraction. The overall accuracy of the proposed method for damaged building extraction is 88%, while producer accuracy and user accuracy are shown 90.78% and 92.47% for the candidate area of this study.

Table.4.3.4. Confutation matrix for accuracy assessments of damaged building identification

Unit Base Accuracy Assessment (Random Forest)		Damaged Building Extracted Result			
		Damaged or washed away	Survived	Total	Producer Accuracy
Ground Truth Data	Damaged or washed away	1044	106	1150	90.78%
	Survived	85	357	442	88.77%
	Total	1129	463	1592	
	User Accuracy	92.47%	77.11%		88.00%

This result is much improved than among the previous methods. The classification algorithm does not over fit, and it does not require guidance (although its accuracy can be tweaked slightly by altering the number of variables used for a split). Furthermore, the algorithm can estimate the importance of variables for the classification. Such estimation is of value for feature extraction and/or feature weighting in high resolution optical image data classification. The Random Forest classifier should be considered very desirable for multi-spectral (in here the DMP series) classification of remote sensing and geospatial data, where no convenient statistical models are usually available.

To further improve the accuracy, additionally, spatial information should be used to correlate man-made objects with their shadows from the closing profile, e.g. C(7), C(11), C(15) and C(19). The extension and investigation of the proposed techniques on data acquired by other sensors (e.g., LIDAR and SAR images) should also be of interest. In the different time series, the color and size of the building roofs would be changed and newly constructed building was found to have mis-classification errors. It is required to have the actual building footprints to be investigated using the ground truth data.

4.4 Automated High Resolution Optical Image registration using Fast Furrier Transform

4.4.1 Results of Image Registration

This section is dedicated to discuss the results of automated registration of pre and post event high resolution (airborne or space borne) images using fast Fourier transform. For further details regarding the methodology refer section 3.5.2. (Chapter 3). Figure.4.4.1 shows the pre and post event unregistered VHR airborne imagery in the same corresponding area.

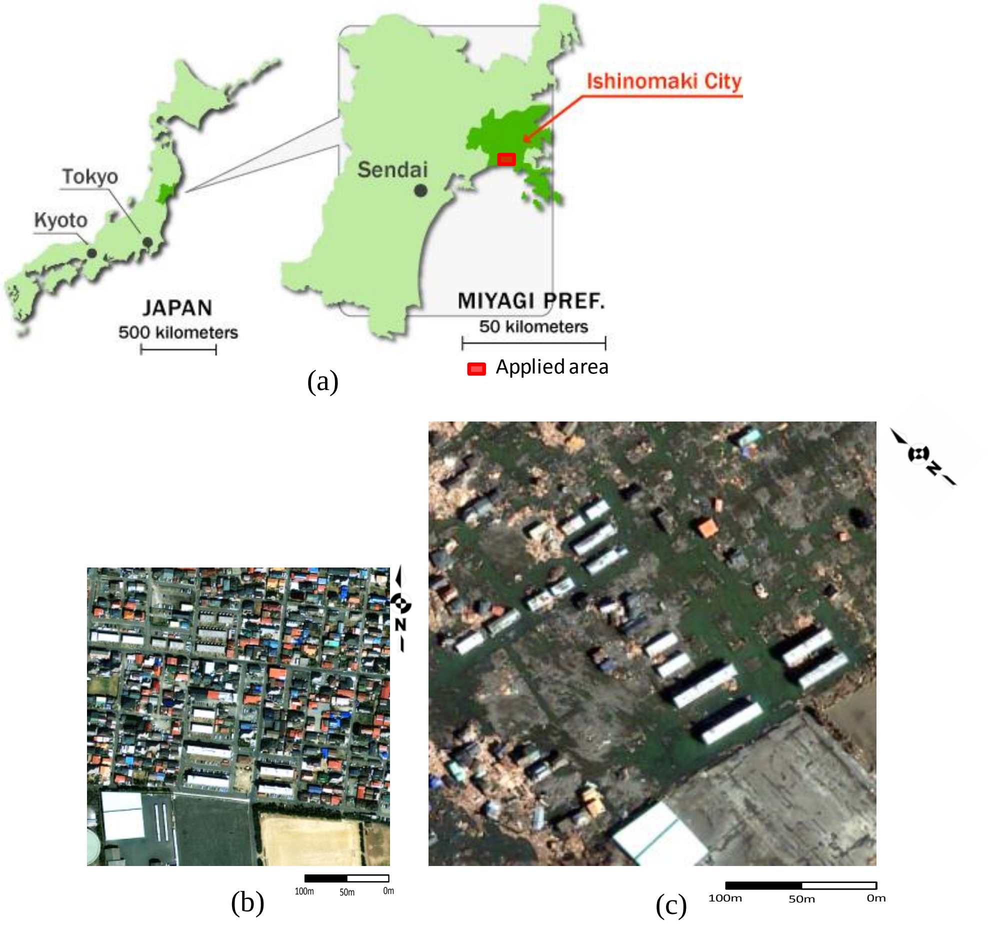

(a)

(b)

(c)

Fig.4.4.1. (a) Applied area, (b) before the Tsunami Hazard Ishinomaki area and (c) after the tsunami hazard.

Figure.4.4.2 shows the image registration of pre and post tsunami aerial images using the proposed phase correlation method and it has detected the correspondence area without error.

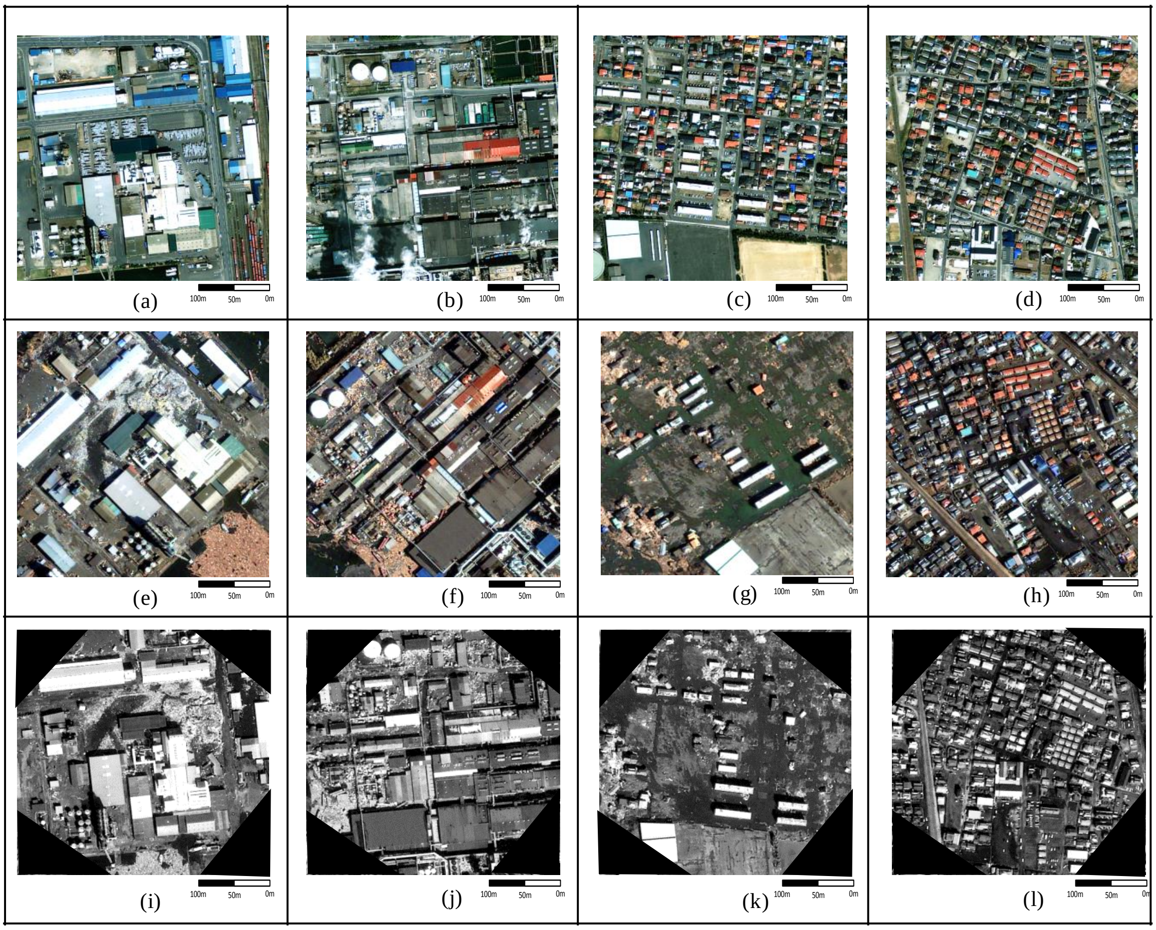

Fig.4.4.2. (a, b, c, d) Pre tsunami Images of Ishinomaki area, (e, f, g, h) Post Tsunami images of the same area and (i, j, k, l) shows registered post-tsunami imagery using the automated proposed method. Here (a) and (b) are show subset images of large scale building compounds and (c) and (d) show complex urban areas which heavily damaged and low damaged.

Table.4.4.1. Accuracy of image registration results.

	True	False	Accuracy
Rotation	152	28	84.44%
Scale	152	28	84.44%
Translation	145	35	80.56%

The Table.4.4.1 shows the accuracy of the tested results of 180 samples. Image registered correctly for rotation and scale variance 152 samples out of them and 145 samples for translation (shift).

4.4.2. Results of Identifying Damaged Building.

The experimental results of damaged area identification using FFT power spectrum base analysis that explained in section 3.5.3 (in chapter 3) are shown in this section. The damaged places were identified using the changes (differ) of the root mean squared among the profile roughness parameter [R_q] and the Waviness height [W_t]standard deviation of the pre event site and the post event site. If the difference of the two values of root mean squared [R_q] is more than 0.0214 and the difference of the two values of Waviness height [W_t] is more than 0.52, the block is identified as a damaged position. Here the Figure.4.4.3 shows the part of results of FFT analysis, i.e. randomly selected points on airborne image and green color subset of 64m × 64m square size show the points that identified as undamaged places and red as damaged.

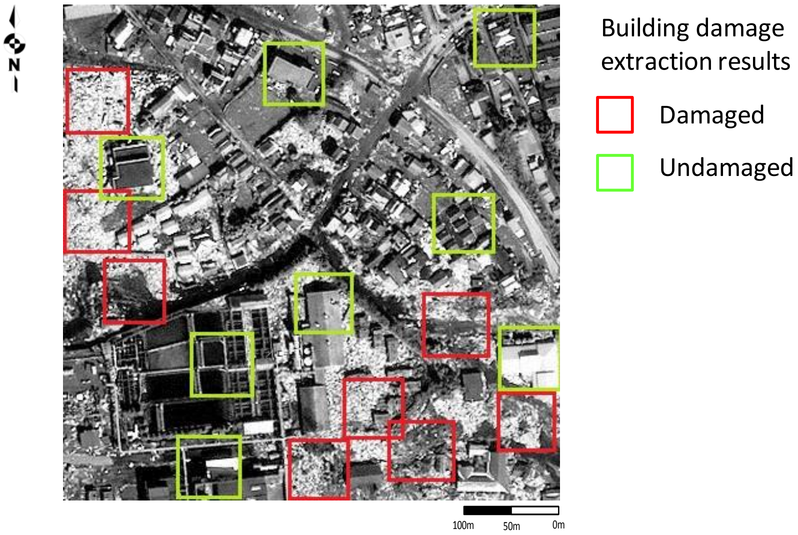

Fig.4.4.3. Randomly selected points on airborne image and damage identification.

The changes of each cross cutting value of power spectrum surface around the r/2 distance from the center of log FFT images of pre and post event were estimated as the method described in section 3.4.3. (Chapter 3). Following the changes of the power spectrum characteristics, it was set empirically to the root mean squared [R_q] value more than 0.0214 Waviness height [W_t]is more than 0.52 for damage identification. The results obtained from this proposed remote sensing method were compared with the 180 samples of ground truth points that randomly selected on the reference tsunami inundate and non-inundated area in Ishinomaki and Minamisanriku area in Miyagi prefecture to quantify the accuracy.

Table.4.4.2. Changes of profile roughness parameter [R_q] for damage identification. (30 out of 180 samples of tsunami inundated hazard area, Ishinomaki, Miyagi Prefecture, Japan,[W_t >0.52]).

Sample No	R_q (Pre event)	R_q (Post event)	Damaged	Sample No	R_q (Pre event)	R_q (Post event)	Damaged	Sample No	R_q (Pre event)	R_q (Post event)	Damaged
1	0.7366	0.6512	YES	11	0.7122	0.6311	YES	21	0.7761	0.6694	YES
2	0.7381	0.7212	NO	12	0.7742	0.7519	NO	22	0.7690	0.6703	YES
3	0.7456	0.6475	YES	13	0.7586	0.6998	NO	23	0.7422	0.6481	YES
4	0.7211	0.6281	YES	14	0.7612	0.6384	YES	24	0.7188	0.6012	YES
5	0.7458	0.7200	NO	15	0.6853	0.6455	NO	25	0.7366	0.6396	YES
6	0.7261	0.6571	NO	16	0.6971	0.6044	YES	26	0.7332	0.6055	YES
7	0.7433	0.6629	NO	17	0.7304	0.7056	NO	27	0.7077	0.6930	NO
8	0.7312	0.6433	YES	18	0.7444	0.7211	NO	28	0.7424	0.7318	NO
9	0.7017	0.6512	NO	19	0.7528	0.6173	YES	29	0.7329	0.7214	NO
10	0.7273	0.7134	YES	20	0.7110	0.7029	NO	30	0.7105	0.6227	YES

Table.4.4.2 shows the building damage identification results conducted by the proposed method. Note that all sample selected that the changes of Waviness height W_t >0.52.

4.4.3 Discussion.

The pre and post event imagery are divided to 64mx64m sub imageries and were applied to two dimensions (2D) Discrete Fast Fourier Transform (DFT) process, which calculate the difference of max-scaled log power spectrum with its vertical frequency to identify damaged building due to the natural hazard using the proposed method. The areas of damaged and undamaged building were identified by using their different spectral effectiveness value over 2D FFT. The airborne Very High Resolution (VHR) imagery consisting of pre and post 2011 Pacific coast Tohoku earthquake and tsunami site of the Ishinomaki area in Miyagi Prefecture, Japan was used for this study.

As an early step, before the damage building detection this section shows the image registration results. The pre and post event optical images of hazardous area were automatically registered using Fast Fourier Transform. Pre-generated gray level airborne images of pre and post event site were applied to FFT based approach. The results show the image registration of pre and post images with different scaled, rotated and shifted, even it changed due to the hazard. However, this algorithm requires images overlapping area more than 30% and scale changes less than 1.8 respectively. The Figure.4.4.4 shows the investigated ground truth survey in candidate area.

(a) (b)

(c) (d)

(e) (f)

Fig.4.4.4. Ground truth survey in Ishinomaki and Minamisanriku area, Miyagi Prefecture. *(Continue)*

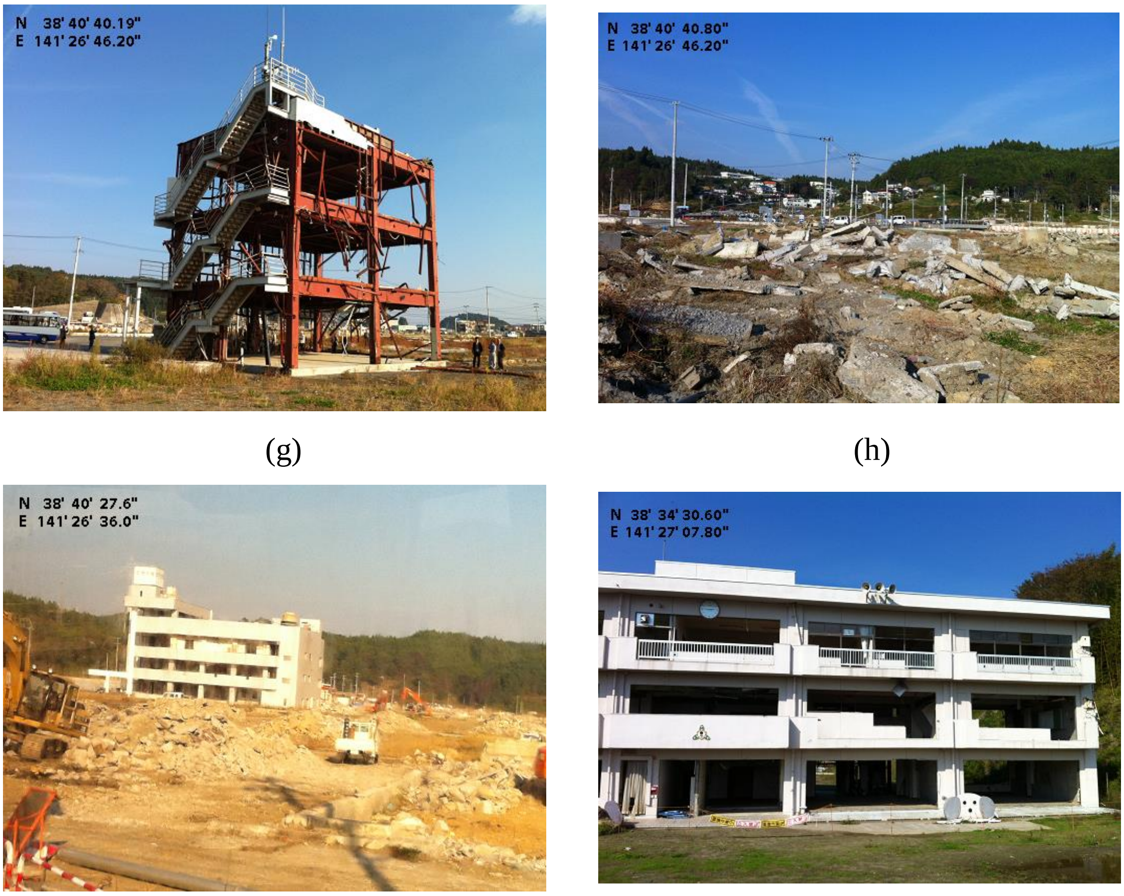

(g) (h)

(i) (j)

Fig.4.4.4. Ground truth survey in Ishinomaki and Minamisanriku area, Miyagi prefecture.(*Continued*)

Here the Figure.4.4.5 shows FFT based results on ground truth data and Table. 4.4.3 shows the accuracy assessments of damaged building using error metrics. The overall accuracy the FFT based proposed method that used spectral information of the image is much lower than the morphological operator based methods that used the spatial information. However, these results to be used to increase the accuracy of previous works in next step as auxiliary data.

The images that obtained from IFFT pre and post hazard data can provide significant information about the location and quantity of damage on buildings of tsunami inundated damage areas. This proposed method easily determined most of the collapsed or washed away building due to the Tsunami. Most of the cases of natural hazards, airborne imageries of the region are not available and available data also with different scale, rotation and shifted imagery that obtained pre and post disaster have to be used. Therefore, it is important to process the available data set rapidly and accurately and this research proposed an approach to fulfill this aim. Some building confronted the tsunami, had serious damages to their walls or the lower part of the structure while being washed away, but the roof stayed infect.

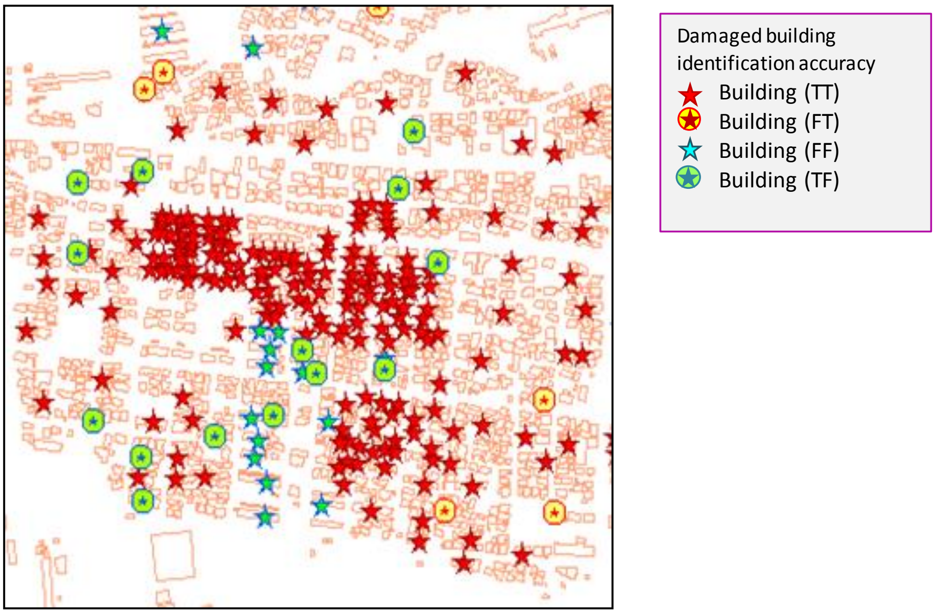

Fig.4.4.5. FFT based results on ground truth data. Here the blue and red color stars show correctly identified undamaged and damaged building, while round with triangles show miss-identified undamaged and damaged building.

Table. 4.4.3. Accuracy assessments FFT based method using error metrics.

Unit Base Accuracy Assessment (FFT)		Damaged Building Extracted Result			
		Damaged or washed away	Survived	Total	Producer Accuracy
Ground Truth Data	Damaged or washed away	863	287	1150	75.04%
	Survived	186	256	442	57.92%
	Total	1049	543	1592	
	User Accuracy	82.27%	47.15%		70.29%

These buildings were identified as undamaged (Refer Figure. 4.5.2.(i) and (j)). This should be identified using another methodology. The results illustrated that the proposed method can be successfully used to identify tsunami inundate damage areas automatically. The maximum scale power spectrum of undamaged building areas shows high values of standard deviation compare with damaged building.

The images that obtained from IFFT pre and post hazard data can provide significant information about the location and quantity of damage on buildings of tsunami inundated damage areas. This proposed method easily determined most of the collapsed or washed away building due to the Tsunami. In most of the cases, airborne imagery of the region is not available and if available it will be in a different Scale, Rotation and shifted imagery that obtained pre and post disaster have to be used. This study was mainly conducted using the freely available data. But care has been taken to account for their different scale, rotation and shifting effects. This mainly reduces the cost of the needed data. Considering the ground condition after the disaster with heavily damaged, this accuracy values are reasonable.

4.5. Combination of Morphological Operators and FFT methods

This concluding section shows the results of the two approaches of morphological and FFT methods. Figure.4.5.1 demonstrates flow of the combined work of morphological and FFT based method that applied to the Ishinomaki, earthquake and tsunami hazard area. The Random Forest classification based method that provided high accuracy among other methods was used as the morphological based approach (Refer Section 4.3). The Same candidate area that applied to the FFT based method in Chapter 3 (Refer Section 3.5.2) was used as another method. The accuracy assessment of this approach was conducted using a field survey and existing GIS data. Figure.4.4.4 (b) and (c) shows part of the data validation of selected samples, of the result of the building extraction over the Ishinomaki area using proposed method. (Refer Section 4.3.3).

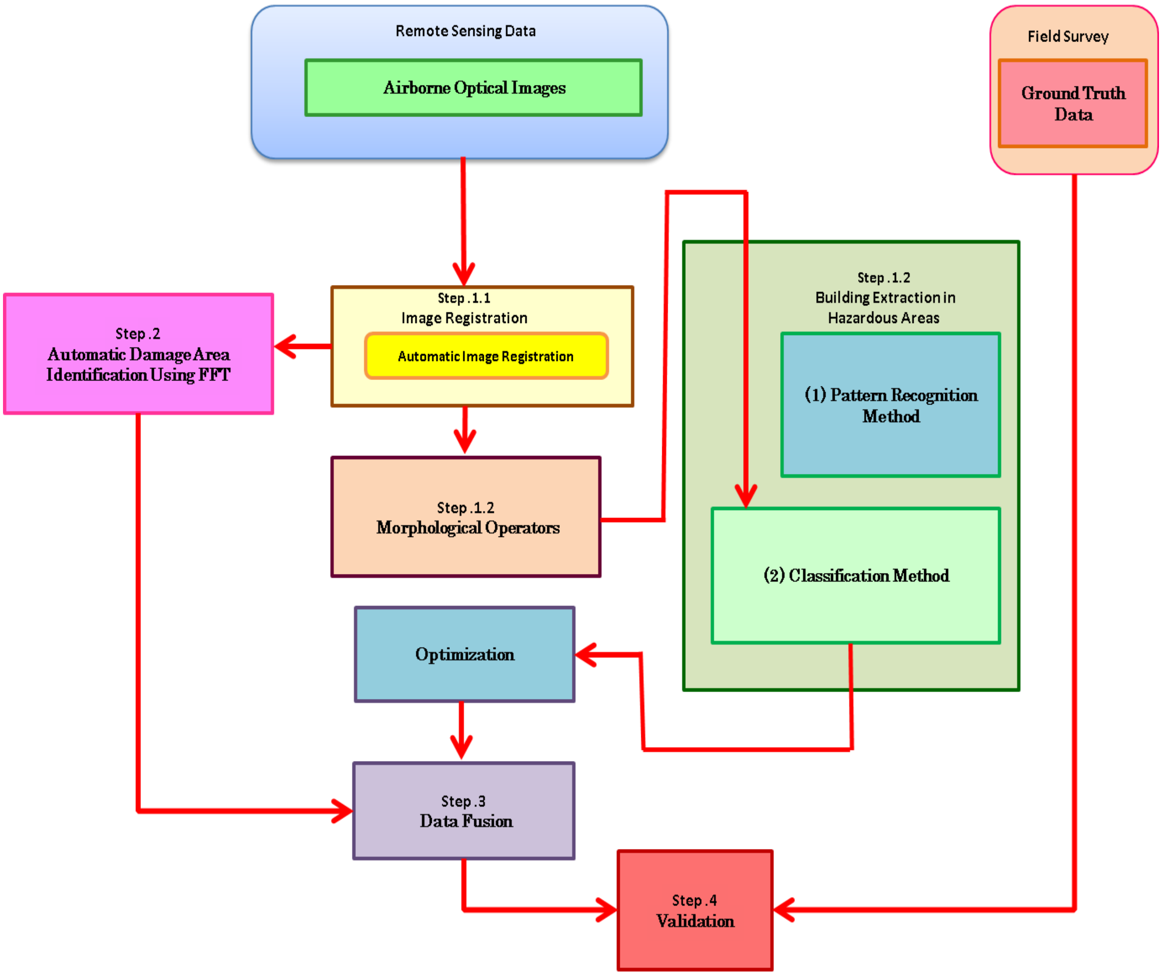

Fig.4.5.1. Damaged building extraction process combining of the morphological based and FFT based approaches.

Figure.4.5.2. Damaged building extraction process combining of the morphological based and FFT based approaches. (Region level and unit level)

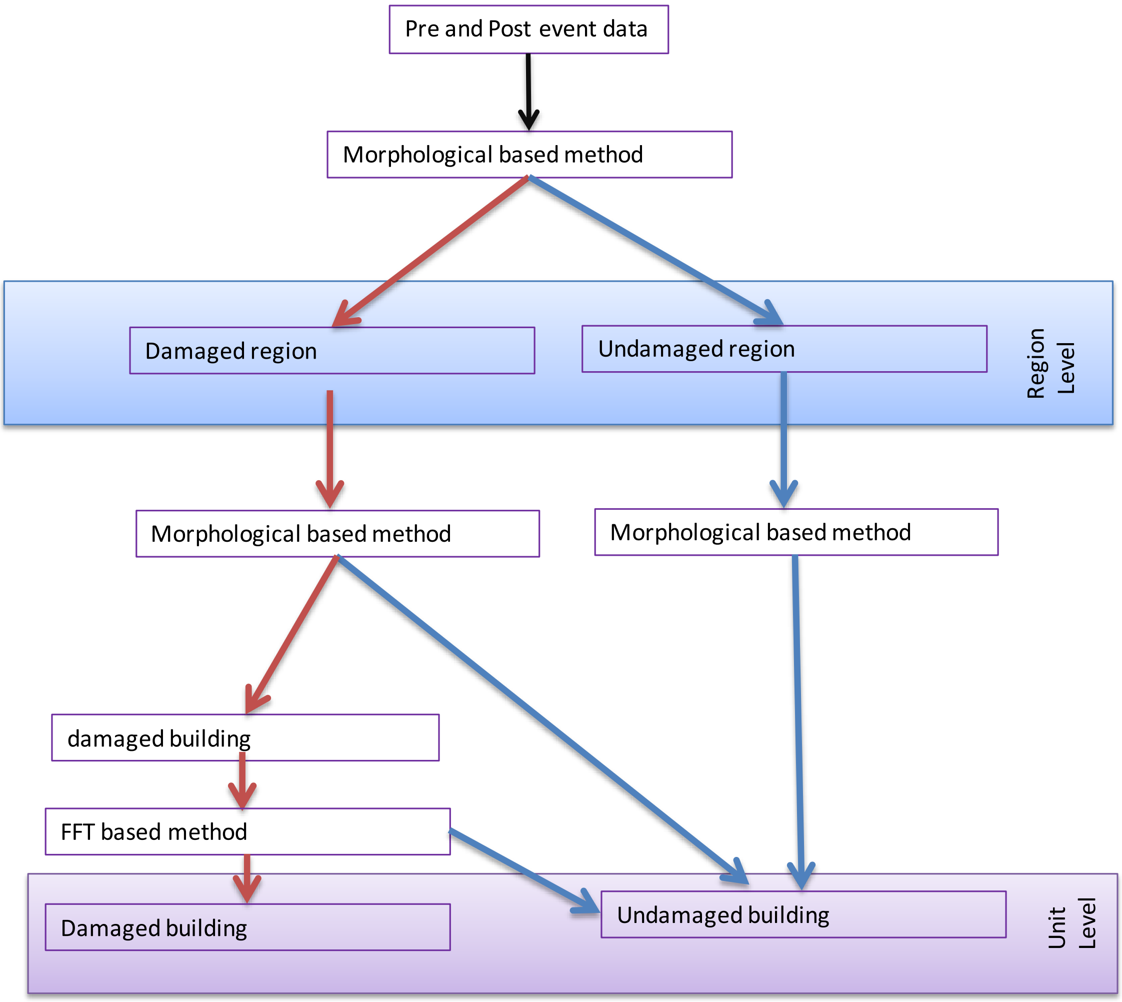

Fig.4.5.2. Damaged building extraction process combining of the morphological based and FFT based approaches. (Region level and unit level)

Combining both results of this methodology produced a significantly high accuracy with the probability map of damaged building that was generated as shown in Figure.4.5.3. Here the green color to red color represents the building damage from low level to high level respectively.

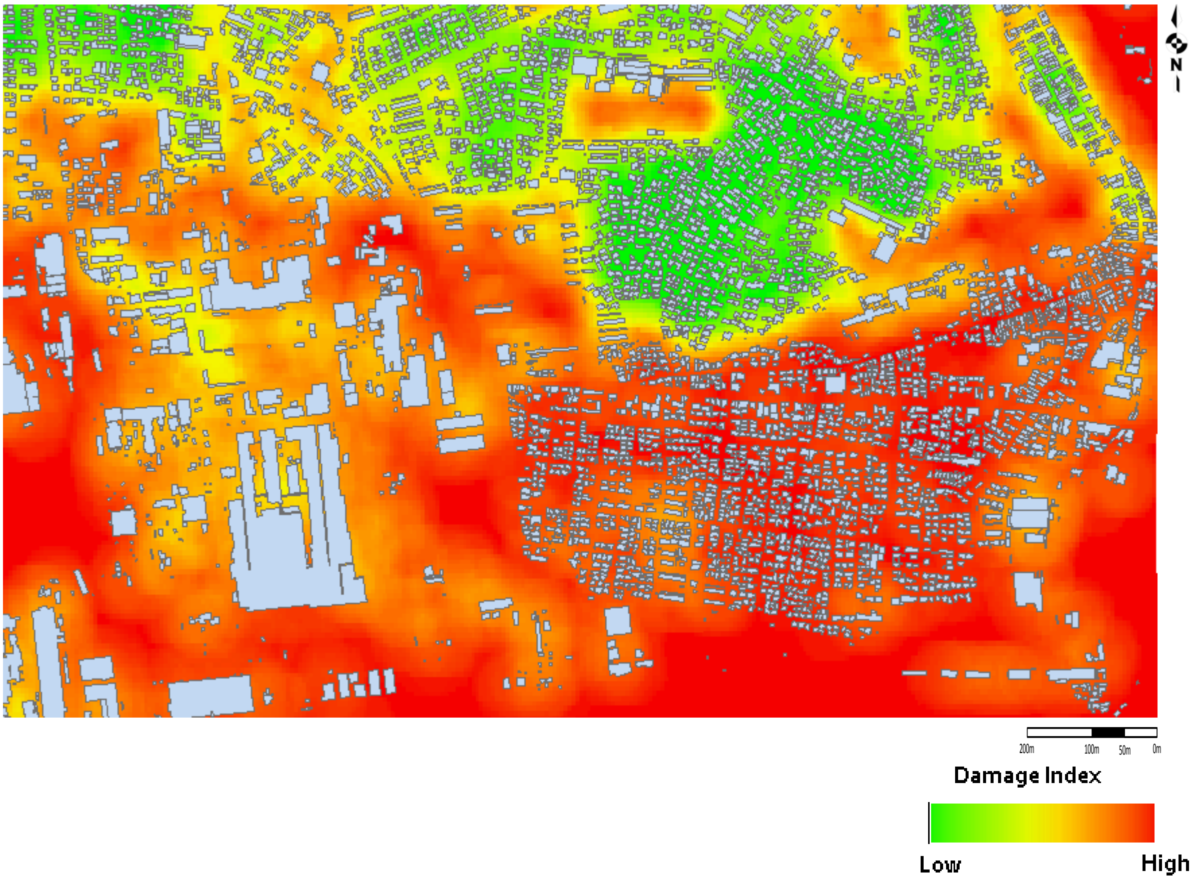

Fig.4.5.3. Combination of Morphological approach and FFT based approach.

Table.4.5.1. Accuracy assessment of the combination morphological and FFT based methods using error metrics.

Unit Base Accuracy Assessment (RF&FFT)		Damaged Building Extracted Result			
		Damaged or washed away	Survived	Total	Producer Accuracy
Ground Truth Data	Damaged or washed away	1098	52	1150	95.48%
	Survived	30	412	442	93.21%
	Total	1128	464	1592	
	User Accuracy	97.34%	88.79%		94.85%

Accuracy assessment of above approach was conducted using a field survey and GIS data (see Table.4.5.1). We found that few errors of existing GIS data while investigating the area conducting in a field survey. Any of the methods identified a building as a damaged; we supposed it as a damage building.

The building that washed away or collapsed in the applied area are identified as 1150 according to field survey and exist GIS data as ground truth and the result of the algorithm above correctly provide 1098 buildings respectively. Thus, the proposed method has proven and considered to be useful in building damage detection with high accuracy even in emergency response following natural disasters.

CHAPTER 5

CONCLUSION

This chapter presents the general conclusions of the study describing and reviewing the main contributions of this work. Specific concluding remarks on the research tropics treated in the dissertation are also given. Finally, perspectives on possible future developments of the work are presented. Based on the following observations general conclusions are made and forwarded here.

1) The main objective of this study is to propose a method for building extraction of urban areas in an event of a natural hazard using optical imagery that can be used for damage identification, assessment, quick and long term response. In other words, damaged building detection is a key element in the post event (natural hazard) crisis assessment and response procedures. All of our study was focused to reach an automated method for rapid and high accurate detection and quantification of the damaged building from VHR (Very High Resolution) space borne (IKONOS, Quick Bird, Geo-Eye) or airborne optical imagery of urban regions.

2) According to the previous research work in the thesis outlines several existing building extraction methods. The challenges faced in each of these techniques and how they addressed the complexities of the urban spatial structure is discussed.

3) The DMP proved to be an effective tool for building extraction of VHR remote sensing images because it is defined as a derivative composition of opening and closing with reconstruction transformations. Operators by reconstruction permit to filter the image by entirely preserving the geometry of those building structures that are not erased from the scene and the size of the building are segmented well with the DMP decomposition process. The definition of the extended derivative of the morphological profile for panchromatic and multispectral images was presented. (Refer Reference [1], [2], [3] and [4]).

4) The presented DMP method considered the different notation of connectivity for building roof extraction. The proposed techniques identified that conventional 7m, 11m, 15m geometric resolution SE out of 3 to 21 opening and closing connectivity were well performed for building roof identification. (Refer Reference [5] [6] [7] [8] 9] and [10]).

5) We addressed the outcomes of the extended morphological pattern recognitions (template matching) technique with binary image for building extraction in Section 4.2. Equipped with this operator, we discuss several template matching scenarios,

considering the SET sizes and shapes. We demonstrate the results with relevance of our proposition by several SET size and shape with different morphological profile cases of pre and post tsunami hazard remote sensing images. Refer Reference [11], [12]. Indeed, the method is useful for binary document image pattern matching tasks. We have shown the results of the experiment of pattern matching for building roofs, to illustrate the effects of FG and BG blur, and of regular sub-samplings of the templates. Proposed combinations of building roofs reflectance value and shape increased the probability of building extraction. However, the candidate area contained various kinds of roofs with different color, shape and size. There were some building structures that are complex, hence these sometimes combine together to be classified as a one building. Moreover, it is important to facilitate the process of template designing by introducing a way to interactively learn the structuring elements to be involved in the template matching process in different hazardous areas.

6) The Random Forests classification method was investigated for classification of pre and post-earthquake and tsunami event remote sensing airborne image data set, which is both a challenging and important classification problem in building extraction discussed in Section 3.3, 3.4, 4.3 and 4.4. In experiments, the Random Forest classifiers performed well for building extraction (even than SVM). The Random Forest algorithm does not over fit, and it does not require guidance (although its accuracy can be tweaked slightly by altering the number of variables used for a split). Furthermore, the algorithm can estimate the importance of variables for the classification. Such estimation is of value for feature extraction and/or feature weighting in high resolution optical image data classification. The Random Forest algorithm can also detect outliers, which can be very useful when some of the cases may be mislabeled. With this combination of efficiency and accuracy, along with very useful analytical tools, the Random Forest classifier should be considered very desirable for multi-spectral (the DMP series) classification of remote sensing and geospatial data, where no convenient statistical models are usually available. (Refer Reference [13], [14] and [15]).

7) Another novelty of the work to identifying damaged building using their shape and low spectral effectiveness over 2D FFT power spectrum was also highlighted in the study. The work proposed is an integration of FFT and level slicing to accurately identify the location of the damaged areas caused by a Tsunami while it helps to increase damage identifying accuracy combing with morphological approach. This work has been

developed parallel but separate with the morphological operation building extraction process. (Refer Reference [16]).

The combination of both these methods produced significantly high accurate results and damaged maps were generated (Refer Section 4.6). The proposed method tested several different kinds of areas, damages and images. Finally the optimized results were validated with ground truth survey and existing GIS data for accuracy assessment. The whole of the study is based on freely available and downloadable data consist of different scale, rotation and shifted imagery that obtained pre and post disaster had to be used due to the budget restrictions. Considering the ground condition of the candidate heavily damaged areas that used for the study, this accuracy values is reasonable. On the basis of the study, the analysis and the experiments carried out in the framework of this thesis, we identified some interesting directions of research. We suggest developing this process further.

- The investigation and extensions of the proposed techniques on data acquired by other sensors (LIDAR, Ultra High Resolution SAR, and DEM images) should also be of interest. If higher accuracy value is desired for optical images, auxiliary additional data should be needed. Indeed, very few applications of mathematical morphology techniques on other data than optical images exist.

- Another interesting direction would be to extend the presented techniques by considering different notation of connectivity in different range. The proposed techniques are based on the conventional 3 to 21 SEs connectivity for building roof identification.

- For pattern matching technique using extended mathematical morphology, in some cases, clear condition between foreground and background spectral value, shape and size is not so easy to correctly obtain, thus preventing us from relying on such a rotating and ordering strategy. Further works will be included the operators robustness against noise, which can be improved by using fuzzy and rotating structuring elements over the image.

- Since the different time series, the color and size of the building roofs would be changed and newly constructed building gave mis-classification error. The actual building footprint should be investigated using GIS data.

- More accurate extended FFT based method for automated image registration in hazardous areas and investigate seismic displacements is also interested.

Reference

1. Chandana Dinesh Parape, Masayuki Tamura, U. Abdul Bari, P.G. Ranjith Dissanayake, Detecting and assessment of tsunami building damage using high-resolution satellite images with GIS data, International Journal of Disaster Resilience in the Built Environment. Emerald. ISSN 1759-5908, Issue 4.2,2013.

2. Chandana Dinesh Parape, Chinthaka Halpage, Masayuki Tamura, Abdul Bari, Ranjith Disanayake, Duminda Welikanna, Shengye Jin , Masami Sugiura, Building Damage and Business Continuity Management in an Event of Natural Hazard – Case study in year 2004 Tsunami, SRI LANKA, International Journal of Sustainability, ISSN 2071-1050. 2013, *5*(2), 456-477; doi:10.3390/su5020456

3. U. Abdul Bari, Chandana Dinesh Parape, Masayuki Tamura, P.G. Ranjith Dissanayake, Assessment of Tsunami Damaged Buildings Using High- Resolution Satellite Images, GIS and GPS Data", IESL Annual Session 2013.

4. Chandana Dinesh Kumara, Masayuki Tamura, Identify Damaged Buildings from High-Resolution Satellite Imagery in Hazard Area Using Morphological Operators- In case of Sichuan earthquake, China, proceeding in ICSBE -International Conference on Sustainable Built Environment, Kandy, Sri Lanka 2010.12.12-14.

5. Chandana Dinesh Kumara, Masayuki Tamura, Identifying Damaged Buildings from High-Resolution Satellite Imagery in Seismic Hazard Area Using Morphological Operators, proceeding in ICIAfS 10 - 5th International Conference on Information and Automation for Sustainability, Colombo, Sri Lanka , 2010.12.17-19.

6. Chandana Dinesh Kumara, Masayuki Tamura, Extraction and Assessment of Buildings Damages from High-Resolution Satellite Imagery, 第20回生研フォーラム「広域の環境・災害リスク情報の収集と利用フォーラム」,proceeding in International Center for Urban Safety Engineering (ICUS), 2011.03.17-18.

7. Chandana Dinesh Kumara, Masayuki Tamura, Identify Damaged Building from High-Resolution Satellite Imagery in Hazardous Areas using Morphological Operators and ISODATA Unsupervised Classification Method, proceeding in 34th International Symposium on Remote Sensing of Environment, Sydney Convention and Exhibition Centre, Sydney, Australia, 2011.04.19-18.

8. Chandana Dinesh Kumara, Masayuki Tamura, Change Detection from High-Resolution Satellite Imagery in Hazardous Areas using Extended Morphological Operators, proceeding in ISPRS Hannover Workshop 2011: High Resolution Earth Imaging for Geospatial Information, June 14-17, Hannover, Germany.

9. U. Abdul Bari, Chandana Dinesh Parape, Masayuki Tamura, P.G. Ranjith Dissanayake, Tsunami Damaged Buildings Assessment Using Satellite Imagery, GIS & GPS Data, International Conference on Building Resilience , proceeding in Interdisciplinary approaches to disaster risk reduction and the development of sustainable communities", Kandalama, Sri Lanka, 2011.7.20-22.

10. Chandana Dinesh Parape, Masayuki Tamura, Identifying Damaged Building from High-Resolution Satellite Imagery in Hazardous Area using Extended Morphological Operators and SVM Classification Method, proceeding in IGARSS-2011 , Vancouver, Canada, 2011 July 22- August 3.
11. Chandana Dinesh Parape, Chinthaka Premachandra, Masayuki Tamura, Masami Sugiura, Morphological Hit-Or-Miss Transform Based Approach for Building Damage Estimation from VHR Airborne Imagery in 2011 Pacific Coast of Tohoku Earthquake and Tsunami , International Archives of Photogrammetry, Remote Sensing and Spatial Information Sciences, Volume XXX-B3, 2012. pp.509-512.
12. Chandana Dinesh Parape, Chinthaka Premachandra, Masayuki Tamura, Masami Sugiura, Extended Morphological Based Approach Combination with and Hit-Or-Miss Transform for Building Damage Estimation from VHR Airborne Imagery in 2011 Pacific Coast of Tohoku Earthquake and Tsunami", proceeding in ISPRS Congress 2012, Melbourne , Australia, 2012.8.25-9.1. 13.
13. Chandana Dinesh Parape, Masayuki Tamura, Mathematical Morphology Based Approach for Building Damage Estimation from VHR airborne Imagery of Ishinomaki Area in 2011 Pacific Coast of Tohoku Earthquake and Tsunami. Proceeding in FIG working week 2012, International Federation of Surveyors, Rome, Italy, May 6-10, 2012.
14. Chandana Dinesh Parape, Chinthaka Premachandra, Masayuki Tamura, Masami Sugiura , Damaged Building Identifying from VHR Satellite Imagery using Morphological Operates in 2011 Pacific Coast of Tohoku Earthquake and Tsunami, proceeding in IGARSS-2012, Munich, Germany, 2012.7.22-27 .p.p.79.
15. Chandana Dinesh Parape, Chinthaka Premachandra, Masayuki Tamura, Masami Sugiura, Automated Identification of Tsunami Induct Damaged Buildings From Airborne Imagery Using Extended Morphological Transformations, proceeding in International Conference on Disaster Management 2012(IIIRR), Kagoshima, Japan, August 24 - 26, 2012.
16. Chandana Dinesh Parape, Masayuki Tamura, Automatic Damaged Building Detection Using Fast Fourier Transform from Close Range Optical Imagery in Case of Natural Hazards, proceeding in ISPRS Congress 2012, Melbourne , Australia, 2012.8.25-9.1.

APPENDIX

a. Support Vector Machine Classification Method

Support vector machine (SVM) is a supervised non-parametric statistical learning technique, therefore there is no assumption made on the underlying data distribution. In its original formulation [1] the method is presented with a set of labeled data instances and the SVM training algorithm aims to find a hyperplane that separates the dataset into a discrete predefined number of classes in a fashion consistent with the training examples. The term optimal separation hyperplane is used to refer to the decision boundary that minimizes misclassifications, obtained in the training step. Learning refers to the iterative process of finding a classifier with optimal decision boundary to separate the training patterns and then to separate simulation data under the same configurations [2]. The implementation of a linear SVM assumes that the multi-spectral feature data are linearly separable in the input space. In practice, data points of different class memberships (clusters) overlap one another. This makes linear separability difficult as the basic linear decision boundaries are often not sufficient to classify patterns with high accuracy. Techniques and workarounds such as the soft margin method [3] and the kernel trick are used to solve the inseparability problem by introducing additional variables (called slack variables) in SVM optimization and mapping (using a suitable mathematical function) the non-linear correlations into a higher (Euclidean or the Hilbert) space, respectively. A kernel function typically needs to fulfill Mercer's Theorem in order to be a valid kernel in SVMs [4]. The choice of a kernel function often has a bearing on the results of analysis. Furthermore, typical remote sensing problems usually involve identification of multiple classes (more than two). Adjustments are made to the simple SVM binary classifier to operate as a multi-class classifier using methods such as one-against-all, one-against-others, and directed acyclic graph [5].

SVMs are particularly appealing in the remote sensing field due to their ability to successfully handle small training data sets, often producing higher classification accuracy than the traditional methods [6]. The underlying principle that benefits SVMs is the learning process that follows what is known as structural risk minimization. Under this scheme, SVMs minimize classification error on unseen data without prior assumptions made on the probability distribution of the data. Statistical techniques such as maximum likelihood estimation usually assume that data distribution is known a priori. Burges [7] in a well-organized SVM tutorial described a simple experiment to illustrate an advantage of SVMs in an image recognition problem. In that demonstration, the performance of a basic multi-way SVM-based recognizer was assessed on image classification in the presence of prior knowledge. The accuracy turned out to be approximately the same if the pixels were first shuffled, with each image instance suffering the same random permutation. Yet, when the act of 'vandalism' (or removal of prior knowledge) took place, SVM still outperformed even the best neural networks. This discovery is particularly appealing in remote sensing applications since data acquired from remotely sensed imagery usually have unknown distributions, and methods such as Maximum Likelihood Estimation (MLE) that assume a multivariate normal data model do not necessarily match that assumption. Even if the data, whose dimensionality is assumed to match the number of spectral bands, were normally distributed, the assumption that the distribution can be described using a bell-shaped (Gaussian) function ceases to be sound, since the concentration of data in higher dimensional space tends to be in the tails [8]. This phenomenon will continue to be encountered in remote sensing as new sensors increase spectral resolution and therefore data dimensionality.

There is also another interesting concept that serves as a key attraction to SVMs. Commonly described by many authors under the notion of over fitting [9], yet variously referred to by others as bias-variance tradeoff [10] or capacity control [11], SVM-based classification has been known to strike the right balance between accuracy attained on a given finite amount of training patterns and the ability to generalize to unseen data.

Alongside the benefits derived from the SVM formulation there are also several challenges. The major setback concerning the applicability of SVMs is the choice of kernels. Although many options are available, some of the kernel functions may not provide optimal SVM configuration for remote sensing applications. Empirical evidence indicates that kernels such as radial basis function and polynomial kernels applied on SVM-based classification of satellite image data produce different results [2]. A good explanation on SVM kernels and their functionality is presented in numerous papers [12]. From the non-expert user point of view, SVM theory is a bit intimidating, particularly due to the fact that the more efficient SVM variants often incorporate some difficult to understand concepts. This limits effective cross-disciplinary applications of SVMs. Numerous SVM tutorials are available [3, 13], but none of these contains an exhaustive discussion on the increasing number of newly proposed variants of SVMs. In the remote sensing field a good starting point would be a textbook by Tso and Mather [14] that provides a review of the entire field of classification methods for remotely sensed data, including SVMs. For those interested in rule extraction from SVMs a recent computer science review is available. Chen and Ho [15] provide an excellent general reference for statistical learning in remote sensing. It should be noted that for this review the term SVM is inclusive of the traditional SVM method as well as SVM-based variants, since most of the latter still heavily rely on the standard SVM method.

In its simplest form, SVMs are linear binary classifiers that assign a given test sample a class from one of the two possible labels. An instance of a data sample to be labeled in the case of remote sensing classification is normally the individual pixel derived from the multi-spectral or hyperspectral image. Such a pixel is represented as a pattern vector, and for each image band, it consists of a set of numerical measurements. Elements of the feature vector may also include other discriminative variable measurements based on pixel spatial relationships such as texture. Figure.a.1 illustrates a simple scenario of a two-class separable classification problem in a two-dimensional input space. An important generalization aspect of SVMs is that frequently not all the available training examples are used in the description and specification of the separating hyperplane. The subsets of points that lie on the margin (called support vectors) are the only ones that define the hyperplane of maximum margin.

$$w \cdot x + b = 0, \forall x \in H_p \qquad (a.1.1)$$

If $x \notin H_p$ Then

$$f(x) = \frac{|w \cdot x + b|}{||w||} \qquad (a.1.2)$$

defines the distance of H_p . In the linearly separable case, such a hyperplane has to satisfy:$a^2 + b^2 =_i c^2$

$$y_i(w \cdot x_i + b) > 1, \forall i \in [1, N] \qquad (a.1.3)$$

One can always choose the vector w after appropriate normalization such that condition (6.3) is satisfied. The optimal hyperplane is the one that maximizes the margin: $2/\,||w||$. This is equivalent to minimizing $||w||/2$ and leads to the following quadratic optimization problem:

$$min\left[\frac{||w||^2}{2}\right], Subject\ to\ (A.1.3) \qquad (a.1.4)$$

For taking into account non-linearly separable data, *slack* variables ξ are introduced to deal with misclassified samples (see Fig. a.1). Eq. (6.3) becomes

$$y_i(w \cdot x_i + b) > 1 - \xi_i\,, \qquad \xi_i \geq 0\ \forall i \in [1, N] \qquad (a.1.5)$$

The final optimization problem can be described as

$$min\left[\frac{||w||^2}{2} + C\sum_{k=0}^{N} \xi_i\right]\ , \quad \text{Subject to} \quad (A.1.5), \qquad (a.1.6)$$

where the constant C is a regularization parameter that controls the amount of penalty. These optimization problems are usually solved by quadratic programming [16]. The classification is further performed by computing $y_u = sgn(w \cdot x_u + b)$, where (w,*b*) are the hyperplane parameters found during the training process and x_u is an unseen sample.

An important notice is that the pixel vectors in the optimization and decision rule equations always appear in pairs related through a scalar product. Therefore, these products can be replaced by nonlinear functions of the pairs of vectors, essentially projecting the pixel vectors into a higher dimensional space Ĥ and thus improving linear separability of data:

$$\check{R}^B \to \hat{H}$$

$$x \to \Phi\ (x)$$

$$x_i + x_i \to \Phi(x_i) \cdot \Phi(x_j) = K\ (x_i, x_j) \qquad (a.1.7)$$

Here, Φ (•) is a nonlinear function for projecting feature vectors into a new space, K (•) is a kernel function that allows one to avoid the computation of the scalar products in the transformed space $[\Phi(x_i) \cdot \Phi(x_j)]$ and thus reduces the computational complexity of the algorithm. The kernel K should fulfill Mercer's condition [17]. SVM require selecting the kernel carefully. For hyperspectral image classification, two kernels are widely used: the polynomial function and the Gaussian Radial Basis Function (RBF).

$$K_{POLY}\ (x_i, x_j) = [\ (x_i, x_j) + 1]^p \qquad (a.1.8)$$

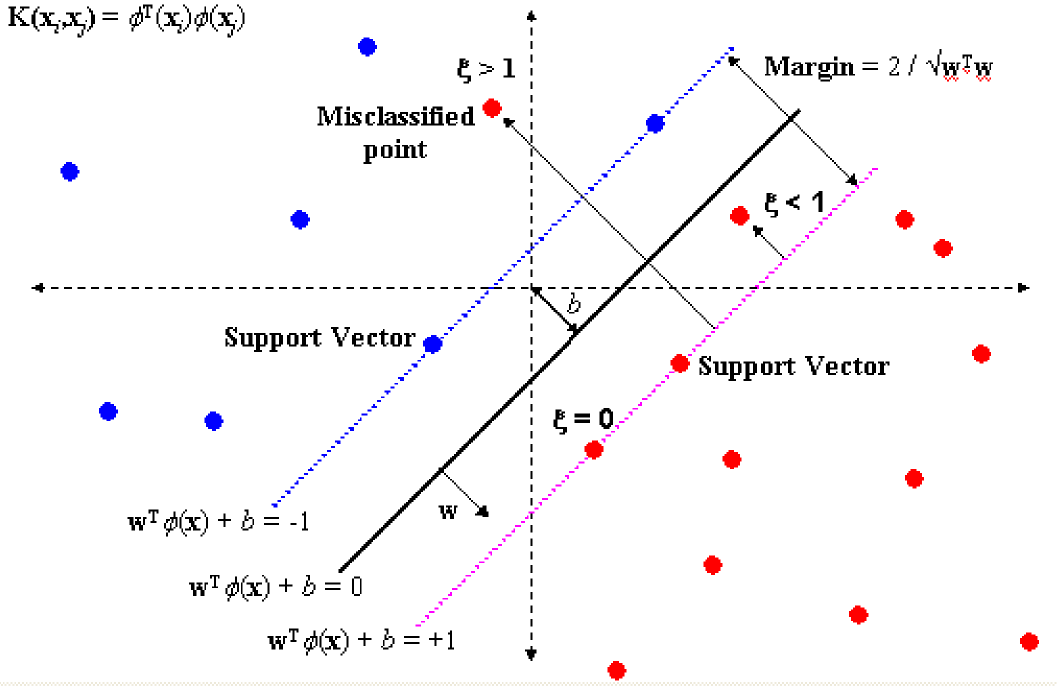

Fig.a.1. Classification of a non-linearly separable case by SVM. There is one non separable feature vector in each class. (*Source- The Stand SVM Formulation, http://research.microsoft.com/en-us/um/people/manik/projects/trade-off/svm.html*)

$$K_{PGAUSS}\left(x_i, x_j\right) = exp\left[-\gamma\left\|x_i - x_j\right\|^2\right] \qquad (a.1.7)$$

where p is the order of the polynomial kernel function, and is the spread of the RBF kernel. SVM are primarily designed to solve binary problems where the class labels can only take two values:±1. To solve the K-class problem, various approaches have been proposed. Two main approaches [18], combining a set of binary classifiers, are defined as

- One Versus All: K binary classifiers are applied on each class against the others. Each pixel x_i is assigned to the class with the maximum output $f(x_i)$.
- One Versus One: $\frac{K(K-1)}{2}$ binary classifiers are applied on each pair of classes. Each pixel is assigned to the class getting the highest number of votes (i.e., winning the maximum number of binary classification procedures).

The one versus one classification has shown to be the most suitable for large problems [19], and its computational complexity is comparable to that of the one versus all approach.

***b*. Indicator functions**

Let Ω be a sample space, let $E \subseteq \Omega$ be an event and denote by $P(E)$ its probability. The indicator function (or indicator random variable) of the event E, denoted by 1_E, is a random variable defined as follows:

$$1_E(\omega) = \begin{cases} 1 \text{ if } \omega \in E \\ 0 \text{ if } \omega \notin E \end{cases} \tag{b.1}$$

In other words, the indicator function of the event E is a random variable that takes value 1 when E happens and value 0 when it does not happen. From the above definition, it can easily be seen that 1_E is a discrete random variable with support

$$R_{1_E} = \{0,1\} \tag{b.2}$$

and probability mass function:

$$P_{1_E}(x) = \begin{cases} P(E) & \text{if } x = 1 \\ P(E^C) = 1 - P(E) & \text{if } x = 1 \\ 0 & \text{otherwise} \end{cases} \qquad \text{(b.3}$$

Indicator functions are often used in probability theory to simplify notation and to prove theorems.

Reference

[1] Vapnik, V., 1979, “Estimation of Dependences Based on Empirical Data”, Nauka, Moscow, Vol.27, pp. 5165–5184. (in Russian) (English translation: Springer Verlag, New York, 1982).

[2] Zhu, G., Blumberg, B.G., 2002, “Classification using ASTER data and SVM algorithms; The case study of Beer Sheva, Israel”, Remote Sensing of Environment, Vol.80 (2), pp.233–240.

[3] Cortes, C., Vapnik, V., 1995, “Support-vector networks”, Machine Learning, Vol.20(3),pp.273–297.

[4] Scholkopf, B., Smola, A.J., 2001, Learning with Kernels, The MIT Press.

[5] Knerr, S., Personnaz, L., Dreyfus, G., 1990, “Single-layer learning revisited: a stepwise procedure for building and training a neural network”, Neuron-computing Algorithms, Architectures and Applications, NATO ASI Series, Springer.

[6] Mantero, P., Moser, G., Serpico, S.B., 2005, “Partially supervised classification of remote sensing images through SVM-based probability density estimation”, IEEE Transactions on Geoscience and Remote Sensing, Vol.43 (3), pp.559–570.

[7] Burges, C.J.C., 1998, “A tutorial on support vector machines for pattern recognition”, Data Mining and Knowledge Discovery, Vol. 2 (2), pp.121–167.

[8] Fauvel, M., Chanussot, J., Benediktsson, J.A., 2009, “Kernel principal component analysis for the classification of hyperspectral remote sensing data over urban areas”, EURASIP Journal on Advances in Signal Processing Article, ID 783194.

[9] Montgomery, D.C., Peck, E.A., 1992, “Introduction to Linear Regression Analysis”, Vol.2, Wiley, New York.

[10] Geman, S., Bienenstock, E., Doursat, R., 1992, Neural networks and the bias/variance dilemma. Neural Computation, Vol. 4 (1),pp. 1–58.

[11] Guyon, I., Vapnik, V, Boser, B., Solla, S.A, 1992, “Capacity control in linear classifiers for pattern recognition”, In: First IAPR International Conference on Pattern Recognition. IEEE Computer Society Press, pp. 385–388.

[12] Kavzoglu, T., Colkesen, I., 2009. A kernel functions analysis for support vector machines for land cover classification. International Journal of Applied Earth Observation and Geoinformation, Vol. 11 (5), pp. 352–359.

[13] C. J. C. Burges, 1998. A tutorial on support vector machines for pattern recognition. Data mining and knowledge discovery, Vol. 2, pp. 121–167.

[14] Tso, B., Mather, P., 2009. Classification Methods for Remotely Sensed Data, 2nd ed.CRC

Press,pp. 376

[15] Chen, H., Ho, P., 2008. Statistical pattern recognition in remote sensing. PatternRecognition , Vol. 41 (9), pp. 2731–2741.

[16] V. Vapnik. Statistical Learning Theory. New York: Wiley, 1998.

[17] C. Cortes, and V. Vapnik, “ Support vector networks” , Machine Learning, vol. 20, no. 3, pp. 273-297, 1995.

[18] Barakat, N., Bradley, A.P., 2010. Rule extraction from support vector machines: a review, Neurocomputing. doi:10.1016/j.

[19] Hsu, C.W., Lin, C.J., 2002. A comparison of methods for multiclass support vector machines. IEEE, Trans. Neural Networks, Vol. 13, pp. 415–425.